

Correlated Quantum Phenomena of Spin-Orbit Coupled Perovskite Oxide Heterostructures:
Cases of SrRuO₃ and SrIrO₃-Based Artificial Superlattices

Seung Gyo Jeong, Jin Young Oh, Lin Hao, Jian Liu*, and Woo Seok Choi**

S. G. Jeong, J. Y. Oh, W. S. Choi

Department of Physics, Sungkyunkwan University, Suwon 16419, Korea

E-mail: choiws@skku.edu

Lin Hao

Anhui Key Laboratory of Condensed Matter Physics at Extreme Conditions, High Magnetic Field Laboratory, HFIPS, Chinese Academy of Sciences, Hefei, Anhui 230031, China

E-mail: haolin@hmfl.ac.cn

Jian Liu

Department of Physics and Astronomy, University of Tennessee, Knoxville, Tennessee 37996, USA

E-mail: jianliu@utk.edu

Keywords: Ruthenates, Iridates, Superlattices, Spin-Orbit Coupling, Epitaxy, Magnetotransport

Unexpected, yet useful functionalities emerge when two or more materials merge coherently. Artificial oxide superlattices realize atomic and crystal structures that are not available in nature, thus providing controllable correlated quantum phenomena. This review focuses on $4d$ and $5d$ oxide superlattices, in which the spin-orbit coupling plays a significant role compared with conventional $3d$ oxide superlattices. Modulations in crystal structures with octahedral distortion, phonon engineering, electronic structures, spin orderings, and dimensionality control are discussed for $4d$ oxide superlattices. Atomic and magnetic structures, $J_{\text{eff}} = 1/2$ pseudospin and charge fluctuations, and the integration of topology and correlation are discussed for $5d$ oxide superlattices. This review provides insights into how correlated quantum phenomena arise from the deliberate design of superlattice structures that give birth to novel functionalities.

1. Introduction

1.1 Oxide Heterostructures

Heterostructures composed of transition metal oxides have been celebrated for decades in fundamental condensed matter research as they serve as one of the key material systems for the development of future functional devices, including thermal, optical, electronic, magnetic, and energy devices.^[1-8] Because of the strong internal electric field generated by the oxygen ions, the chemical bonding nature between the various transition metal elements and oxygen ions are either covalent or ionic.^[9] This strong chemical bonding ensures highly coherent lattice matching epitaxial relationship between the thin films and the substrates or between the different layers within oxide heterostructures.^[4, 10] Such coherent structure is not attainable in structures with, e.g., van der Waals bonding.^[11, 12] This feature also distinguishes oxide heterostructures from semiconductor heterostructures, which shape the contemporary electronics industry, by embedding correlated functionalities for further scalable and energy-efficient multifunctional devices. Hence, the idea of stacking the building blocks of transition metal oxides with various physical and chemical properties to exploit synergetic functionality has been prevalent in the field. Oxide heterostructures can ideally realize combinatorial devices that can simultaneously sense, compute, memorize, and actuate by epitaxially combining the necessary layers. Moreover, the functionalities of each layer can be altered as they are being combined, thereby leading to emergent synergetic functionalities. Thus, the opportunity to develop new materials has been maximized.

Epitaxial oxide heterostructures have led to a revolutionary expansion in the fundamental physical and chemical sciences.^[4] In addition to the conventional strong correlation among charge, spin, lattice, and orbital degrees of freedom in a single transition metal oxide compound, oxide heterostructures of transition metal oxides provide important tuning parameters,^[5] such as epitaxial strain, octahedral distortion, structural symmetry constraints, charge transfer, magnetic and superconducting proximity, orbital engineering, interfacial band bending, ferroelectric field effect, quantum tunneling, dimensional crossover, and inversion symmetry breaking. The systematic and facile control of these parameters has deepened our understanding of the underlying mechanisms of the functionalities.^[13] In particular, the on-demand growth of oxide heterostructures has allowed us to explore the vast landscape of intriguing and important problems in the field.

Oxide superlattices employ coherent lattice structures of the oxide heterostructures to the very limit, which is a single atomic layer.^[4] They promote single-crystalline structures that are not available in nature, thereby overcoming the thermodynamic constraints for spontaneous natural crystal formation. The development of atomic-scale precision control of the layers enabled genuine man-made crystals with facile tunability of the lattice structures and periodicity. Even though the strong correlation often occurring in oxides largely modify the structure, the electronic band structure is essentially the energy eigenfunction of electrons under a periodic potential. Hence, the control of the periodic potential via artificial engineering of lattices fundamentally allows altering the physical and chemical properties of the material. For example, the size of the unit cell of superlattices can be digitally increased with the periodicity superimposing the original periodicity of each constituent layer, giving rise to the band folding in the momentum space with the formation of minibands. By exploiting the aforementioned strong covalent/ionic bonding between the transition metal and oxygen, the crystalline symmetry, chemical stoichiometry, and dimensionality of the artificial crystal can be further modified. The strong covalent/ionic bonding also underscores the importance of the functional interfaces, the effect of which is considerably amplified in superlattices.

The numerous oxide superlattices can be classified in several ways. For example, tri-color superlattices, in which the inversion symmetry is broken, can be distinguished from conventional bi-color superlattices.^[10] Additionally, the global structures of the superlattices, for example, perovskite, spinel, pyrochlore, and brownmillerite, can be a basis for classification. However, the vast majority of oxide superlattices studied to date have perovskite structures. One can also categorize the oxide superlattices by focusing on the transition metal elements. Whereas $3d$ transition metal oxides have been intensively studied over the last several decades, recently, $4d$ and $5d$ transition metal oxides have become increasingly important with the introduction of appreciable spin-orbit coupling (λ), of which the strength is comparable to the on-site Coulomb interaction (U) and crystal field splitting energy (Δ) within the transition metal oxygen octahedra (Table 1). As a result of the variety of spin-orbit-entangled degrees of freedom and their non-trivial interactions, various exotic correlated phases can realize in $4d$ and $5d$ elements, including spin-orbit-assisted Mott insulators, $J_{\text{eff}} = 1/2$ magnetism, quantum spin liquids, excitonic magnetism, multipolar orderings, and correlated topological semimetals.^[14] The combination of these novel spin-orbit-entangled states with conventional oxide superlattice approaches provides a new frontier

of correlated quantum phenomena with practical controllability that inspires future quantum electronic devices with various functionalities. Therefore, oxide superlattices containing $4d$ and $5d$ transition metal oxide layers possess physics beyond in those superlattices with $3d$ transition metal elements, as schematically shown by the correlated functionalities in **Figure 1**. Herein, first, we briefly summarize previous studies on $3d$ oxide superlattices, the idea and methods of which can be applied and extended to $4d$ and $5d$ oxide superlattices. Subsequently, we discuss the $4d$ and $5d$ oxide superlattices in further depth.

1.2 $3d$ Based Superlattice

Most traditional $3d$ perovskite oxides have been used as constituent layers in superlattices. Titanates (SrTiO_3 , BaTiO_3 , CaTiO_3 , and LaTiO_3) have been extensively studied, partly owing to the intriguing physical behavior of SrTiO_3 , including its quantum paraelectric nature and ability to accommodate oxygen vacancies. Before the discovery of unexpected metallic behavior at the interface between two band insulators, i.e., LaAlO_3 and SrTiO_3 ,^[15] the interface between a Mott insulator and a band insulator, i.e., LaTiO_3 and SrTiO_3 , respectively, was found to be metallic owing to the “electronic reconstruction”.^[16] $\text{LaTiO}_3/\text{SrTiO}_3$ superlattices provided an ideal testbed for experimental examination of the unexpected metallic interface as they effectively amplify the conducting signature observed not only from the transport measurements but also by optical spectroscopy. As shown in **Figure 2a**, the structure can be viewed as a La substitution for Sr within the SrTiO_3 matrix in a layer-by-layer manner, i.e., delta-doping. Optical spectroscopy characterizes the intrinsic carrier density of the entire superlattice, as shown in **Figure 2b**.^[17] Here, the sheet carrier density is independent of the overall La concentration, thus indicating that only the interface is metallic and not the entire sample. Note that such observation would have been extremely difficult with a single interface in conventional oxide heterostructures. The $\text{LaTiO}_3/\text{SrTiO}_3$ interface has the potential for use in transparent conducting electrode applications as the visible light can penetrate the sample without much absorption.^[18] The La delta-doping approach was later developed as fractional doping of the superlattice, thus enabling control of the carrier density at the interfaces.^[19] This approach was found to be beneficial for thermoelectric applications.^[20] Another important functionality of $\text{LaTiO}_3/\text{SrTiO}_3$ superlattices is quantum resonant tunneling (**Figure 2c**).^[21] This report is the first observation of resonant tunneling in oxide superlattices, which has been an important subject in semiconductor superlattices. On the other hand, the dimensional quantum confinement of $3d^1$ electrons was optically characterized in the $\text{LaTiO}_3/\text{LaAlO}_3$ superlattices.^[22]

As in the case of La doping, SrTiO₃ is a very effective system that exhibits a wide variety of electronic phases (from insulator to superconductor) upon doping. Nb doping has proven to be efficient, and by constructing superlattices of metallic Nb-doped SrTiO₃ and SrTiO₃ layers, the dimensionality of the metallic layer can be reduced to the thickness of a single unit-cell. One of the merits of the reduced dimension is the enhancement of the electron-phonon coupling, which increases the thermopower of the low-dimensional system, as shown in **Figure 2d**.^[23, 24]

Titanate superlattices have been extensively studied in terms of their ferroelectric properties. BaTiO₃ is ferroelectric, SrTiO₃ is incipient ferroelectric, and CaTiO₃ is paraelectric. However, by combining these materials at the atomic scale, the ferroelectricity can be further enhanced, as shown in **Figure 2e**. The paraelectric layers become ferroelectric owing to cooperative structural distortion within the superlattices.^[25] On the other hand, the three titanate perovskites can be combined to form tri-color superlattices with inherent inversion symmetry breaking. Inversion symmetry breaking is essential for the emergence of ferroelectricity, and ferroelectricity may be expected even with nonferroelectric constituents. The tri-color superlattices exhibit enhanced ferroelectric polarization, thus corroborating the intuitive symmetry-breaking mechanism (**Figure 2f**).^[10] Such a polar order could be further modified by geometric constraints offered by the oxide heterostructure. The epitaxial tensile strain in PbTiO₃/SrTiO₃ multilayers induced flux-closures,^[26] which was later extended to smaller polar vortex structures in PbTiO₃/SrTiO₃ superlattices, as shown in **Figure 2g**.^[27] Furthermore, the modulation of the lattice structure and interfaces leads to an entirely different global vibrational response of the superlattices (**Figure 2h**), thereby leading to a greater control over the thermal conductivity.^[28, 29]

Except for titanates, 3d perovskite superlattices have been realized using vanadates,^[30] manganites,^[31] ferrites,^[32] cobaltites,^[33] and nickelates.^[34] In nickelates, the dimensionality change results in a collective change in the correlated electronic and magnetic phase transitions (**Figure 2i**). For oxide superlattices other than perovskites, hexagonal LuFeO₃ superlattices have representatively demonstrated magnetoelectric coupling promoted by geometric ferroelectricity (**Figure 2j**).^[35]

This review summarizes recent studies on $4d$ and $5d$ oxide superlattices. Most of the $4d$ and $5d$ superlattices studied thus far contain SrRuO_3 and SrIrO_3 layers, respectively. Hence, herein, we focus on the superlattices of these two important materials. Chapter 2 introduces state-of-the-art atomic-scale epitaxy techniques that enable the realization of artificial superlattices. Chapter 3 discusses the SrRuO_3 based superlattices. Starting from the lattice structure modulation, we discuss artificial phonon engineering, ferromagnetism, dimensionality-induced phase transition, and topologically nontrivial spin structures. In Chapter 4, we discuss SrIrO_3 based superlattices. The crystal structure, epitaxial strain, spin-charge fluctuation, and fluctuation of $J_{\text{eff}} = 1/2$ pseudospin in the 2D limit are discussed. We will further compare the natural layered crystal of the Ruddlesden-Popper series with the superlattices. Finally, we summarize this review in Chapter 5 with an outlook.

2. Atomic Scale Epitaxy Techniques: Realization of Artificial Oxide Crystal

The development of modern epitaxy techniques has provided atomic-scale precision controllability of state-of-the-art oxide heterostructures. Prominent epitaxy techniques for realizing oxide superlattices include sputter deposition, pulsed laser epitaxy, and molecular beam epitaxy. Sputtering was first employed to fabricate iron oxide films in 1852.^[36, 37] To this day, sputtering is widely used for thin film growth as it is economical and useful for mass production in the industry.^[38] The sputtering process uses the plasma produced by electrical discharge and the electrostatic acceleration of ions to deposit the thin film material on the substrate surfaces. Oxide heterostructures and superlattices can be grown using two target compounds. High-quality oxide superlattices grown by sputter deposition include cuprates,^[39] titanates,^[38, 40] ruthenates,^[41] nickelates,^[42, 43] and manganites.^[44]

Owing to the improvement in vacuum techniques in the 1960s, both pulsed laser epitaxy and molecular beam epitaxy have been developed.^[45, 46] Pulsed laser epitaxy is one of the most appreciated approaches that demonstrates the atomic-scale epitaxy of oxide superlattices. The thin film growth process is as follows.^[47] 1) A pulsed laser ablates the surface of a target in a vacuum chamber and generates a plasma plume. 2) The plasma plume propagates and reaches the heated substrate. 3) The ion clusters crystallize on the substrate surface through a thermodynamic process. Pulsed laser epitaxy is useful for synthesizing complex heterostructures and superlattices using a target manipulator. The growth window of pulsed laser epitaxy is typically wide for transition metal oxides and can be modulated using several experimental parameters, such as the laser (pulse energy and repetition rate), substrate

(material, surface, and temperature), and type of background gas, pressure, and flow rate in the growth chamber.^[48] In particular, the interaction (or scattering) between plasma and background determines the kinetics, oxidation state, and stoichiometry of the incoming plume, as well as the final surface dynamics of incoming species. These factors settle the growth mechanisms of oxide thin films, such as layer-by-layer, step flow, and island growth modes.^[47, 49-51] For example, in cases of SrRuO₃ based superlattices, the growth of the thin film layer of SrRuO₃ depends sensitively on the substrate temperature, oxygen background pressure, and laser fluence. First, due to the volatile nature of Ru ions at high temperatures, substrate temperatures of around 700 °C are commonly used. Second, a sufficiently oxygen-rich environment of 100 mTorr is required to synthesize stoichiometric SrRuO₃ layers.^[49, 52] Third, since high laser fluence can induce unintended cation vacancies and change the growth modes,^[53, 54] a laser fluence of around 1.2 J/cm² is typically used for the growth of SrRuO₃ layers. Finally, when constructing a superlattice, we should consider the deposition conditions of the partner layer, ensuring that they do not compromise the functionality of SrRuO₃. Moreover, it is crucial to experimentally verify whether the selected deposition conditions are appropriate. Although measuring small changes in the chemical composition ratio of SrRuO₃ according to these experimental conditions is difficult, the prominent observations are the variation in the ferromagnetic phase transition temperature and electrical transport behaviors.^[49, 53] On the other hand, by adjusting the number of laser pulses, the growth of each layer within a superlattice can be accurately controlled with atomic-scale precision, even without reflection high energy electron diffraction.^[55] Thanks to the versatile technical advantages, the majority of oxide superlattices with atomic-scale precision thickness control have been reported as using pulsed laser epitaxy.

Molecular beam epitaxy supplies each constituent element of perovskite oxide independently, under ultrahigh vacuum conditions, whereas both sputtering and pulsed laser epitaxy typically use stoichiometric ceramic targets. Molecular beam epitaxy offers selective cation control of perovskite oxides with atomic-scale precision thickness control via the instantaneous shutter control of individual elements.^[56] High-vacuum conditions also provide a high mean free path for electrons and ions suitable for in-situ characterizations, including high-energy electron diffraction, low-energy electron diffraction, X-ray photoelectron spectroscopy, and Auger electron spectroscopy. One of the experimental parameters of oxide molecular beam epitaxy for stoichiometric films is the oxidant and/or the oxidant background pressure. Because molecular oxygen in early oxide molecular beam epitaxy is insufficient in numerous cases,

oxygen plasma and/or ozone gases have become popular for achieving more aggressive oxidizing environments; however, they are accompanied by high vapor pressure and require external vapor inlet systems. More recently, solid source metal-organic molecular beam epitaxy has been suggested to obtain low vapor pressures and low source temperatures, which is more stable and cheaper compared with other oxide molecular beam epitaxies.^[57] Finally, atomic layer deposition has also proven to be useful in depositing oxide thin films, although the realization of perovskite oxide superlattices has yet to be demonstrated.

3. 4d SrRuO₃ Based Superlattices

The 4d perovskite oxide SrRuO₃ exhibits itinerant ferromagnetism with various correlated functionalities.^[58-60] In bulk, SrRuO₃ exhibits an orthorhombic structure at room temperature with the *Pbnm* space group having $a^-a^-c^+$ rotation pattern in the Glazer notation. The bulk lattice constants are $a = 5.5670 \text{ \AA}$, $b = 5.5304 \text{ \AA}$, and $c = 7.8446 \text{ \AA}$ in orthorhombic notation,^[61] whereas the pseudo-cubic lattice constant is 3.93 \AA .^[49] Owing to their chemical stability, electrical conductivity, and versatile physical properties, SrRuO₃ films have received considerable attention for both fundamental correlated physics and applications.^[58] In particular, the spin-orbit coupling strength of the 4d Ru ions is comparable to the electronic correlation energy scales, for example, Hund's coupling, crystal field splitting, and electron hopping,^[14] thus leading to novel spin-orbit-coupled electronic ground states and physical phenomenon. The three Ru t_{2g} orbitals (d_{xy} , d_{xz} , and d_{yz}) within SrRuO₃ are filled with four electrons following Hund's rule, thereby stabilizing $S = 1$ spin states in the bulk.^[62] Theoretical calculations suggested a half-metallic behavior with Stoner spin splitting of SrRuO₃.^[63] When the stoichiometry deviates from the ideal SrRuO₃, for example, when Ru-O vacancies are introduced, a structural phase transition from orthorhombic to tetragonal is observed, along with changes in the electronic and chemical behaviors.^[49, 64]

By taking advantage of the epitaxial heterostructuring, facile control over the d -electron configuration, octahedral bonding geometry, crystalline symmetry, magnetic interactions, and electronic dimensionality can be achieved. Since the first growth of single-crystalline SrRuO₃ epitaxial films in 1992 reported by Eom et al.,^[65] numerous SrRuO₃ heterostructures have been demonstrated to exhibit intriguing functional phenomena, such as metal-insulator transition,^[66, 67] structural phase transition,^[68, 69] electrocatalytic activity,^[64] spin-phonon coupling,^[70] itinerant ferromagnetism,^[71, 72] controllable magnetic anisotropy,^[52, 73] anomalous and/or topological Hall effect,^[74-79] Weyl fermion behavior,^[80] topological magnon,^[81, 82] and

chiral phonon-mediated magnetic interactions.^[55] Several studies have demonstrated epitaxially grown SrRuO₃ thin films on SiO₂/Si substrates,^[83-85] which implies the potential integration of correlated functional oxides with Si-based electronics. Atomically designed SrRuO₃ superlattices provide further extended controllability of the correlated functionalities, depending on the type of partner oxide layer and substrate, chemical stoichiometry, individual layer thickness, repetition number, and stacking order of the supercell structure. Table 2 summarizes the reported SrRuO₃ based superlattices with various functional partner compounds.^[41, 54, 55, 70, 86-164] Herein, several emergent functionalities of SrRuO₃-based superlattices and their modulations are reviewed in the following Sections.

3.1 Modulation of Correlated Lattice Degree of Freedom

The customized lattice degree of freedom of orthorhombic SrRuO₃ provides a facile control knob for determining multiple correlated functionalities.^[58] A theoretical study proposed that the orthorhombic structure of SrRuO₃ with octahedral tilt and the tetragonal structure of SrRuO₃ without octahedral tilt have almost the same energy, differing by only a few tens of meV.^[165] By taking advantage of the nearly degenerate energy of the orthorhombic and tetragonal structures of SrRuO₃, it is possible to control the octahedral tilts of both structures and stabilize various structural phases through epitaxial heterostructures. Such structural modification modulate the ferromagnetic behavior (transition temperature, coercive field, magnetic easy axis, and magnetization value), electronic structure (crystal field and orbital hybridization), magnetotransports, and topological behavior. This section introduces various structural modulations in SrRuO₃ based superlattices from microscopic octahedral distortion to macroscopic crystalline symmetry.

3.1.1 Octahedral Distortion

Contemporary scanning transmission electron microscopy can directly visualize minute distortions of RuO₆ octahedra in SrRuO₃-based heterostructures. Wang et al. reported the SrRuO₃ thickness-dependent evolution of lattice mismatch within SrRuO₃/LaCoO₃ multilayers grown on SrTiO₃ substrates using selected-area electron diffraction patterns (**Figure 3a**).^[156] The authors detected Ruddlesden-Popper-type faults induced by excessive Sr ions within the SrRuO₃ layers. The microstructure could be further modified by controlling the SrRuO₃ layer thickness. Jeong et al. demonstrated the propagation of octahedral distortions in SrRuO₃/SrTiO₃ superlattices. Even for the same thickness of the SrRuO₃ layer, the octahedral distortion was systematically modulated by controlling the atomic-scale

thickness of adjacent SrTiO₃ layers (**Figure 3b**).^[91] As the reportedly, as the STO thickness increased, the cubic nature of the SrTiO₃ layer better restrained the octahedral distortion of the SrRuO₃ layer within the superlattices. A similar approach was adopted by Shan et al., in which the octahedral distortion in SrRuO₃/SrCuO₂ superlattices was modulated by dimensionality control of the infinite layered SrCuO₂ (**Figure 3c**).^[117] With decreasing SrCuO₂ layer thickness, the CuO₂ infinite layer was shown to change from planar to chain-type, which modulated the polyhedral connectivity at the interface. On the other hand, Ziese et al. showed that the out-of-plane lattice constant for the SrRuO₃ layer in SrRuO₃/Pr_{0.7}Ca_{0.3}MnO₃ superlattices could be controlled by the thickness of the Pr_{0.7}Ca_{0.3}MnO₃ layer (**Figure 3d**).^[141] Yao et al. suggested that the ferroelectric polarization of BiFeO₃ induced ionic displacements of the interfacial SrRuO₃ layer in the SrRuO₃/BiFeO₃ multilayers (**Figure 3e**).^[158] This modified the metallic SrRuO₃ layer. Mao et al. further demonstrated electrical field control of the Ru ion displacement via switchable ferroelectric polarization in a SrRuO₃/BaTiO₃ superlattice using in situ transmission electron microscopy, as shown in **Figure 3f**.^[112] By applying an electrical field along the out-of-plane direction, they controlled the ion displacement in both the atomically thin metallic SrRuO₃ and ferroelectric BaTiO₃ layers within the superlattice. They suggested that the asymmetry at the interface due to BaO-RuO₂ and SrO-RuO₂ can induce polarization bistability along the upward and downward directions, leading to the electrical field control of the displacement of Ru ions. On the other hand, finite octahedral rotation led to the two perovskite unit cell periodicity (unit cell doubling) and the resultant half-order Bragg diffraction peak, as studied by May et al.^[166] **Figure 3g** shows the octahedral distortion variation in the SrRuO₃/SrTiO₃ superlattice observed by half-order diffraction measurements using synchrotron X-ray facilities.^[107]

3.1.2 Crystalline Symmetry

The RuO₆ octahedral distortion determines the crystalline symmetry of SrRuO₃ based superlattices. Off-axis X-ray diffraction measurements around (204) SrTiO₃ Bragg reflections with four different azimuth angles (ϕ) of 0°, 90°, 180°, and 270° typically revealed the asymmetric crystal structure of orthorhombic SrRuO₃ heterostructures (**Figure 4a**).^[49] In conventional SrRuO₃ single films, the crystalline symmetry of SrRuO₃ is modulated by controlling the thickness,^[68] epitaxial strain,^[69] and chemical composition of the SrRuO₃ layers.^[64] For superlattices, the control of octahedral tilt propagation was shown to result in an orthorhombic to tetragonal structural phase transition in SrRuO₃/SrTiO₃ superlattices by

manipulating the thickness of the SrTiO₃ layer (**Figure 4b**).^[91] A structural phase map as a function of both SrRuO₃ and SrTiO₃ layer thicknesses was constructed, as shown in **Figure 4c**. Despite the same thickness and stoichiometry of the SrRuO₃ layer, the interfacial octahedral connectivity between SrRuO₃ and SrTiO₃ with atomic-scale thickness modulation systematically realized the structural phase transition of the SrRuO₃/SrTiO₃ superlattice. This further modified the electromagnetic properties of the ferromagnetic SrRuO₃ layer, including the magnetic coercive field, saturation magnetization, and ferromagnetic transition temperature. Sahoo et al. confirmed similar structural phase transitions in SrRuO₃/PrMnO₃ superlattices by varying the thickness of the PrMnO₃ layer, as shown in **Figure 4d**.^[147] A shift in the magnetic hysteresis loop was observed, and it was enhanced in the case of the tetragonal superlattice, thus indicating crystalline symmetry-dependent interfacial antiferromagnetic coupling. The distorted lattice structure in the SrRuO₃ layer within the superlattice can also influence the crystalline symmetry of the partner layer, with inversion symmetry breaking at the interface. Behera et al. proposed a possible orthorhombic structure in the La_{0.7}Sr_{0.3}MnO₃ layers within SrRuO₃/La_{0.7}Sr_{0.3}MnO₃ superlattices on a (110)-oriented SrTiO₃ substrate using X-ray diffraction and Raman spectroscopy (**Figure 4e**).^[129] Four unit cell layers of La_{0.7}Sr_{0.3}MnO₃, sandwiched between 14 unit cell layers of SrRuO₃, exhibited an orthorhombic structure, leading to modification of the magnetic behavior. Using density functional theory calculations and ferroelectric measurements, Callori et al. discussed the possibility of three different types of interfaces depending on the chemical composition and inversion symmetry breaking in the SrRuO₃/PbTiO₃ superlattice (**Figure 4f**).^[41] As the thickness of the PbTiO₃ layer within the superlattices decreased, the polarization asymmetry was enhanced owing to the compositional inversion symmetry breaking, which led to modified ferroelectric phases. Hence, the superlattice approach provides facile and versatile controllability of the bonding geometry in correlated quantum oxides, thus providing numerous intriguing functionalities.

3.2 Correlated Phonon Engineering

Facile structural modification in artificial quantum oxides enables the manipulation of phonon dispersion, phonon group velocity, electric polarization, and the density of states of phonons.^[167] This has potential for future acoustic applications, including quantum Bragg mirrors and cavities,^[168] quantum acoustic memory and transducers,^[169] microwave-optical converters,^[170] quantum amplifiers,^[171] and circuit acoustodynamics.^[172] Most studies on phonon engineering have been limited to high-quality III–V compound semiconductors.

However, recent phonon engineering in correlated oxides can lead to novel applications of tunable coherent phonon excitations for future quantum acoustic devices integrated with their correlated functionalities.

3.2.1 Zone-Folded Phonon and Its Dynamics

The superimposed periodicity of the superlattice induces the backfolding of the acoustic phonon dispersion, thereby generating zone-folded acoustic phonons in the GHz and/or THz frequency range. Jeong et al. demonstrated phonon dispersion in SrRuO₃/SrTiO₃ superlattices, as shown in **Figure 5a**.^[88] As the supercell periodicity is designed to be ten times of the bulk SrTiO₃ lattice constant, the reciprocal lattice constant of the superlattice decreases by ten times with the appearance of an equivalent backfolded Brillouin zone. This leads to zone-centered acoustic phonons near the Γ -point. The left panel of **Figure 5b** shows the theoretically estimated phonon dispersion with the presence of zone-folded acoustic phonons in SrRuO₃/SrTiO₃ superlattices. Clear Raman excitations of zone-folded acoustic phonons with systematic control of their excitation frequency in the THz frequency range were demonstrated via precise thickness control of the supercell periodicity (middle and right panels of Figure 5b). Such coherent phonon modes of superlattices were also observed in the time-resolved pump-probe measurement, as shown the top panel of **Figure 5c**, studied by Yang et al.^[103] By examining the fast Fourier transformed pump-probe spectra of the SrRuO₃/(SrTiO₃ or SrIrO₃) superlattices, the excitation frequency and mean free path of the zone-folded acoustic phonons were obtained. The bottom panel of Figure 5c shows the experimentally observed phonon mean free path following the theoretical model, thus validating the experimental approaches. Bojahr et al. compared the oscillation phase of zone-folded acoustic phonons in optical pump-probe measurements to ultrafast X-ray diffraction in SrRuO₃/SrTiO₃ superlattices (**Figure 5d**).^[108] Both optical measurements showed the same fluence dependence of the phase but complex wavelength dependence of the broadband data. Schmising et al. reported the ultrafast structural evolution of the lattice and polarization dynamics in a SrRuO₃/PbZr_{0.2}Ti_{0.8}O₃ superlattice using femtosecond X-ray diffraction.^[113] **Figure 5e** shows the relative angular shift of the selected Bragg reflection, representing a transient expansion of the superlattice structure by 0.24%. The optical excitation of the SrRuO₃ metal layers generates a large stress that compresses the PbZr_{0.2}Ti_{0.8}O₃ layers within the superlattice, thereby offering optically controllable ferroelectric polarizations. On the other hand, the photoinduced ultrafast stress generation in ferromagnetic SrRuO₃ confirmed the subpicosecond magnetostriction effect in the nanolayered SrRuO₃/SrTiO₃ superlattice via

ultrafast X-ray diffraction.^[95] It was shown that the phonon-mediated and magnetostrictive stress contributions had similar strengths but opposite signs in the SrRuO₃/SrTiO₃ superlattice. The amplitudes of the ultrafast X-ray signals (solid diamonds) followed the temperature-dependent magnetization squared below the ferromagnetic transition temperature. This represents a close interplay between the lattice and spin degrees of freedom in SrRuO₃ heterostructures.

3.2.2 Spin-Phonon Coupling

Strong spin-phonon coupling plays an important role in understanding the correlated long-range spin order in SrRuO₃ systems. For example, in 1994, Kirillov et al. reported temperature-dependent Raman spectra of a SrRuO₃ single film to exhibit phonon anomalies at the ferromagnetic transition temperature (**Figure 6a**).^[173] The report However, they could not investigate the polarization selection rules for the phonon analysis owing to the multidomain structure of SrRuO₃ single films. Iliev et al. further developed the polarized Raman spectra of SrRuO₃ films with a thickness of approximately 300 nm grown on (010)- and (001)-oriented SrTiO₃ substrates (**Figure 6b**).^[174] The authors tentatively assigned the experimentally observed Raman excitations using lattice dynamical calculations. **Figure 6c** summarizes the temperature dependence of the peak position and linewidth of the four different Raman branches of the (010)-oriented SrRuO₃ film. The temperature dependence of the phonon peak position exhibited an anomaly around the ferromagnetic transition temperature. The temperature anomaly of the 391 cm⁻¹ phonon mode (regarding apical oxygen vibrations) could be understood as spin-exchange coupling modulated by ionic displacement. However, other phonon anomalies (especially for the 225 cm⁻¹ phonon mode is mainly related to Sr ion vibration) could not be explained by the conventional magnetostriction effect. This suggests that the mechanism of spin-phonon coupling in SrRuO₃ is complicated. Although the phonon linewidths have a relatively large experimental error, the authors suggested that the linewidth peaked near the transition temperature, which also supports the coupling between the optical phonons and fluctuations of the magnetic order parameter near the phase transition.

A more recent study on SrRuO₃/SrTiO₃ superlattices has demonstrated that a similarly strong spin-phonon coupling can be preserved in the atomically thin SrRuO₃ layers within the superlattice, as shown in **Figure 6d**.^[70] A slight difference in the ferromagnetic transition temperature between the single film and superlattice was detected in the phonon spectra, thus providing experimental proof of the preserved spin-phonon coupling. Furthermore, the

temperature-dependent Raman spectra of the SrRuO₃/SrTiO₃ superlattice shows that the phonon mode at $\sim 367\text{ cm}^{-1}$ split into two modes, at ~ 358 and $\sim 386\text{ cm}^{-1}$ below the ferromagnetic phase transition temperature (**Figure 6e**). The split in phonon mode could be assigned to oxygen vibrations with orthogonal polarizations in orthorhombic bulk SrRuO₃ by utilizing lattice dynamical calculations. It was proposed that the superposition of two orthogonal linear phonon modes with phase differences could give rise to circular phonons, which could combine with spins or magnetic moments.^[55] The molecular field in the ferromagnetic phase of the SrRuO₃ layer induced the phonon Zeeman effect and the resultant temperature-dependent phonon splitting below the ferromagnetic transition temperature in the Raman spectra, thus evidencing chiral symmetry breaking. This revealed a chiral phonon-mediated interlayer exchange interaction and synthetic spin structure in the superlattice. The synthetic spin structure will be further discussed in Section 3.5.2.

3.3 Tunable Ferromagnetism

Superlattice design provides unprecedented tunability of spin ordering in SrRuO₃ layers. This Section discusses various magnetic and magnetotransport behaviors in SrRuO₃ based superlattices. We also introduce unconventional magnetic interactions across the heterointerface and/or between SrRuO₃ layers within the superlattices. This summary can inspire the design of correlated magnetic superlattices for future spintronic applications. These applications may include magnetoresistive memories, magnetic racetracks, spin-orbit torque memories, and current-induced magnetization switching devices.^[60, 175, 176]

3.3.1 Structural Modulation of Ferromagnetic Order

Owing to the finite spin-orbit interaction, the global and local structural modifications of the SrRuO₃ layer lead to tunable anisotropic ferromagnetic properties, including saturation magnetization, coercive field, and magnetotransport behaviors. For example, Jeong et al. examined the crystalline symmetry-dependent spin state of a SrRuO₃/SrTiO₃ superlattice via atomic-scale thickness control of the SrTiO₃ layers.^[91] As the orthorhombic distortion of the SrRuO₃ layer evolves toward tetragonal symmetry, the crystal field splitting between the d_{xy} and $d_{xz,yz}$ orbitals is enhanced, resulting in a reduction in saturation magnetization. This is schematically shown in the left panel of **Figure 7a**. X-ray absorption spectroscopy with linear dichroism demonstrated the enhancement of the unoccupied state at d_{xy} orbitals of the tetragonal SrRuO₃/SrTiO₃ superlattice (right panel of **Figure 7a**), experimentally supporting this argument. **Figure 7b** shows the structural dependence of magnetization as a function of

the magnetic field for the orthorhombic and tetragonal SrRuO₃/SrTiO₃ superlattices. The magnetic coercive field significantly increased for the tetragonal superlattices compared with the orthorhombic ones. Lin et al. consistently demonstrated that SrCuO₂/SrRuO₃/SrCuO₂ heterostructures exhibits structure-dependent magnetic hysteresis behavior via dimensionality control of infinite-layer-SrCuO₂ (**Figure 7c**).^[117]

Magnetotransport measurements also reveal the structural modulation of the ferromagnetic behavior. Evidently, the magnetotransport signal originates predominantly from the metallic SrRuO₃ layer when the partner layer of the superlattice is insulating. **Figure 7d** shows the magnetic field-dependent magnetoresistance (left panel) and anomalous Hall effect (right panel) of the SrRuO₃/SrTiO₃ superlattices, confirming the structural evolution of the magnetic coercive field depending on the SrTiO₃ layer thickness.^[89] Furthermore, an anomalous Hall signal contains contributions from topological spin dynamics. Chen et al. theoretically suggested the existence of Weyl nodes in ferromagnetic SrRuO₃, inspired by the observation of nonmonotonic temperature dependence of anomalous Hall signal and magnetization. These observations suggest a finite Berry curvature in the SrRuO₃.^[177] Itoh et al. measured the temperature-dependent spin-wave gap using neutron diffraction, exhibiting identical nonmonotonic temperature dependence. This further supports the presence of Weyl Fermions along with spin-wave excitation.^[81] Based on these studies, Jeong et al. showed that the size of the spin-wave gap could be further enhanced by using a tetragonal SrRuO₃ layer, induced by the modulated magnetic anisotropy in superlattices (**Figure 7e**).^[89] **Figure 7f** shows the temperature-dependent anomalous Hall resistivity of the SrRuO₃/Pr_{0.7}Ca_{0.3}MnO₃ superlattice.^[141] Whereas the anomalous Hall signals of orthorhombic SrRuO₃ single films (green and yellow lines) and SrRuO₃/SrTiO₃ superlattices (red and blue lines) were negative at low temperatures, the tetragonal SrRuO₃/Pr_{0.7}Ca_{0.3}MnO₃ superlattice (navy line) exhibited a positive sign. Ziese et al. performed angle-dependent magnetoresistance measurements, as shown in **Figure 7g**.^[138] The experimental results for orthorhombic (left panel of Figure 7g) and tetragonal (right panel of Figure 7g) superlattices show good agreement with the fitting results, thus representing the structural dependence of the magnetotransport behavior. Cui et al. reported that the angle-dependent magnetoresistance of SrRuO₃/SrTiO₃ superlattices changes from twofold to fourfold perpendicular symmetry with increasing SrTiO₃ layer thickness owing to structural modifications (**Figure 7h**).^[107]

3.3.2 Interfacial and Interlayer Exchange Coupling

Interfacial exchange coupling of the SrRuO₃ layer with different magnetic compounds and/or interlayer exchange coupling between the SrRuO₃ layers within superlattices leads to an intriguing correlated magnetic order with functionalities. Qu et al. showed the reorientation of lateral magnetic anisotropy in SrRuO₃/La_{0.67}Ca_{0.33}MnO₃ superlattices, as shown in **Figure 8a**.^[145] The magnetic field-dependent magnetization curves of the superlattices exhibited a rotation of the magnetic easy axis from the orthorhombic [010] to [100] axis with increasing repetition number of the superlattices. By performing X-ray absorption spectroscopy and structural characterizations, the combination of epitaxial strain and interfacial coupling was suggested to be the origin of magnetic easy axis modulation. On the other hand, the exchange interaction across the interface of ferromagnetic SrRuO₃ and antiferromagnetic layers frequently revealed an exchange bias effect, characterized by the shift of the magnetic hysteresis loop. Padhan and Prellier reported a large difference between the field-cooled and zero-field-cooled magnetic hysteresis loops and anisotropic behavior depending on the magnetic field direction for SrRuO₃/SrMnO₃ superlattices with different SrMnO₃ layer thicknesses (**Figure 8b**).^[151] Here, anisotropic interfacial coupling was demonstrated between the biasing moments of the ferromagnetic SrRuO₃ layer and pinning moments of the antiferromagnetic SrMnO₃ layer within the superlattices. **Figure 8c** shows the temperature-dependent exchange bias in the SrRuO₃/LaNiO₃ superlattices investigated by Liu and Ning.^[157] The appearance temperature of the magnetic bias effect is defined, which is much lower than the magnetic transition temperature of SrRuO₃. Singh and Chen reported a vertical shift of the hysteresis loop in SrRuO₃/BiFeO₃ superlattices, as shown in **Figure 8d**.^[159] This shift was attributed to pinned Ru⁴⁺ moments at the interface and local defects in the SrRuO₃ layer. Ziese et al. reported antiferromagnetic interlayer coupling in SrRuO₃/La_{0.7}Sr_{0.3}MnO₃ superlattices.^[136] The left panel of **Figure 8e** shows the out-of-plane (circles) and in-plane (squares) magnetic moments as functions of temperature. By varying the SrRuO₃ layer thickness, a change in the magnetization below the ferromagnetic transition temperature of SrRuO₃ was evident, thus indicating an interlayer-coupled spin order. The magnetic-field-dependent magnetization curves in the right panel of Figure 8e support the SrRuO₃ thickness-dependent interlayer coupling in the SrRuO₃/La_{0.7}Sr_{0.3}MnO₃ superlattices. Sahoo et al. also studied interlayer exchange coupling in SrRuO₃/PrMnO₃ superlattices.^[147] This superlattice is composed of two ferromagnets in which the two layers exchange couples. As an example, **Figure 8f** shows the modulated magnetic field-dependent magnetization curves of the superlattice as a function of the PrMnO₃ thickness, indicating the interlayer coupling. More

recently, Jeong et al. suggested unconventional interlayer exchange coupling and resultant synthetic spin structures via chiral phonons in SrRuO₃/SrTiO₃ superlattices.^[55]

3.4 Dimensionality-Induced Phase Transition

Dimensional crossover with an electromagnetic phase transition is a key concept for realizing and understanding the low-dimensional correlated functionality of SrRuO₃ heterostructures. In this section, we introduce the atomic-scale modulation of electronic ground states, which are strongly coupled to the magnetic ground state in SrRuO₃ based superlattices. As the dimensionality of SrRuO₃ decreases, the ferromagnetic metallic ground state in the bulk becomes unstable, which is indicative of an intriguing dimensional crossover. Innovation in atomic-scale epitaxy and microscopy techniques has opened a pathway for investigating the monolayer limit of SrRuO₃ heterostructures. In particular, one advantage of periodic superlattice structures is that they provide measurable experimental signals of monolayer SrRuO₃ with tunable functionality compared with SrRuO₃ single films. We also summarize the recent debate on the magnetic and transport behavior of monolayer SrRuO₃ within superlattices.

3.4.1 Atomic Scale Control of Electronic Ground State coupled Magnetic Behavior

Ueda et al. examined the magnetic and electrical transport properties of SrRuO₃/BaTiO₃ superlattices grown on SrTiO₃ (110) substrates with various stacking periodicities.^[111] As the periodicity of the superlattice decreases, the temperature-dependent resistivity exhibits an electrical phase transition from metal to insulator owing to the reduced dimensionality of the SrRuO₃ layer (top panel of **Figure 9a**). The magnetization versus temperature curves in the bottom panel of Figure 9a shows a concomitant decrease of magnetization and ferromagnetic transition temperature with decreasing periodicity. The inset of Figure 9a further signifies the antiferromagnetic-like behavior of the superlattice consisting of two unit cell layers of SrRuO₃ and five unit cell layers of BaTiO₃, similar to layered ruthenates. Liu et al. reported that SrRuO₃/LaAlO₃ superlattices with varying SrRuO₃ layer thicknesses preserved the ferromagnetic behavior down to two unit cell layers of the SrRuO₃ with a ferromagnetic transition temperature of 110 K (**Figure 9b**).^[116] Izumi et al. demonstrated SrRuO₃ thickness-dependent ferromagnetic behavior observed by temperature-dependent magnetization measurement in **Figure 9c**, in SrRuO₃/SrTiO₃ superlattices.^[86, 87] As the SrRuO₃ layer thickness decreased, the magnetic transition temperature systematically decreased to 60 K for the two unit cell layers of SrRuO₃ within the superlattice. The monolayer SrRuO₃ did not

exhibit magnetic transition down to 2 K. Temperature-dependent resistivity curves of the SrRuO₃/SrTiO₃ superlattice consistently exhibited a decrease in temperature with maximum magnetoresistivity related to the ferromagnetic transition temperature, with decreasing SrRuO₃ layer thickness (**Figure 9d**). In particular, a monolayer SrRuO₃ superlattice with five unit cell layers of SrTiO₃ showed insulating temperature dependence in the absence of ferromagnetic transitions. More recently, consistent demonstration of dimensional crossover in both electronic and magnetic phase transitions for atomically thin SrRuO₃ layers within SrRuO₃/SrTiO₃ superlattices was reported.^[92] A clear distinction between the metallic and insulating phases was also observed from temperature-dependent thermopower measurements. Suppression of the electronic charge carriers in the monolayer SrRuO₃ superlattice induced a large enhancement in the thermopower at low temperatures. Furthermore, a phase instability at the border of the dimensional crossover, i.e., at the two unit cell layers of SrRuO₃, with a temperature-dependent metal-insulator transition along with a metamagnetic transition, was observed. Notably, distinct partner oxide layers of two unit cell SrRuO₃ superlattices exhibit exotic magnetic behavior with transition temperature, thus indicating the tunable magnetic functionality of the low-dimensional SrRuO₃ superlattices. **Figures 9f-9i** further show the dimensionality-induced electronic phase transition of the SrRuO₃/SrTiO₃ superlattices with strongly coupled magnetic phase transitions.^[54, 98, 100] Numerous experiments by different research groups consistently demonstrated the presence of electromagnetic phase transition across the dimensional crossover in the SrRuO₃ layers.

3.4.2 Debate on Monolayer SrRuO₃ within Superlattices

The monolayer limit of SrRuO₃ has tremendous potential for achieving a novel low-dimensional ground state in the electronic, magnetic, and topological states. Alves et al. theoretically proposed a spin-polarized two-dimensional electron gas in a SrRuO₃/SrTiO₃ superlattice composed of a monolayer of SrRuO₃ and five unit cell layers of SrTiO₃, as schematically illustrated in **Figure 10a**.^[102] The authors used local spin density approximation methods with an effective on-site Coulomb interaction of 4.0 eV for the Ru-*d* orbitals. **Figure 10b** shows the typical double peak feature of the Ru-*d_{xz,yz}* states (marked by arrows) that are similar to those frequently observed in 1D metallic systems, representing the low-dimensional electronic structure of the monolayer SrRuO₃ superlattice. Jeong et al. demonstrated the systematic evolution of the dimensionality-induced metal-insulator transition coupled with the magnetic phase transition using the generalized gradient approximation method (**Figure 10c**).^[92] Whereas the trilayer SrRuO₃ superlattice preserved the ferromagnetic metallic state

similar to that of the bulk, the ground states of the monolayer and bilayer SrRuO₃ superlattices were antiferromagnetic insulating states with a finite band gap between the d_{xy} and $d_{yz, zx}$ orbitals of the Ru- t_{2g} states. Thus, they suggested that anisotropic hybridization of the Ru- t_{2g} orbitals induced dimensionality-induced concomitant magnetic and electronic phase transitions in the atomically thin SrRuO₃ superlattices. It was further mentioned that the on-site Coulomb interaction value is important for theoretically reproducing the experimentally observed electromagnetic phase of low-dimensional SrRuO₃ systems.

The experimental realization and characterization of SrRuO₃ monolayers have received considerable attention. Compared with single film, monolayer SrRuO₃ superlattices have a structural advantage in terms of accessible experimental signals required to explore the low-dimensional SrRuO₃ layers. **Figure 10d** shows the clear insulating behavior of the monolayer SrRuO₃ superlattice, characterized by Deng et al.^[54] Note that the resistivity value was much lower compared with that for the SrRuO₃ single film of three atomic unit cell thickness, in which the thinner films could not be measured.^[178] The superlattices were also beneficial for preserving the layer-by-layer growth of the SrRuO₃ layer by controlling laser fluence of pulsed laser epitaxy,^[54] with minimized surface depletion effect. However, we also note that the quantitative resistivity values of monolayer SrRuO₃ superlattices reported by different groups show considerable differences, suggesting the highly sensitive electrical transport behavior of these superlattices within different dielectric environments that mostly provided by the neighboring SrTiO₃ layers. Boschker et al. reported monolayer SrRuO₃/SrTiO₃ superlattices with five unit cell layers of SrTiO₃.^[105] **Figure 10e** shows the temperature-dependent resistivity of three different superlattices with the same periodicity, revealing diverse resistivity values, particularly at the low temperatures. **Figures 10f and 10g** consistently show the clear insulating behavior of the monolayer SrRuO₃ in other SrRuO₃/SrTiO₃ superlattices, where the resistivity significantly increases with the thickness of the SrTiO₃ layer, as observed by two different groups.^[99, 107]

To confirm the effect of the thickness of the SrTiO₃ layer in the monolayer SrRuO₃ superlattices, we summarized the reported temperature-dependent resistivity of the SrRuO₃ monolayer within different SrRuO₃/SrTiO₃ superlattices (**Figures 10h and 10i**).^[86, 92, 99, 105, 107, 109] Figure 10h shows a large variation in the experimental observations from different groups for monolayer SrRuO₃ superlattices depending on the thickness of the SrTiO₃ layer. The resistivity values extracted at 40 and 300 K as a function of SrTiO₃ layer thickness are shown

in Figure 10i. Evidently, most monolayer SrRuO₃ superlattices exhibited increased resistivity as the SrTiO₃ layer thickness increased at both the selected temperatures. This simple analysis indicates a viable interlayer electronic coupling between the SrRuO₃ monolayers through an atomically thin SrTiO₃ layer, thus determining the electronic state of the monolayer SrRuO₃ superlattices. However, so far, several groups have succeeded in depositing SrRuO₃ monolayer superlattices and reported only preliminary experimental results. We hope that future studies will investigate how the interlayer coupling between SrRuO₃ monolayers determines the magnetic ground state associated with the metal-insulator transition. Furthermore, most studies so far have been limited to SrRuO₃/SrTiO₃ superlattices, where charge transfer at the interface is highly suppressed.^[92] The suppression of charge transfer at the SrRuO₃/SrTiO₃ interface has been predicted theoretically by Zhong and Hansmann, in which the energy level of oxygen ion at the interface has been aligned to predict the difference in work function or electron affinity.^[179] SrRuO₃ and SrTiO₃ happen to have similar energy level of oxygen *p*-orbital state with respect to the Fermi energy. This result suggests that a different partner layers other than the SrTiO₃ layer might lead to non-zero charge transfer at the interface, thereby resulting in novel electronic phases in the monolayer SrRuO₃ superlattices. **Figure 10j** shows the temperature-dependent resistivity curves of superlattices with monolayer SrRuO₃ and 10 unit cell layers of BaTiO₃, which is more metallic than the more extensively studied SrRuO₃/SrTiO₃ superlattices.^[112] This experimental observation implies that more intriguing physics might be hidden in the monolayer SrRuO₃ superlattices.

3.5 Synthetic Spin Structures

Owing to the strongly correlated electrons and a considerable spin-orbit interaction, SrRuO₃ based superlattices have introduced various novel synthetic spin structures. In this Section, we discuss synthetic spin structures via spin-phonon coupling and topologically nontrivial spin textures observed and manipulated in SrRuO₃ based superlattices.

3.5.1 Spin-Phonon Coupling Induced Synthetic Spin Structures

As mentioned in Section 3.3.2, ferromagnetic SrRuO₃ is known to have strong spin-phonon coupling, which has been experimentally validated for both single films and superlattices. Based on the strong spin-phonon coupling, the existence of chiral phonons in the SrRuO₃/SrTiO₃ superlattice was proposed based on the observation of the phonon Zeeman effect.^[55] Chiral symmetry breaking of phonons induces emergent quantum magnetic

phenomena such as the phonon Hall effect,^[180] optically driven effective magnetic field,^[181] AC Stark effect,^[182] topologically induced viscosity split,^[183] and pseudogap phases.^[184] Jeong et al. introduced a chiral phonon-induced interlayer exchange interaction between ferromagnetic SrRuO₃ and the resultant synthetic spin structures in SrRuO₃/SrTiO₃ superlattices (**Figure 11a**). The left panel of Figure 11a shows the unexpected oscillatory behavior of in-plane magnetization as a function of the SrTiO₃ layer thickness in the SrRuO₃/SrTiO₃ superlattices. The noncollinear spiral spin state observed from the polarized neutron reflectivity was suggested to be responsible for the observed magnetic oscillation (middle and right panels of Figure 11a), thus suggesting the presence of interlayer exchange coupling. As SrTiO₃ is insulating, the conventional Ruderman-Kittel-Kasuya-Yosida interaction cannot explain the observed behavior. Instead, chiral phonons have been proposed as mediating quasi-particles for unconventional interlayer-exchange interactions.

3.5.2 Topologically Nontrivial Synthetic Spin Structures

The strong antiferromagnetic interlayer coupling and/or Dzyaloshinskii-Moriya interactions at the symmetry-broken interfaces of the superlattice can lead to a topologically nontrivial synthetic spin texture, i.e., magnetic skyrmions, in SrRuO₃, envisioning novel spintronic functionalities. Noncollinear spin structures in SrRuO₃ based superlattices are typically manifested by the topological Hall effect in magnetotransport measurements. Vrejoiu and Ziese proposed that strong antiferromagnetic interlayer coupling with different magnetocrystalline anisotropies in SrRuO₃/La_{0.7}Sr_{0.3}MnO₃ superlattices can induce the topological Hall effect, as shown in **Figure 11b**.^[122] In these superlattices, the exchange field was estimated to be in the range of several Tesla. Because the ferromagnetic La_{0.7}Sr_{0.3}MnO₃ layer is comparatively soft, the topological Hall effect can develop in the SrRuO₃ layers. Yao et al. observed a temperature-dependent topological Hall effect in SrRuO₃/BiFeO₃ multilayers originating from the broken inversion symmetry near the interface (**Figure 11c**).^[158] Jeong et al. investigated the tunable topological Hall effect in a SrRuO₃/SrTiO₃ superlattice by controlling the repetition number of the supercell structures, as shown in **Figure 11d**.^[90] The competition between the Dzyaloshinskii-Moriya and dipole-dipole interactions can be modulated by the repetition number of SrRuO₃/SrTiO₃ superlattices. Using Monte-Carlo simulations, it was shown that the Dzyaloshinskii-Moriya interaction-stabilized Néel-type skyrmions for low-repetition superlattices and dipole-dipole interaction-stabilized Bloch-type skyrmions for high-repetition superlattices were realized. This resulted in a nonmonotonic dependence of the topological Hall signal depending on the repetition number. By adopting a

strong spin-orbit coupling of $5d$ oxides with ferromagnetic SrRuO_3 , Pang et al. further reported the interfacial Dzyaloshinskii-Moriya interaction in $\text{SrRuO}_3/\text{SrIrO}_3$ superlattices, resulting in a topological Hall effect (arrow in **Figure 11e**).^[163]

It is worth discussing other potential mechanisms of the unconventional Hall signal in SrRuO_3 based heterostructures. Kan et al. suggested that the inhomogeneous magnetoelectric properties of atomically thin SrRuO_3 layers induce a topological Hall-like hump signal as a function of the magnetic field strength.^[185] Yang et al. reported the absence of the hump-like signal in the Hall resistance loops of $\text{SrIrO}_3/\text{SrRuO}_3/\text{SrIrO}_3$ trilayers (top panel of **Figure 11f**), whereas the $\text{SrRuO}_3/\text{SrIrO}_3$ superlattices exhibited a hump structure in the magnetic field-dependent Hall measurements (bottom panel of **Figure 11f**).^[162] This result was interpreted as the unavoidable inhomogeneity in the SrRuO_3 layers within the superlattices. Ziese et al. reported that the hump signal of the $\text{SrRuO}_3/\text{Pr}_{0.7}\text{Ca}_{0.3}\text{MnO}_3$ superlattice can be explained by a combination of two different Hall contributions, which have different temperature dependence and opposite Hall sign, as shown in **Figure 11g**.^[138] The structural modification of $\text{SrRuO}_3/\text{Pr}_{0.7}\text{Ca}_{0.3}\text{MnO}_3$ superlattices separates the tetragonal and orthorhombic structures within the SrRuO_3 layers. Based on their structural characterization, they suggest that combining two different magnetic domains from tetragonal and orthorhombic structures, which have opposite Hall signals, could potentially lead to a topological Hall-like hump signal. Clear experimental observations are necessary for a better understanding of the unconventional Hall signal. Several techniques for imaging the topological non-trivial spin textures includes magnetic force microscopy, scanning tunneling microscopy, Lorentz transmission electron microscopy, and magnetic X-ray scattering. First, magnetic force microscopy and scanning tunneling microscopy have limitations in observing the spin texture of the inner SrRuO_3 layers in some heterostructures because they use a probe tip. Conventional Lorentz transmission electron microscopy still has limitations in high-magnification measurements at temperatures below 150 K and under a magnetic field of about 1 T. We expect that magnetic X-ray scattering is considered the most realistic method for observing the spin texture of the internal SrRuO_3 layers while applying an external magnetic field at low temperatures.^[186] If changes in the superlattice diffraction peak are observed, distinguishable observations can be obtained due to the significantly larger experimental signal provided by the superlattice peak compared to that of thin single films.

As exemplified by the abovementioned intriguing Hall effect and the potential existence of real-space or reciprocal-space magnetic textures,^[74] heterostructures composed of SrIrO₃ and SrRuO₃ have attracted intense attention in the past few years. As this portion of the work has been summarized in detail in a recent review, it is skipped in the current work. It is worthy to note that iridate by itself is another good example showcasing how the intriguing interplay of electron correlation and spin orbit coupling leads to a rich variety of emergent phenomena.^[187-191] In the next Chapter, we will review studies related to iridate-based superlattices other than SrIrO₃/SrRuO₃ heterostructures.

4. 5d SrIrO₃ Based Superlattices

SrIrO₃ is the most notable building block for constructing 5d superlattices because of the readily obtained perovskite structure in thin films. 40 nm is believed to be the critical thickness to keep the high quality of perovskite SrIrO₃ thin film, above which impurity phases like monoclinic SrIrO₃ and Ir-deficiency phases may exist.^[192] Nonetheless, it would be helpful to start with the physics related to Sr₂IrO₄, to better understand the physics of the quasi-isolated square lattice composed of four IrO₆ octahedra, and to better apprehend the motivation for engineering the square lattice in different superlattice structures.^[193]

A well-recognized scenario in iridates is that the octahedral crystal field splits the 5d orbitals into e_g and t_{2g} orbitals. The latter entangles with spin, giving rise to a half-filled $J_{\text{eff}} = 1/2$ doublet on top of a fully occupied $J_{\text{eff}} = 3/2$ quartet. Consequently, although the correlation is much reduced in iridates, it is still strong enough to split the narrow $J_{\text{eff}} = 1/2$ band into an empty upper Hubbard band (UHB) and a full lower Hubbard band (LHB), thereby leading to a considerable Mott gap in single-layer iridates, such as Sr₂IrO₄.^[194, 195] The Mott physics not only accounts for the insulating behavior of Sr₂IrO₄ but also renders the square-lattice iridate as another promising candidate for pursuing next-generation high- T_c superconductivity.^[196, 197] The $J_{\text{eff}} = 1/2$ state also results in novel magnetic properties. The most essential consequence of the strong spin-orbit-entangled state is that simple spin is no longer a good quantum number for describing the electron wave function while the magnetic moments are described within the $J_{\text{eff}} = 1/2$ manifold.^[198] Nevertheless, the quasi-isotropic shape of the $J_{\text{eff}} = 1/2$ state has an equal mixture of d_{xy} , d_{yz} and d_{zx} orbitals (under cubic crystal symmetry). Thus, the intersite magnetic interaction on a straight bond is necessarily isotropic, i.e., a Heisenberg exchange interaction is assumed, similar to the $S = 1/2$ sites. This local rotational symmetry

thus enables a square lattice of $J_{\text{eff}} = 1/2$ states to capture the rich physics of the 2D Hubbard model and 2D Heisenberg model, as schematically shown in **Figure 12**. Previous studies on bulk samples have shed light in this direction but only unveiled the tip of the iceberg owing to the limited flexibility in crystal structure. Table 3 summarizes the reported SrIrO₃ based superlattices depending on the functionality of the partner perovskite oxide layer, which fosters the controllability of emergent correlated behaviors.^[75, 199-218] Next, we review recent exciting findings on superlattices composed of square-lattice iridates by the virtual extensive control of the lattice structure, chemical composition, etc.

4.1 Crystal and Magnetic Structures Manipulation

4.1.1 Manipulating electronic properties via atomic-scale precision control of crystal structure

Figure 13a shows the representative lattice structure of a (SrIrO₃)₁/(SrTiO₃)₁ superlattice, where perovskite SrIrO₃ and SrTiO₃ monolayers are stacked alternately along the *c*-axis. The most important building block in the superlattice is a square lattice composed of corner-sharing IrO₆ octahedra, whereas the SrTiO₃ spacer is cubic and electronically and magnetically inert.^[75, 199, 219-223] Similar to all other perovskite systems, IrO₆ octahedron may rotate around the *c*-axis, which is dubbed as octahedral rotation, or rotate around the diagonal direction in the *ab*-plane leading to an octahedral tilt, as extensively discussed in the previous Chapter for the ruthenate.^[224, 225] Octahedral rotation and tilt play drastically different roles in determining the local/global crystal symmetry of SrIrO₃. As schematically shown in **Figure 13b**, for a square lattice with a staggered octahedral rotation pattern, the global rotational symmetry is the same as that without rotation.^[226] By contrast, the octahedral tilt breaks not only the local inversion symmetry but also the global rotational symmetry (**Figure 13c**).

Matsuno et al. synthesized a series of (SrIrO₃)_{*n*}/(SrTiO₃)₁ superlattices with *n* values ranging from 1 to 4.^[75] Electrical transport measurements suggest that (SrIrO₃)₃/(SrTiO₃)₁ is at the boundary between the semimetallic phase and the Mott insulating phase. All the superlattices feature a half-filled $J_{\text{eff}} = 1/2$ state thanks to the absence of interfacial charge transfer between Ir and Ti. The degradation of the insulating state with increasing *n* indicates that the electron correlation was successively suppressed due to the increasing SrIrO₃ spacer thickness. This control of quantum confinement was later confirmed by Kim et al., based on density functional theory calculations. The study found that the vertical charge hopping within the multiple-layer SrIrO₃ spacer increased the $J_{\text{eff}} = 1/2$ bandwidth, which in turn reduced the

effective electron correlation.^[200] The $(\text{SrIrO}_3)_1/(\text{SrTiO}_3)_1$ superlattice thus represents as a rare artificial layered structure for simulating the 2D single-band Hubbard model.^[201] To introduce additional tunability to the layered structure, Hao et al. systematically changed the SrTiO_3 thickness while leaving SrIrO_3 only a monolayer thick.^[199] The $(\text{SrIrO}_3)_1/(\text{SrTiO}_3)_2$ and $(\text{SrIrO}_3)_1/(\text{SrTiO}_3)_3$ with thicker SrTiO_3 spacers are indeed more insulating than $(\text{SrIrO}_3)_1/(\text{SrTiO}_3)_1$ with a SrTiO_3 monolayer spacer, similar to the case of SrRuO_3 (see Section 3.4.2), indicating that the charge-hopping channel across the SrTiO_3 spacer is finite and controllable, although the conduction band of SrTiO_3 is approximately 2 eV higher than the upper $J_{\text{eff}}=1/2$ Hubbard band.^[75, 202] The charge-hopping channels across the SrTiO_3 in the superlattice structure were reaffirmed in a subsequent theoretical work.^[202]

4.1.2 Magnetic Structure Manipulation

The superlattice series also exhibits an interesting magnetic phase diagram. While all insulating superlattices are antiferromagnetically ordered at the base temperature, the transition temperature T_N can be changed by over two orders of magnitude.^[75] As shown in **Figure 14a**, $(\text{SrIrO}_3)_1/(\text{SrTiO}_3)_1$ has a maximum T_N of approximately 150 K, which decreases monotonically with increasing SrIrO_3 layer thickness. A well-defined antiferromagnetic transition is almost unobservable in the semimetallic $(\text{SrIrO}_3)_4/(\text{SrTiO}_3)_1$. On the other hand, T_N decreased with increasing the SrTiO_3 layer thickness, as shown in **Figure 14b**. This difference indicates that the SrIrO_3 layer thickness alone does not determine T_N in the superlattices. A possible scenario is that the interlayer coupling decreases by separating the neighboring SrIrO_3 layers. In fact, the interlayer coupling is speculated to decrease exponentially with increasing distance from the neighboring magnetic layer.^[227] This is consistent with the significantly reduced T_N from ~ 150 to 40 K when the spatial distance between neighboring SrIrO_3 layers increased from a SrTiO_3 monolayer to a SrTiO_3 bilayer.^[199] Additionally, the T_N was found to be approximately the same when increasing the SrTiO_3 slab from bilayer to trilayer, which is indicative of reaching the regime where the 2D magnetic ordering is predominantly stabilized by magnetic anisotropy, which will be discussed in more detail in Section 4.3.2.

The magnetic anisotropy in square-lattice iridates is highly sensitive to dimensionality. The magnetization and magnetic scattering measurements suggest that $(\text{SrIrO}_3)_1/(\text{SrTiO}_3)_1$ has an easy plane anisotropy,^[75] similar to the bulk monolayer-systems Sr_2IrO_4 and Ba_2IrO_4 .^[228] To resolve the magnetic anisotropy of $(\text{SrIrO}_3)_2/(\text{SrTiO}_3)_1$, Meyers et al. measured the azimuthal

angle dependence of the magnetic peak using the magnetic resonant scattering technique.^[203] A key difference between the easy-plane and easy-axis anisotropy is that the easy-plane magnetic moments can be completely removed from the scattering plane, giving rise to the zero intensity of magnetic peak, while the magnetic peak intensity of an easy-axis system is nonzero at any finite azimuthal angle.^[228-232] In parallel to the easy-axis model, the authors found that the magnetic peak is always observable in the studied azimuthal range. This result demonstrates that $(\text{SrIrO}_3)_2/(\text{SrTiO}_3)_1$ has a dominant easy-axis anisotropy,^[203] that is similar to that of $\text{Sr}_3\text{Ir}_2\text{O}_7$.

By virtue of the dimensionality controlled magnetic anisotropy, Gong et al. prepared an interesting hybrid superlattice structure with an alternating stacking of $(\text{SrIrO}_3)_1/(\text{SrTiO}_3)_1$ and $(\text{SrIrO}_3)_2/(\text{SrTiO}_3)_1$ superlattices, as schematically showing in **Figures 14d** and **14e**.^[204] It is found that the hybrid superlattice orders only at a single temperature close to the Neel temperature of $(\text{SrIrO}_3)_2/(\text{SrTiO}_3)_1$, thus suggesting a uniform magnetic structure. However, detailed magnetic scattering measurements revealed that the hybrid superlattice has a dominant canted easy plane anisotropy similar to that of $(\text{SrIrO}_3)_1/(\text{SrTiO}_3)_1$. This result suggests that the magnetic behavior of the hybrid superlattice is not a simple addition to the magnetic order of the monolayer and bilayer superlattices. In contrast, integrating the monolayer member and bilayer member of the Ruddlesden-Popper iridates into a single structure leads to two separate ordering temperatures and the addition of orthogonal anisotropy.^[233] The difference between the hybrid superlattice and hybrid Ruddlesden-Popper structure could be ascribed to the extra in-plane half-unit-cell slide between the monolayer and bilayer slabs in the Ruddlesden-Popper structure, which suppresses monolayer-bilayer magnetic coupling.^[204] Another possible contribution is that the bilayer in the artificial superlattice is much closer to the spin-flop transition than its Ruddlesden-Popper counterpart.^[179]

In particular, square-lattice iridates have magnetic anisotropy primarily owing to the high-order perturbation from the virtual hopping between $J_{\text{eff}} = 1/2$ and $J_{\text{eff}} = 3/2$ states in the presence of a nonzero Hund's coupling. The induced pseudo-dipolar interaction produces a predominantly out-of-plane magnon gap, the sign of which varies with tetragonal distortion. This spin model explains the easy-plane anisotropy of Sr_2IrO_4 well and predicts an easy-axis antiferromagnetic state with IrO_6 octahedra being heavily elongated along the c -axis.^[198] However, the predicted magnon gap is much smaller than that measured using resonant

inelastic X-ray scattering in $\text{Sr}_3\text{Ir}_2\text{O}_7$.^[234] Kim et al. reported that compared to single-layer iridates, an additional interlayer pseudo-dipolar interaction must also be considered in the bilayer system, which eventually leads to a far larger anisotropy term that favors c -axis anisotropy irrespective of tetragonal distortion.^[231, 234] Meyers et al. found in a superlattice system, the octahedral tilt, albeit small in the $(\text{SrIrO}_3)_2/(\text{SrTiO}_3)_1$, significantly reduced the interlayer pseudo-dipolar interaction. Thus, although $(\text{SrIrO}_3)_2/(\text{SrTiO}_3)_1$ still hosted c -axis anisotropy similar to that of the bulk, it was closer to the phase boundary between the easy-plane and easy-axis magnetic phases, as shown in **Figure 14c**.^[203] Nevertheless, Gong et al. found that the octahedral tilt of the hybrid superlattice was smaller than that of $(\text{SrIrO}_3)_2/(\text{SrTiO}_3)_1$, indicating that the interlayer pseudo-dipolar interaction is not the primary reason for the dominant easy-plane anisotropy in the bilayer slab. A bilayer-Hubbard model analysis revealed that a moderate correlation strength also leads to a giant magnon gap and suggested that the bilayer system in the intermediate regime could be the long-sought excitonic insulator.^[235]

4.2 Enhancing and Manipulating $J_{\text{eff}} = 1/2$ Pseudospin Fluctuations

4.2.1 Extreme Spin Fluctuations in the 2D Limit

In general, spin fluctuation in the 2D limit is much stronger than that in 3D materials, and the critical behavior of 2D spin fluctuation depends sensitively on magnetic anisotropy.^[236, 237]

For example, the correlation length diverges in a power-law manner when approaching the ordering temperature in the presence of Ising-type magnetic anisotropy. The divergence is faster if the easy-axis anisotropy is switched to the easy-plane anisotropy. The spin fluctuation then reaches an extreme situation of an exponential-type diverging trend when the anisotropy is zero. According to the Mermin-Wagner theorem, the spin fluctuation of 2D isotropic magnets is so strong that any long-range order will be melted at a non-zero temperature owing

to $|M| < \frac{C}{\sqrt{T}} \cdot \frac{1}{|\ln \sqrt{|h|}|}$, where M represents net magnetization or staggered magnetization, h

denotes a uniform field or staggered field in ferromagnetic or antiferromagnetic systems, and C is a constant.^[238] Extreme spin fluctuation offers an ideal platform for achieving a highly

efficient spin response, which is beneficial for designing ultrafast spintronic devices.

Additionally, spin fluctuation in the 2D square lattice is recognized to be closely related to the unconventional superconductivity in cuprates^[239, 240] and is essential for advancing fundamental physical understanding.

4.2.2 Staggered Field Effect in Antiferromagnets

In certain antiferromagnetic materials with locally broken inversion symmetry, an external magnetic field may behave effectively as a staggered field to linearly couple to the antiferromagnetic order parameter. For example, in Cu benzoate, the Dzyaloshinskii–Moriya interaction can be written in the form $H_{DM} = \sum_j (-1)^j \vec{D} \cdot (\vec{S}_j \times \vec{S}_{j+1})$, where \vec{D} is the Dzyaloshinskii–Moriya vector and \vec{S}_j is the spin operator at site j . Here, factor $(-1)^j$ denotes the staggered Dzyaloshinskii–Moriya pattern along the spin chain. After rotation along the \vec{D} direction through an alternating angle $\alpha/2$, where $\tan \alpha = D/J$, i.e., $\vec{S}_j^+ \rightarrow \vec{S}_j^+ \cdot e^{i\alpha/2}$, $\vec{S}_{j+1}^+ \rightarrow \vec{S}_{j+1}^+ \cdot e^{-i\alpha/2}$, the Dzyaloshinskii–Moriya term can be absorbed into the exchange interaction, giving rise to an effective Heisenberg-like model.^[226] In 2D square-lattice systems, the Hamiltonian transformation can be thought of as the conversion of the global spin frame (**Figure 15a**) to the twisted local frame (**Figure 15b**). Considering the Zeeman effect under an external field h along the x -direction $H_{Zeeman} = -h \sum_j S_j^x$ in the redefined spin frame, one will arrive at $H_{Zeeman} = -h \cos \frac{\alpha}{2} \sum_j \tilde{S}_j^x - h \sin \frac{\alpha}{2} \sum_j (-1)^j \tilde{S}_j^y$. Clearly, a staggered field, linearly coupled with the AFM order parameter, is generated along the y -axis. Furthermore, the staggered field effect is governed by D/J , which generally increases with spin orbit coupling in general. Note that for a 1D spin chain, the staggered pattern of the Dzyaloshinskii–Moriya interaction on neighboring bonds does not break the global rotation symmetry.

4.2.3 Manipulating 2D Extreme Antiferromagnetic Fluctuations

The staggered field effect enables direct control of antiferromagnetic fluctuations. As mentioned in Section 4.1.2, $(\text{SrIrO}_3)_1/(\text{SrTiO}_3)_2$ and $(\text{SrIrO}_3)_1/(\text{SrTiO}_3)_3$ are at the 2D limit because the almost unchanged T_N with further suppressed interlayer coupling.^[199, 241] The in-plane staggered rotation pattern of IrO_6 octahedra and the large spin orbit coupling gives rise to a substantial staggered field upon application of an in-plane magnetic field. As shown in **Figure 15c**, the crossover temperature T_0 , which can be treated as the ordering temperature the purpose of practical application, increases rapidly with the in-plane magnetic field. This observation is striking and even counterintuitive, considering that antiferromagnets are generally resilient to external magnetic fields.^[242] The giant magnetic response was ascribed to the unique combination of a hidden $\text{SU}(2)$ symmetry protected by the global crystal

rotational symmetry, a large staggered field effect due to the strong spin orbit coupling, and a vanishingly small interlayer coupling due to the quasi-2D nature of the artificial structure.

The sharp increase in the ordering temperature with the magnetic field indicates that the disordered state above T_0 can be transitioned into a long-range order state by applying certain magnetic fields, thus offering a novel approach for designing magnetic field switching of antiferromagnetic order, as shown in **Figure 15d**. The magnetic logic bit (on/off) is typically defined by the orientation of the order parameter in the magnetic ordering state in antiferromagnetic spintronics.^[243-246] This is distinct from the above study, where the *on* state does not rely on the specific spin orientation in the ordered state, whereas the *off* state is simply a trivial disordered state. Moreover, the key to realizing such an efficient staggered response to a uniform stimulus is the SU(2)-symmetry-preserved Dzyaloshinskii–Moriya interaction, which can be achieved in various antiferroic materials via sophisticated lattice engineering strategies. This finding may stimulate more exciting work in exploring and realizing advanced nanoscale devices with antiferroic materials, which are much abundant but are largely unexplored.

4.3 Enhancing and Manipulating $J_{\text{eff}} = 1/2$ Charge Fluctuations

4.3.1 Charge Fluctuations in the Intermediate Regime

The spin and charge degrees of freedom are entangled in the half-filled single-band Hubbard system because charge localization is tied to the formation of local magnetic moments.^[201, 247] Thus, the local magnetic moments are thus effectively local particle–hole pairs. Correspondingly, breaking up a pair by exciting the charges into the electron–hole continuum above the charge gap annihilates the local magnetic moment (i.e., longitudinal spin fluctuations), and vice versa. In the strong-coupling Mott limit, the local magnetic moments survive well above T_N because the charge degree of freedom remains frozen until the thermal fluctuations substantially disturb the Mott gap, which can be several orders of magnitudes higher than T_N . Consequently, the spin-charge fluctuation is typically weak in this regime. In the weak-coupling Slater limit, the system is metallic above T_N without the local magnetic moments, thus resulting in weak spin-charge fluctuations. Compared to the two limits, the intermediate coupling regime has an optimum spin-charge fluctuation because both local moments and charge carriers exist above T_N . A generic phase diagram of a half-filled single-band system is schematically drawn in **Figure 16a**. Clearly, electron correlation is the key to

exploring the emergent phenomena associated with charge fluctuations in a single-band Hubbard system.

4.3.2 Modulating Electron Correlation via Epitaxial Strain

Epitaxial strain is one of the most vital and readily accessible knobs for modulating the effective electron correlation in thin-film and heterostructure studies. Kim *et al.* predicted that the $J_{\text{eff}} = 1/2$ bandwidth of the $(\text{SrIrO}_3)_1/(\text{SrTiO}_3)_1$ superlattice decreases with increasing tensile strain.^[219] Kim *et al.* confirmed the $J_{\text{eff}} = 1/2$ band feature in the superlattice, as shown in Figure 16b, and unveiled that the substantial strain effect in $(\text{SrIrO}_3)_1/(\text{SrTiO}_3)_1$ as compared to Sr_2IrO_4 arises from the additional vertical hopping channels in the former,^[202] as schematically shown in **Figure 16c**. Kim *et al.* later expanded the strain study on $(\text{SrIrO}_3)_m/(\text{SrTiO}_3)_1$ with $m > 1$.^[200] Ranging from -4% to 4% of the epitaxial strain, the authors found that the electronic structure, albeit slightly different owing to the different stacking patterns of the superlattice series, displayed a similar strain dependence.

Experimentally, Yang *et al.* prepared a series of $(\text{SrIrO}_3)_1/(\text{SrTiO}_3)_1$ superlattices on different substrates to implement variable epitaxial strains of 0, -0.95%, and -1.06%.^[248] With X-ray absorption spectroscopy measurements at the O *K*-edge, the authors found that the $J_{\text{eff}} = 1/2$ single-band feature was preserved under epitaxial strain. In the above X-ray absorption measurements, the intensity difference between the out-of-plane and in-plane channels was considered to be a measure of the relative hybridization strength of Ir with planar oxygen.^[249, 250] Notably, the X-ray absorption intensity in the out-of-plane channel was always larger than the in-plane signal, indicating a dominant hybridization between Ir and planar oxygen in all the superlattices (**Figure 16d**). By extracting the X-ray linear dichroism, which is the difference spectra between the out-of-plane and in-plane channels, the authors unveiled that in-plane hybridization systematically increased with compressive strain. This is strong evidence that the effective electron correlation in superlattices decreases monotonically with increasing compressive strain.

Electronic correlation modulation was also captured in the electric transport and magnetic measurements. Although all the superlattices had an insulating ground state, the insulating behavior was weakened in the compressed superlattices, confirming that the reduced electron correlation is consistent with the electronic structure. Interestingly, the authors observed an emergent high-temperature metallic phase in $(\text{SrIrO}_3)_1/(\text{SrTiO}_3)_1$ with the largest

compressive strain. Moreover, all the superlattices had the same antiferromagnetic structure while the Neel temperature T_N decreased monotonically with increasing compressive strain. Intuitive, half-filled single-band systems can be ascribed to Mott insulators because of the insulating state being established well above T_N .^[247] However, the reduced T_N , due to enhanced electron hopping, clearly contradicts the expectation of the exchange interaction $J \propto 4t^2/U$ (t and U denote electron hopping and correlation, respectively) at the strong coupling limit.^[251] The magnetic peak intensity was quantified at the base temperature and revealed that the antiferromagnetic order parameter decreased monotonically with compressive strain. The fact that the antiferromagnetic order parameter, antiferromagnetic ordering temperature, and strength of the insulating behavior decrease simultaneously with the effective electron correlation (**Figure 16e**), revealed that charge fluctuations play a dominant role in the stability of the antiferromagnetic ordering. This is a key feature of Slater-type insulators in the weak-coupling limit.^[247, 252] The coexistence of characteristics of weak and strong coupling limits indicates that the (SrIrO₃)₁/(SrTiO₃)₁ superlattice system should be within the Slater-Mott crossover regime. In contrast to these two limits, knowledge about the intermediate regime is very limited,^[252] which is discussed in more detail in the next section.

4.3.3 Manipulating Charge Fluctuations via Staggered Field Effect

To explore the intermediate regime in depth, Hao et al. performed a comprehensive magnetotransport study of (SrIrO₃)₁/(SrTiO₃)₁ grown on a SrTiO₃ substrate.^[253] As mentioned in Section 4.3.1, the intermediate regime (or the Slater-Mott crossover regime) hosts energetic charge fluctuations, which effectively lead to longitudinal spin fluctuations.^[248] The intriguing spin-charge interplay causes a notable anomaly in the insulating resistivity when cooling through T_N . After applying an in-plane magnetic field, the authors observed a substantial magnetoresistance effect above T_N . Positive magnetoresistance is unusual because transverse spin fluctuations typically plays a dominant role in antiferromagnetic semiconductors, and a negative magnetoresistance effect is commonly observed.^[254, 255] In addition, magnetoresistance above T_N exhibits a similar temperature dependence of the staggered susceptibility, which increases quickly with temperature approaching T_N , as shown in **Figure 16f**. Another interesting observation is the anisotropic characteristic of the anomalous magnetoresistance, i.e., a large magnetoresistance is observed when the magnetic field is parallel to the plane, whereas the out-of-plane magnetoresistance is almost unobservable. Note that because of the finite antiferromagnetic order parameter, a staggered field effect also exists in the intermediate regime, which is expected to stabilize the

localized magnetic moments and enhance the particle-hole binding. As a large staggered field is only produced in the presence of an in-plane magnetic field owing to the in-plane net magnetic moment, this observation demonstrates that magnetoresistance originates from the suppression of spin-charge fluctuations under staggered magnetic fields.

Further insights into the anomalous magnetoresistance were gained through theoretical simulation using a 2D model built on a $J_{\text{eff}} = 1/2$ square lattice. The authors reported that a staggered field increases the size of the antiferromagnetic order parameter by suppressing longitudinal spin fluctuation. The effect is most significant around T_N , where the spin susceptibility is maximized. The carrier density is strongly suppressed owing to the staggered magnetic field and reaches its minimum around T_N . The carrier density reduction renders the anomalous magnetoresistance even more peculiar than the carrier mobility-driven magnetoresistance effects in most cases.^[256-261] The anomalous magnetoresistance thus probes the longitudinal spin fluctuations by virtue of the spin-orbit coupling-induced staggered field effect, and offers a novel pathway to control the binding energy of the fluctuating particle-hole pairs via a magnetic field in the Slater-Mott crossover regime.

4.4 Topology-Correlation Interplay in Artificial Iridates

The intermediate regime is interesting not only because of the coexistence of spin and charge fluctuations but also because of the possibility of integrating both electronic topology and correlation in a single system. The concept of electronic topology was developed with the prediction and discovery of a variety of symmetry-protected surface states, edge states, etc.^[262, 263] These studies focused primarily on noninteracting systems that can be well understood in single-particle band pictures. Nonetheless, the interaction between electrons is typically nonzero in real materials and can sometimes lead to emergent phenomenon beyond band structure prediction. A well-known example is the Mott insulating state in 2D half-filled single-band systems, for which non-interacting band theory predicts a good metal. Thus, whether and how the electronic topology manifests in correlated systems is generally unknown. This is particularly true for the intermediate regime, where both the single-electron approach in the weak-coupling limit and the superexchange approach in the strong-coupling limit fail to capture the energetic spin and charge excitations. It is believed that designer electronic topology and electronic correlation based on artificial heterostructures are promising routes to understand the intriguing interplay.^[264]

As discussed in Section 4.3.2, (SrIrO₃)₁/(SrTiO₃)₁ is a realistic 2D half-filled Hubbard model system in the intermediate regime. To implement a nontrivial electronic topology, Yang et al. prepared (SrIrO₃)₁/(CaTiO₃)₁ superlattices on SrTiO₃ substrates.^[206] The key difference between the lattice structures of (SrIrO₃)₁/(CaTiO₃)₁ and (SrIrO₃)₁/(SrTiO₃)₁ is the realization of a large octahedral tilting in the former by reducing the tolerance factor. The effective Hamiltonian of the distorted 2D square lattice can be written as:

$$H = -t \sum_{\langle ij \rangle} \sum_{\alpha, \beta} \left[c_{i\alpha}^\dagger (e^{i\theta \mathbf{d}_{ij} \cdot \boldsymbol{\sigma}})_{\alpha\beta} c_{j\beta} + h.c. \right] + U \sum_i n_{i\uparrow} n_{i\downarrow} \quad (1),$$

where the first term accounts for the nearest-neighboring $\langle ij \rangle$ hopping, as schematically shown in **Figure 17a**, $c_{i\alpha}^\dagger$ ($c_{i\alpha}$) is the creation (annihilation) operator of a $J_{\text{eff}} = 1/2$ electron with spin α on site i , $\boldsymbol{\sigma}$ is the vector of Pauli matrices, and U is the onsite electron-electron repulsion. In contrast to the typical 2D Hubbard model, electron hopping between neighboring sites is mediated by a finite SU(2) gauge field, $e^{i\theta \mathbf{d}_{ij} \cdot \boldsymbol{\sigma}}$. Octahedral rotation contributes to the staggered normal component of the gauge field, whereas octahedral tilt results in planar components. Unlike the rotation, the octahedral tilt breaks the global fourfold rotational symmetry such that the planar components cannot be gauged simultaneously on the square lattice. This effect can be intuitively captured as the gauge-invariant flux ϕ of any closed path of hopping, as shown in **Figure 17b**. In the absence of correlation, the model leads to a Dirac semimetal, and the nonzero flux emerges in the momentum space as a Berry phase, which is the main source of the spontaneous Hall effect.^[265, 266] In the strong-coupling limit, the flux gives rise to Ising anisotropy along \mathbf{d}_{\square} .

Consistent with the model analysis, a large anomalous Hall effect below T_N was observed. Interestingly, both the saturated and remnant anomalous Hall conductivities exhibited a nonlinear temperature dependence, i.e., they first increased quickly and then began decreasing with cooling, as shown in **Figure 17c**. This unconventional behavior indicates that the anomalous Hall effect is governed by physical quantities that compete with each other. Indeed, the authors observed that the anomalous Hall angle σ_{yx}/σ_{xx} , which measures the strength of the charge deflection, increased with cooling, whereas the anomalous Hall coefficient $S_H = \sigma_{yx}/M_S$ which is proportional to the effective charge carrier density, had an opposite dependence, as shown in the inset of Figure 17c. Thus, the intrinsic anomalous Hall effect suggests that the impact of electronic topology extends to a Mott insulator in the moderately correlated regime. This is the central idea of the intermediate regime, where

delocalized antiferromagnetic moments give rise to activated charge carriers and the two physical quantities increase at the expense of each other.

At the base temperature, the authors found that the magnetic structure indeed had an easy axis along \mathbf{d}_{\square} , as shown in the inset of **Figure 17d**. Nevertheless, through resonant inelastic scattering measurements, the spin gap was found to be surprisingly large (~ 85 meV), close to the giant magnon gap of the bilayer iridate $\text{Sr}_3\text{Ir}_2\text{O}_7$.^[234] The gap size was far larger than expected from the linear spin wave theory in the strong-coupling limit and can be understood only using a Hubbard model with a moderate correlation strength. The nonmonotonic anomalous Hall effect and the giant spin gap demonstrate that the interplay between the electronic topology and electronic correlation is so rich that the emergent phenomena are typically beyond the theorems relating to the weak-coupling or strong-coupling limit.

In complementary to the intrinsic anomalous Hall effect driven by the same group of $J_{\text{eff}} = 1/2$ electrons that form the antiferromagnetic Mott insulating state through symmetry engineering in a 2D square-lattice iridate block, the anomalous Hall effect was also observed in superlattices composed of SrIrO_3 and other magnetic compounds, as is discussed in the next section.

4.5 Superlattices Composed of SrIrO_3 and Magnetic Compounds

The anomalous Hall effect is typically observed in materials with SOC and broken time reversal symmetry.^[265] Although SrIrO_3 features a large spin-orbit coupling and theory predicts the existence of multiple nontrivial electronic topologies upon breaking a certain crystal symmetry,^[267] the material by itself does not break the time reversal symmetry. Thus, a large effort has been devoted to introducing long-range magnetic order in iridates by heterostructuring SrIrO_3 with different magnetic compounds.

For example, Nichols et al. synthesized a series of superlattices composed of SrIrO_3 and an antiferromagnetic insulator SrMnO_3 .^[212] In contrast to the two mother phases, the authors found that $(\text{SrIrO}_3)_1/(\text{SrMnO}_3)_1$ displayed a large net magnetization with the easy axis along the film normal direction. The interfacial ferromagnetism was ascribed to the charge transfer between Ir and Mn. In parallel to the spontaneously broken time-reversal symmetry, the anomalous Hall effect was observed below the magnetic ordering temperature. As shown in **Figure 18a**, the anomalous Hall effect is reduced and eventually vanished with increasing

layer thickness, highlighting the crucial role of the interface in the emergent ferromagnetism. Skoropata et al. replaced SrMnO_3 with LaMnO_3 in the aforementioned superlattice structures and realized a potential topological Hall effect by engineering the interfacial Dzyaloshinskii–Moriya interaction.^[216] Recently, Gu et al. exploited CaMnO_3 as the main constituent of a superlattice composed of SrIrO_3 .^[218] The authors observed a metal to nonmetal crossover with decreasing layer thickness (**Figure 18b**), again highlighting the crucial role of the Ir/Mn interface in modulating the global electric transport property. In contrast to building a SrIrO_3 based superlattice with magnetic conductors, Jaiswal et al. prepared superlattices with SrIrO_3 and LaCoO_3 , which is a magnetic insulator at low temperatures.^[213] They reported a large anomalous Hall effect when SrIrO_3 was in direct contacts with LaCoO_3 at the atomic scale, whereas such effect was absent when SrIrO_3 and LaCoO_3 layers were separated by a thick SrTiO_3 spacer (**Figure 18c**). The authors argued that the anomalous Hall effect is due to proximity-induced magnetism in the SrIrO_3 layer.

In addition to the end members of RMnO_3 , Yoo et al. constructed heterostructures with SrIrO_3 and $\text{La}_{0.7}\text{Sr}_{0.3}\text{MnO}_3$,^[207] which were best optimized for the double-exchange-dominated ferromagnetism. In addition to the ordinary Hall effect, the authors extracted the anomalous Hall component of the superlattices. With a systematic variation in the layer thickness, they found that the anomalous Hall resistivity always scales linearly with the square of the longitudinal resistivity, as shown in **Figure 18d**.^[265] The anomalous Hall effect was ascribed to proximity-induced magnetism in the SrIrO_3 layer, whereas the intriguing double-SrO layer at the Ir/Mn interface plays a subtle role in mediating the exchange interaction. Yi et al. found that attaching $\text{La}_{0.7}\text{Sr}_{0.3}\text{MnO}_3$ to SrIrO_3 at the atomic scale leads to a large variation in magnetic anisotropy.^[208, 210] In addition to $\text{SrIrO}_3/\text{La}_{0.7}\text{Sr}_{0.3}\text{MnO}_3$ superlattices, Yi et al. prepared superlattices composed of SrIrO_3 and $\text{La}_{0.8}\text{Sr}_{0.2}\text{MnO}_3$.^[211] Interestingly, the authors observed a reversible phase transformation with a lattice change as large as 7% at room temperature using ionic liquid gating. The phase transformation is associated with a clear modulation of the electronic, magnetic, and optical properties due to the reversible transfer of oxygen and/or hydrogen ions. This work further demonstrates that digital superlattices usually hosts emergent functionalities that have not been seen in the mother phases or in their solid solutions.

4.6 Superlattices Composed of Iridates Other Than SrIrO_3

As the 3D end member of the iridate Ruddlesden-Popper family, SrIrO_3 has a simple perovskite structure similar to most functional oxides and is widely used to construct iridate-based superlattices. With the development of epitaxy techniques, studies have also been conducted on superlattices composed of other iridates, such as Sr_2IrO_4 and CaIrO_3 .

Liu et al. grew superlattices with alternating Sr_2IrO_4 and SrTiO_3 layers.^[268] The superlattices were found to have an emergent magnetoelectric phase transition, probably due to the double SrO layers at the interface (**Figure 19a**). By replacing SrTiO_3 with BaTiO_3 , the magnetoelectric transition was substantially enhanced, with a pronounced magnetoelectric coefficient. Gruenewald et al. integrated Sr_2IrO_4 and LaSrGaO_4 atomically in a planar manner and realized 1D IrO_2 stripes.^[269] From resonant inelastic X-ray scattering measurements, as shown in **Figure 19b**, the authors found that the 1D stripes clearly enhanced exchange interactions and confined orbital excitations compared with Sr_2IrO_4 . In addition to the interesting dielectric and magnetic behaviors observed on Sr_2IrO_4 based superlattices, Xu et al. found an enhanced anisotropic magnetoresistance effect in superlattices composed of Sr_2IrO_4 and $\text{La}_{0.7}\text{Sr}_{0.3}\text{MnO}_3$.^[270] By modulating the magnetic field direction, a nonvolatile memory based on the AMR effect was realized.

Similar to SrIrO_3 , CaIrO_3 is semimetallic and can be stabilized into the perovskite phase using epitaxy.^[271] Recently, CaIrO_3 has been increasingly used to construct atomic-scale superlattices. For example, Lim et al. prepared a series of $\text{CaIrO}_3/\text{SrTiO}_3$ superlattices and found enhanced anisotropic magnetoresistance as compared to $\text{SrIrO}_3/\text{SrTiO}_3$ superlattices.^[272] Interestingly, the authors found that the anisotropic magnetoresistance of $(\text{CaIrO}_3)_1/(\text{SrTiO}_3)_1$ was maximized at 45° , whereas the largest anisotropic magnetoresistance of $(\text{SrIrO}_3)_1/(\text{SrTiO}_3)_1$ occurred at 90° . This anisotropic magnetoresistance difference indicates that replacing SrIrO_3 with CaIrO_3 in the superlattice causes a substantial change in the magnetic structure, as shown in **Figure 19c**. Fourfold anisotropic magnetoresistance was also observed in a recent study by Vagadia et al., who constructed multiple superlattices composed of CaIrO_3 and CaMnO_3 .^[273] The anisotropic magnetoresistance magnitude was found to be as high as 70%, which is approximately two orders of magnitude greater than the value reported for $(\text{CaIrO}_3)_1/(\text{SrTiO}_3)_1$, as shown in **Figure 19d**. This unprecedentedly high anisotropic magnetoresistance was ascribed to the combination of a strong biaxial anisotropy and a metamagnetic transition.

5. Conclusions and Outlook

Ruthenate- and iridate-based oxide superlattices exemplify the power of bottom-up synthesis by heteroepitaxial growth in overcoming the material bottleneck in solid-state chemistry. Unlike the large number of material families of $3d$ transition metal oxides, studies on $4d$ and $5d$ systems have been limited to a few compounds available in bulk form. Artificial crystals built from atomically thin SrRuO_3 and SrIrO_3 demonstrate a route for creating coherent layered structures that are unobtainable using conventional protocols. A particularly important aspect of the reported studies is that one can create analogous systems to the known bulk compounds. The analogy is not only in the layered character of the crystal structure but also in the physics behind the electronic and magnetic properties. It is crucial to make such comparisons when designing artificial crystals because they determine the crystal unit that play an essential role in the unified picture of the physical properties. A closely related direction is the interface and heterostructures of $3d$ and $4d$, $3d$ and $5d$, and $4d$ and $5d$ oxides. One advantage of such systems is that they bring together different degrees of correlation and spin-orbit coupling. Although some studies have adopted this direction, the complexity of such systems often renders difficulty in disentangling the roles of the different layers in driving the observed properties, particularly when the layers are unit-cell thin. The superlattices with quantum-confined structures of atomically thin SrRuO_3 and SrIrO_3 layers fill the gap in understanding. They established that the ground state and properties of a monolayer of SrRuO_3 and SrIrO_3 are favorable, which serves as the basis for using them as building blocks for more complex structures. This allows the reexamination of ultrathin superlattices with $3d$ oxides and rejuvenates this research direction. It also sets a blueprint for developing new superlattices of this kind. Note that the analogy between the superlattice and bulk does not mean that the properties of the artificial crystals are the same as those of the bulk in every aspect. Instead, the key is to be able to identify both their similarities and differences and understand the reasons behind them. This builds the foundation for further exploiting the additional structural degrees of freedom afforded by the superlattice to generate structural variants beyond the bulk compounds and stabilize new phases.

An immediate benefit of superlattice synthesis is the possibility of obtaining a large variety of oxide systems with strong spin-orbit coupling, which is the key property that distinguishes $4d$ and $5d$ systems from their $3d$ counterparts. This opens the door to exploring topology-driven physics and properties of oxides through structural and symmetry engineering. This is an

important future direction for this class of systems. Proposals of topological designs of oxide superlattices have indeed been put forward for about ten years. However, numerous predictions are based on the single-particle picture, which may not be realistic because of the significant electronic correlation remaining in the $4d$ and $5d$ orbitals. This characteristic could result in $4d$ and $5d$ oxides in a regime where topology and correlation coexist and interact with each other. For instance, one of the most important consequences of correlation is magnetism, and the role of spin-orbit coupling in correlated systems has traditionally been viewed as a perturbation that controls magnetic anisotropy. On the other hand, if spin-orbit coupling leads to a nontrivial electronic topology, magnetically driven topological states may emerge, and their emergence can very well depend on magnetic anisotropy. The intrinsic anomalous Hall effect is an excellent example, in which both the Berry phase and magnetic order with a proper easy axis are necessary. Therefore, one may consider the anomalous Hall effect as a combined result of spin-orbit coupling, correlation, and crystal symmetry, which can be implemented in artificial crystals by design. Even in the strong correlation limit, the impact of topology may still survive but in a different form because the spin-dependent hopping that is responsible for topology is mapped to the Dzyaloshinskii–Moriya interactions. In fact, exchange magnetic anisotropy is a result of Dzyaloshinskii–Moriya interactions, which are a vital source of magnetoelectricity in oxides. Artificial crystals of $4d$ and $5d$ electrons may bridge several different research fields.

From the application point of view, creating magnetic oxides with substantial spin-orbit coupling is crucial for the development of spintronics. Future directions include realizing magnetic materials with especially large magnetic anisotropy for nonvolatile memory and developing efficient spin charge conversion for energy harvesting. Finally, there is great potential for applying new experimental methods from parallel developments. Examples include ionic-liquid gating and freestanding membranes. The superlattice structure could have the advantages of sustaining the lattice when the ions move in and out. Broadly stated, this may have significant implications in catalysis studies because precious metals are known to be good catalysts. Controlling the $4d$ and $5d$ electronic states in artificial crystals can lead to improved performances.

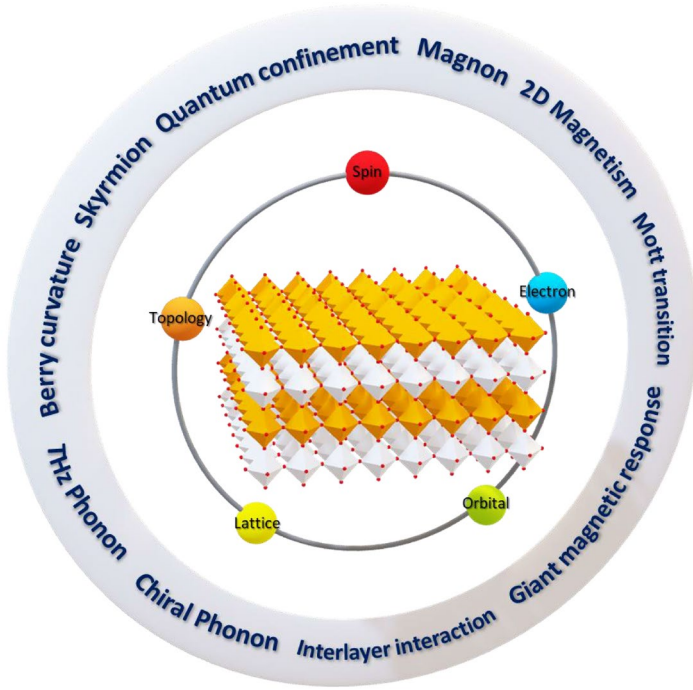


Figure 1. Schematic summary of artificial $4d$ and $5d$ oxide superlattices with their versatile functionalities.

Table 1. Correlation strength in $3d$, $4d$, and $5d$ transition metal oxide superlattices. The symbols U , λ , and Δ represent on-site Coulomb interaction, spin-orbit coupling, and crystal field splitting energy, respectively.

Elements	U (eV)	λ (eV)	Δ (eV)
$3d$	5 ~ 7	0.01 ~ 0.10	1 ~ 2
$4d$	0.5 ~ 3	0.1 ~ 0.3	2 ~ 3
$5d$	0.4 ~ 2	0.1 ~ 1	3 ~ 4

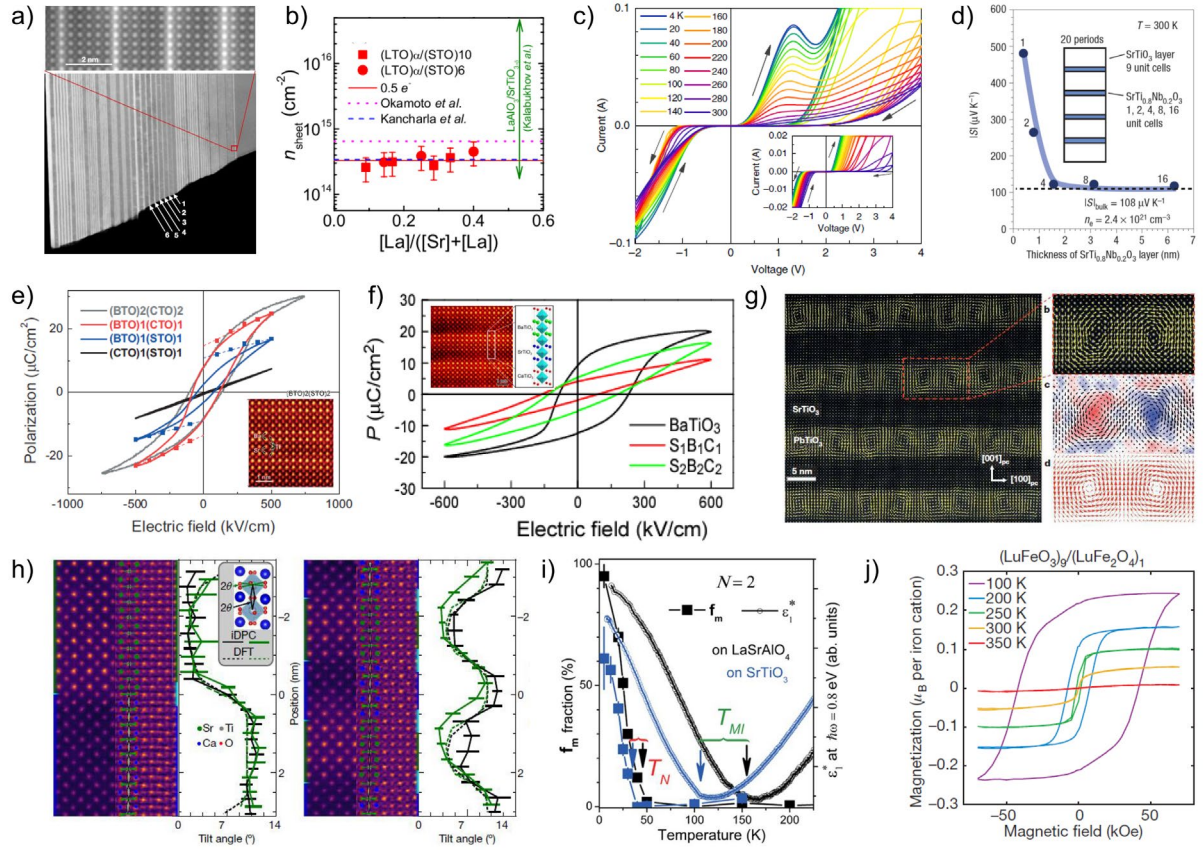


Figure 2. a) Cross-section scanning transmission electron microscopy image, reproduced with permission.^[16] Copyright 2002, Springer Nature, b) optical spectroscopy analysis, reproduced with permission.^[17] Copyright 2007, American Physical Society, and c) quantum resonant tunneling results of LaTiO₃/SrTiO₃ superlattices, reproduced with permission.^[21] Copyright 2015, Springer Nature. d) Thermopower in SrTiO₃/SrTi_{0.8}Nb_{0.2}O₃ superlattices with varying SrTi_{0.8}Nb_{0.2}O₃ thickness, reproduced with permission.^[24] Copyright 2007, Springer Nature. e) Polarization hysteresis of Ti-based superlattices, reproduced with permission.^[25] Copyright 2007, Wiley-VCH. f) Polarization hysteresis of Ti-based tri-color superlattices, reproduced with permission.^[10] Copyright 2005, Springer Nature. g) Observation on polar vortex in PbTiO₃/SrTiO₃ superlattices using electron microscopy.^[27] Copyright 2016, Springer Nature. h) Octahedral tilt angle of different thickness of SrTiO₃/CaTiO₃ superlattices from ADF and iDPC image, reproduced with permission.^[28, 29] Copyright 2022, Springer Nature. i) Temperature dependent muon ratio affected by local magnetic field and normalized permittivity in LaNiO₃/LaAlO₃ superlattices grown on LaSrAlO₄ and SrTiO₃ each, reproduced with permission.^[34] Copyright 2011, American Association for the Advancement of Science. j) Temperature dependent magnetic hysteresis of (LuFeO₃)₉/(LuFe₂O₄)₁ superlattices, reproduced with permission.^[35] Copyright 2016, Springer Nature.

Table 2. Summary of reported 4d SrRuO₃ based superlattices.^[41, 54, 55, 70, 86-164]

4d SrRuO ₃ based superlattices	Functionality of partner compounds	Reference
SrRuO ₃ /SrTiO ₃	Quantum paraelectric	[54, 55, 70, 86-110]
SrRuO ₃ /BaTiO ₃		[111, 112]
SrRuO ₃ /PbTiO ₃	Ferroelectric	[41, 114]
SrRuO ₃ /PbZr _{0.52} Ti _{0.48} O ₃		[113, 115]
SrRuO ₃ /LaAlO ₃	Dielectric	[116]
SrRuO ₃ /SrCuO ₂	Infinite layer	[117]
SrRuO ₃ /La _{0.7} Sr _{0.3} MnO ₃		[118-137, 143]
SrRuO ₃ /Pc _{0.7} Ca _{0.3} MnO ₃		[138-143]
SrRuO ₃ /La _{0.7} Ca _{0.3} MnO ₃		[144-146]
SrRuO ₃ /PrMnO ₃	(Anti-)Ferromagnetic	[147-149]
SrRuO ₃ /SrMnO ₃		[150-155]
SrRuO ₃ /LaCoO ₃		[156]
SrRuO ₃ /LaNiO ₃		[157]
SrRuO ₃ /BiFeO ₃	Multiferroic	[158-160]
SrRuO ₃ /SrIrO ₃		[161-163]
SrRuO ₃ /SrIrO ₃ /SrZrO ₃ SrRuO ₃ /SrHfO ₃ /SrZrO ₃	5d oxides	[164]

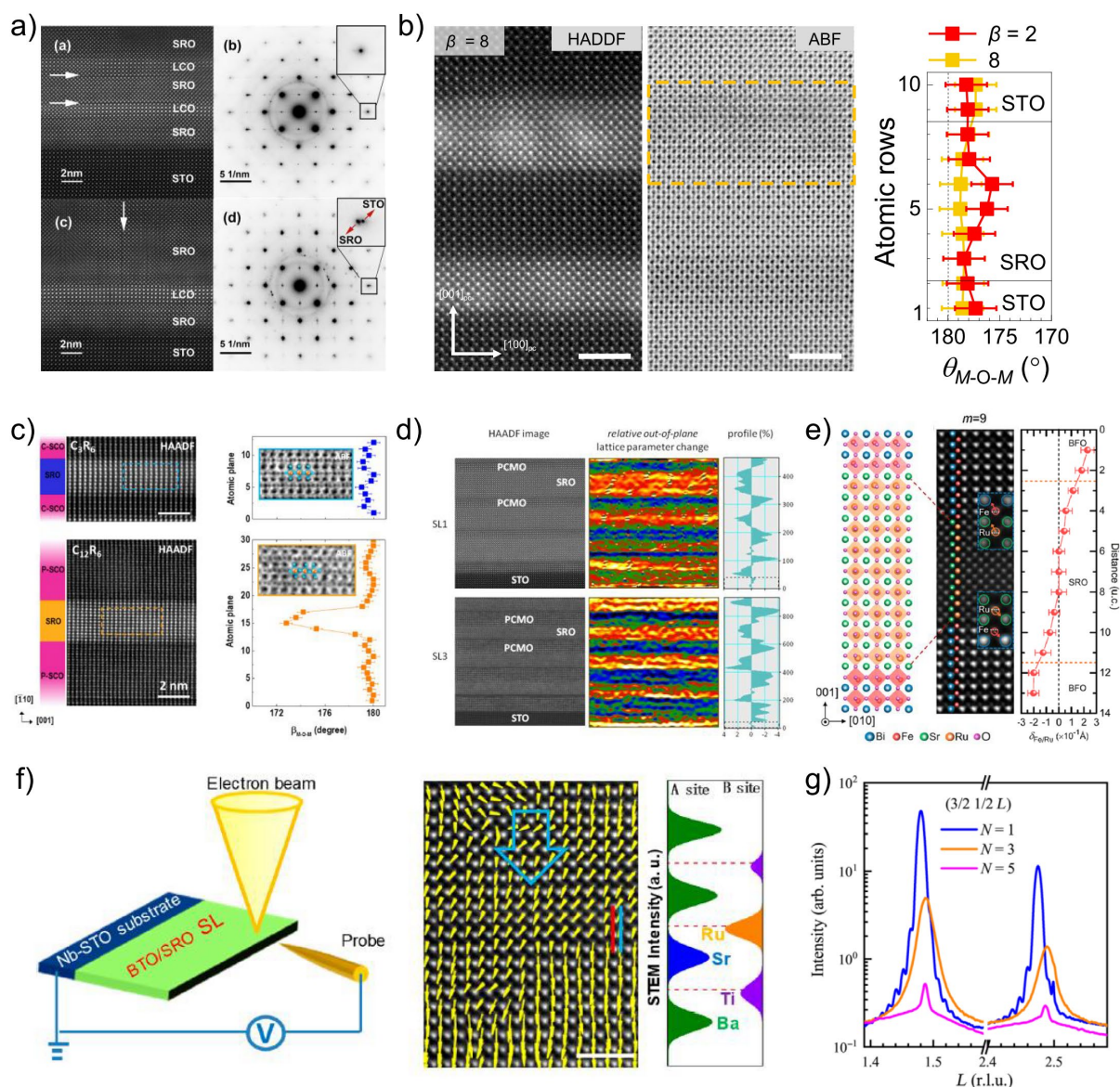


Figure 3. a) Cross-sectional scanning transmission electron microscopy and selected area electron diffraction images of SrRuO₃/LaCoO₃ multilayer thin films, reproduced with permission.^[156] Copyright 2018, Elsevier. b) Scanning transmission electron microscopy images for SrRuO₃/SrTiO₃ superlattices and propagation of octahedral distortion with respect to SrTiO₃ layer thickness, reproduced with permission.^[91] Copyright 2020, Wiley-VCH. c) Scanning transmission electron microscopy image and octahedral distortion of SrRuO₃/SrCuO₂ superlattices, reproduced with permission.^[117] Copyright 2021, American Chemical Society. d) Scanning transmission electron microscopy image and relative out-of-plane lattice parameter change of SrRuO₃/Pr_{0.7}Ca_{0.3}MnO₃ superlattices, reproduced with permission.^[141] Copyright 2011, IOP publishing. e) Ionic displacements of interfacial SrRuO₃ induced by ferroelectric polarization of BiFeO₃ in SrRuO₃/BiFeO₃ multilayer structure, reproduced with permission.^[158] Copyright 2022, American Chemical Society. f) In situ

transmission electron microscopy for electrical field control of Ru ion displacement through ferroelectric polarization in SrRuO₃/BaTiO₃ superlattices, reproduced with permission.^[112]

Copyright 2020, American Chemical Society. g) Observation on octahedral distortion of SrRuO₃/SrTiO₃ superlattice by half-order X-ray diffraction measurements, reproduced with permission.^[107] Copyright 2020, American Association for the Advancement of Science.

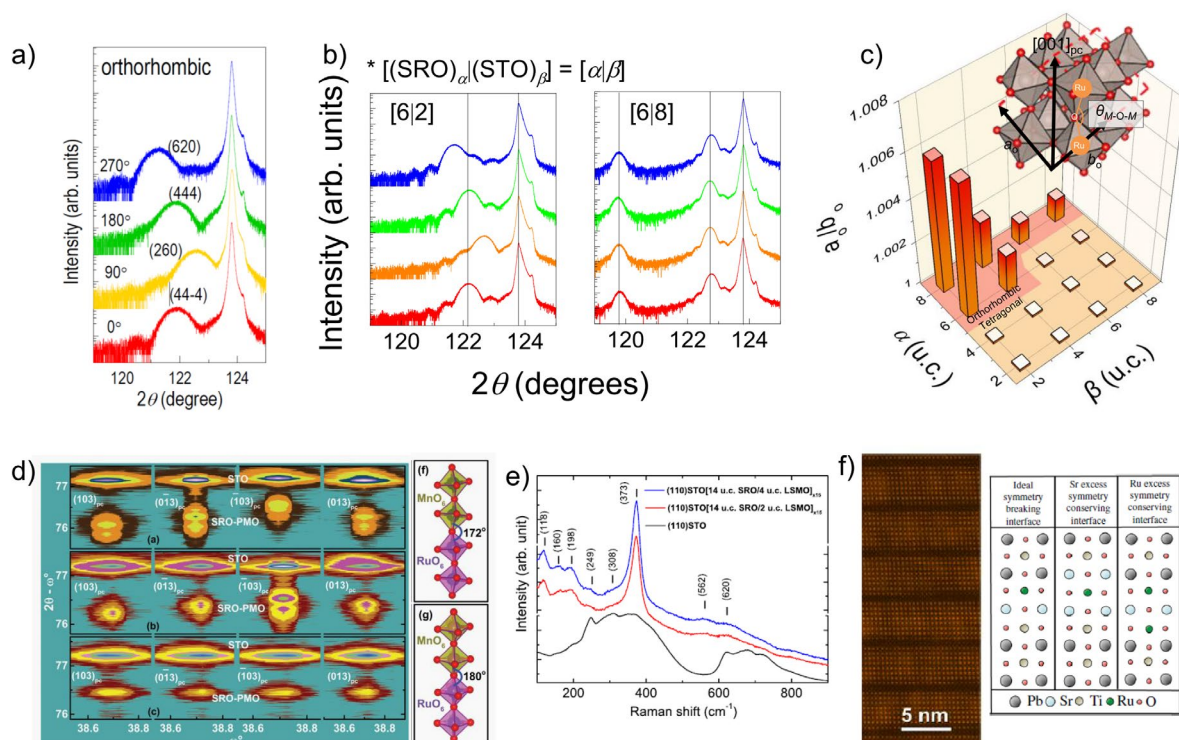


Figure 4. a) Asymmetric crystal structure of orthorhombic SrRuO₃ heterostructure observed by off-axis measurement around (204) SrTiO₃ Bragg reflections with four different azimuth angles, reproduced with permission.^[49] Copyright 2017, Springer Nature. b) Structural phase transition of SrRuO₃/SrTiO₃ superlattices from orthorhombic to tetragonal as SrTiO₃ layer thickness increases.^[91] Copyright 2020, Wiley-VCH. c) Octahedral distortion mapping of SrRuO₃/SrTiO₃ superlattices with respect to SrRuO₃ and SrTiO₃ layer thickness, reproduced with permission.^[91] Copyright 2020, Wiley-VCH. d) Structural phase transition of SrRuO₃/PrMnO₃ with respect to PrMnO₃ layer thickness shown by reciprocal space mapping around (103) SrTiO₃ Bragg reflections for four different azimuth angles, reproduced with permission.^[147] Copyright 2018, Wiley-VCH. e) Raman spectroscopy of (110) oriented SrTiO₃ and SrRuO₃/La_{0.7}Sr_{0.3}MnO₃ superlattice on (110) oriented SrTiO₃ with different La_{0.7}Sr_{0.3}MnO₃ thickness, reproduced with permission.^[129] Copyright 2014, AIP publishing. f) Scanning transmission electron microscopy image and the three types of theoretically possible

interfaces of an SrRuO₃/PbTiO₃ superlattice, reproduced with permission.^[41] Copyright 2012, American Physical Society.

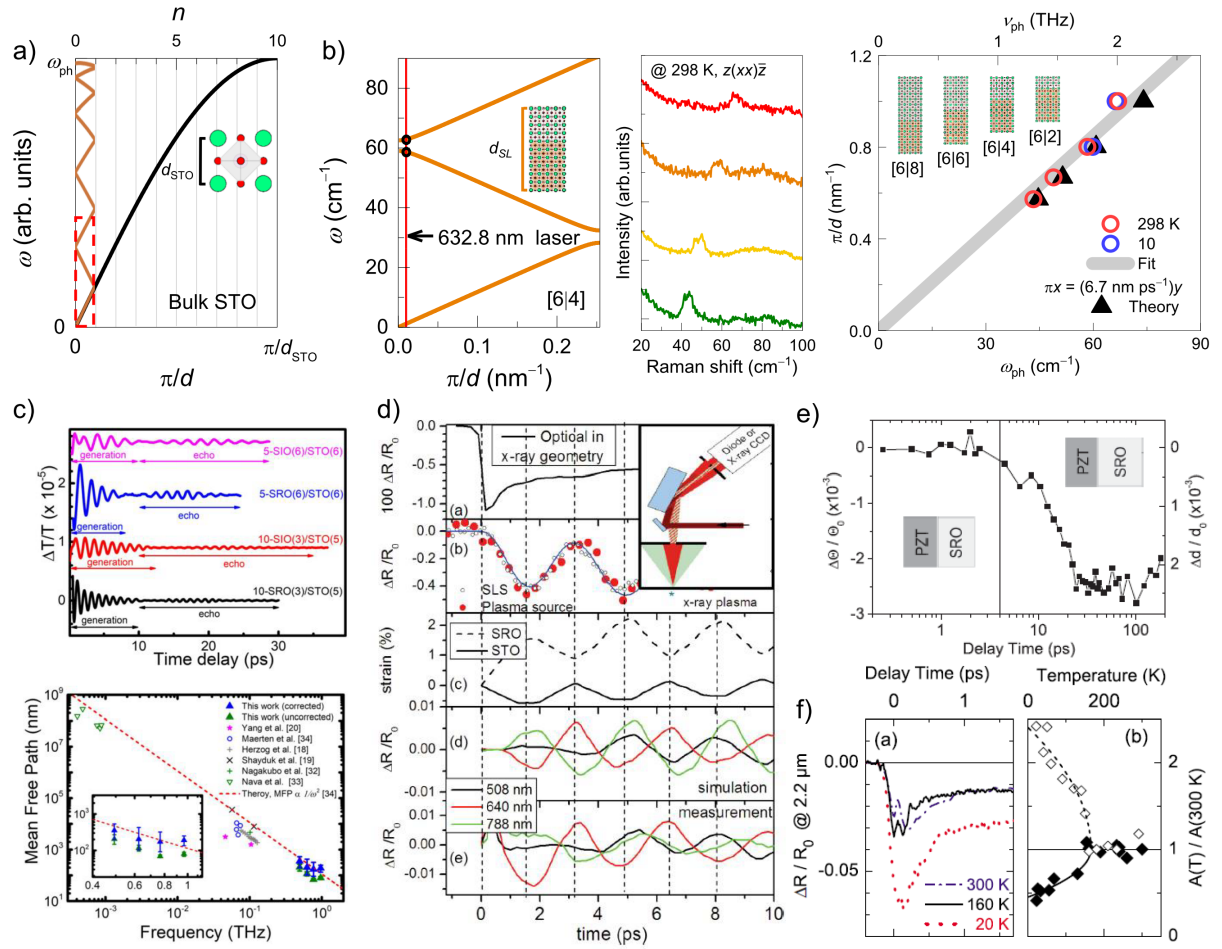


Figure 5. a) Schematic of zone-folded phonon dispersion of bulk SrTiO₃ and SrRuO₃/SrTiO₃ superlattice, reproduced with permission.^[88] Copyright 2022, Wiley-VCH. b) Theoretical estimation of zone-folded phonon dispersion of SrRuO₃/SrTiO₃ superlattice system and Raman spectra. reproduced with permission.^[88] Copyright 2022, Wiley-VCH. c) Time-resolved pump-probe of SrRuO₃(or SrIrO₃)/SrTiO₃ superlattice and frequency dependent phonon mean free path, reproduced with permission.^[103] Copyright 2020, IOP publishing. d) Comparison of zone-folded acoustic phonon in SrRuO₃/SrTiO₃ superlattice observed by optical pump-probe measurement and ultrafast X-ray diffraction, reproduced with permission.^[108] Copyright 2012, American Physical Society. e) relative angular shift of SrRuO₃/PbZr_{0.2}Ti_{0.8}O₃ of the selected Bragg reflection, reproduced with permission.^[113] Copyright 2007, American Physical Society. f) Optical reflectivity change for three different temperatures and comparison between temperature dependence of the amplitude of the

reflectivity change and superlattice phonon oscillation, reproduced with permission.^[95]

Copyright 2008, American Physical Society.

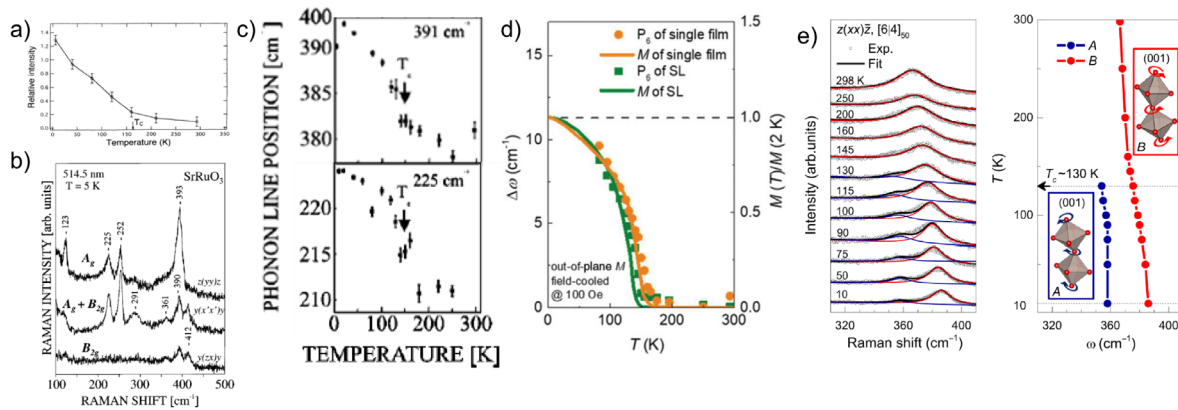


Figure 6. a) Temperature-dependent Raman spectra of SrRuO₃ thin film showing phonon anomalies at ferromagnetic transition temperature, reproduced with permission.^[173] Copyright 1995, American Physical Society. b) Polarized Raman spectra of ~300-nm-thickness SrRuO₃ thin film on (010) and (001) SrTiO₃ substrates, reproduced with permission.^[174] Copyright 1999, American Physical Society. c) Temperature dependence of the Raman peak position of (010)-oriented SrRuO₃ thin film, reproduced with permission.^[174] Copyright 1999, American Physical Society. d) Temperature dependence of both phonon anomaly and magnetization to compare spin-phonon coupling of single SrRuO₃ film and SrRuO₃/SrTiO₃ superlattice, reproduced with permission.^[70] Copyright 2020, The Royal Society of Chemistry. e) Phonon mode splitting corresponding to oxygen vibrations with orthogonal polarizations in bulk SrRuO₃ below ferromagnetic phase transition temperature, reproduced with permission.^[55] Copyright 2022, American Association for the Advancement of Science.

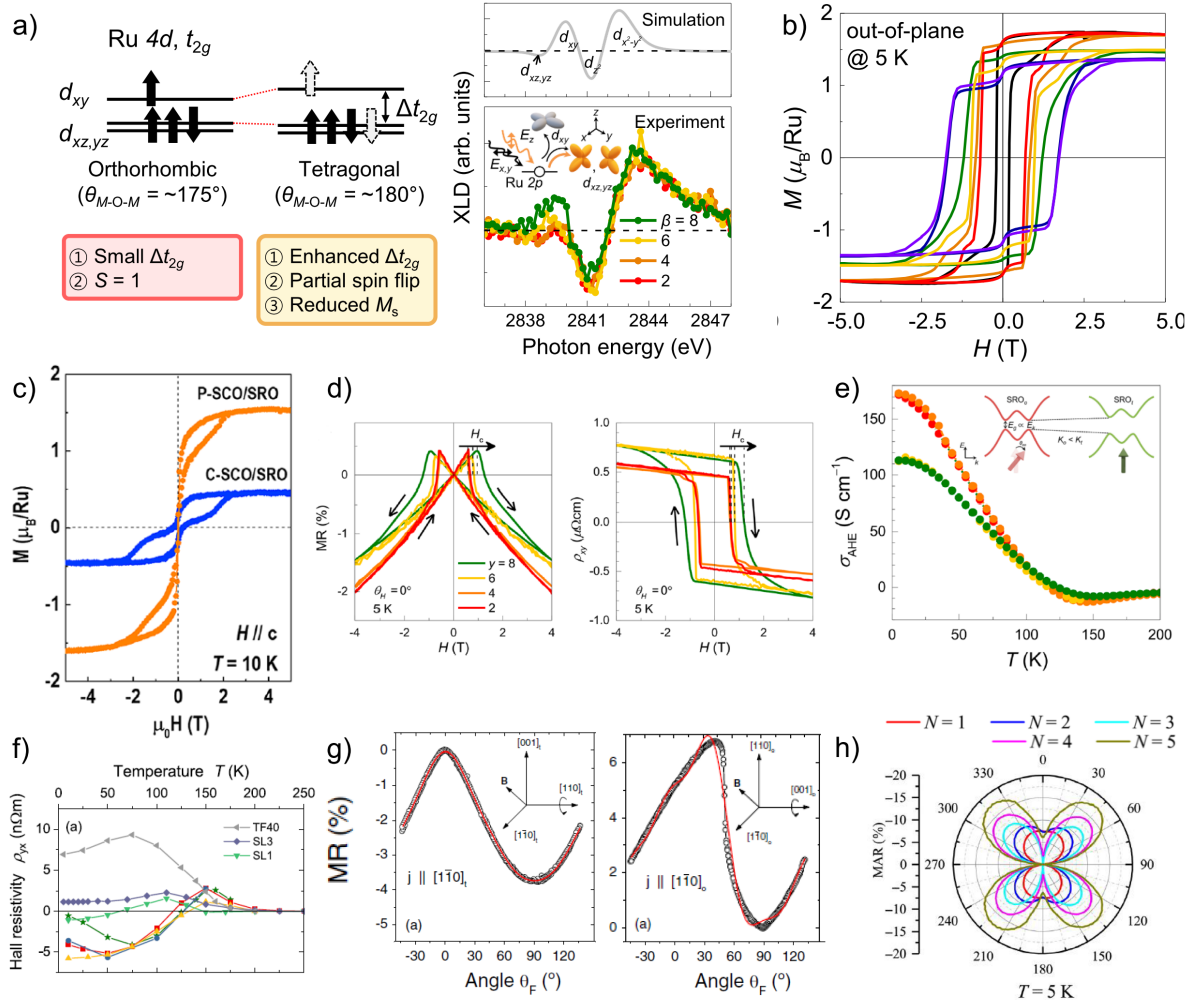


Figure 7. a) Orbital energy splitting difference between orthorhombic and tetragonal SrRuO₃, reproduced with permission.^[91] Copyright 2020, Wiley-VCH. b) Systematic change of saturation magnetization with structural phase transition of SrRuO₃/SrTiO₃ superlattice between orthorhombic and tetragonal, reproduced with permission.^[91] Copyright 2020, Wiley-VCH. c) Structural dependence of magnetic field-dependent magnetization of SrCuO₂/SrRuO₃/SrCuO₂ heterostructure with respect to the SrCuO₂ layer thickness, reproduced with permission.^[117] Copyright 2021, American Chemical Society. d) Magnetoresistance and anomalous Hall effect in SrRuO₃/SrTiO₃ superlattices, reproduced with permission.^[89] Copyright 2021, American Chemical Society. e) Temperature dependent anomalous Hall conductivity of SrRuO₃ in orthorhombic and tetragonal structure, reproduced with permission.^[89] Copyright 2021, American Chemical Society. f) Temperature dependent Hall resistivity of SrRuO₃/Pr_{0.7}Ca_{0.3}MnO₃ superlattice, reproduced with permission.^[141] Copyright 2011, IOP publishing. g) Magnetic field angle dependent magnetoresistance measurement of orthorhombic and tetragonal SrRuO₃/Pr_{0.7}Ca_{0.3}MnO₃ superlattices, reproduced with permission.^[138] Copyright 2019, IOP publishing. h) Magnetic field angle

dependent magnetoresistance of SrRuO₃/SrTiO₃ superlattices with different SrTiO₃ thickness, reproduced with permission.^[107] Copyright 2020, American Association for the Advancement of Science.

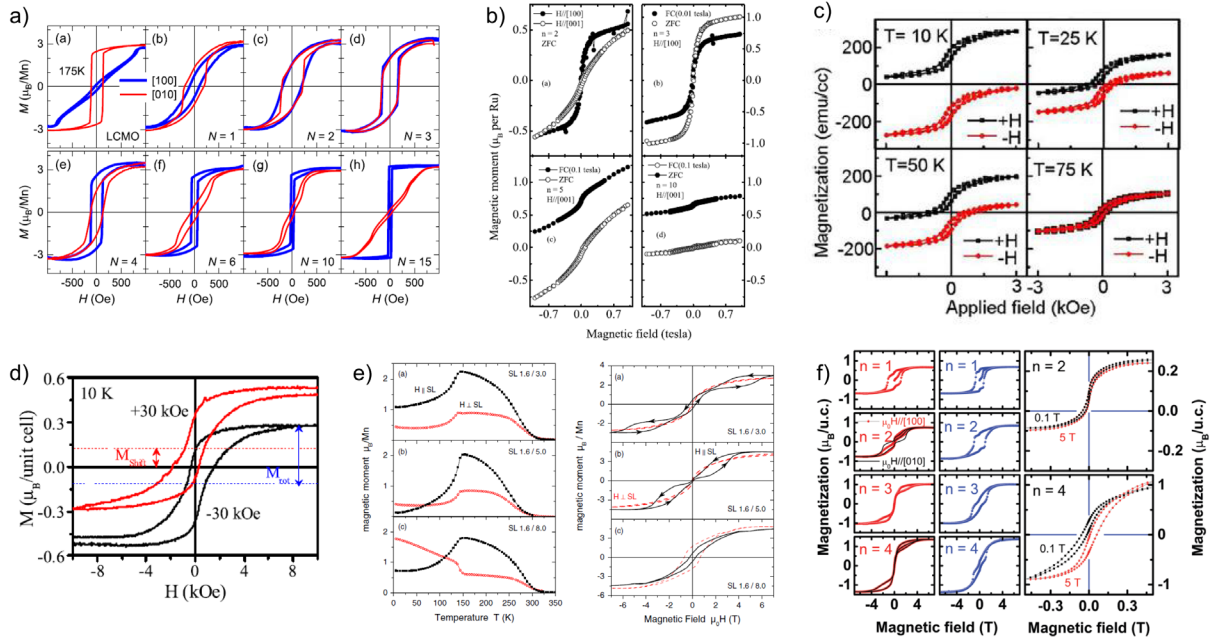


Figure 8. a) Repetition number dependent lateral magnetic anisotropy of SrRuO₃/La_{0.67}Ca_{0.33}MnO₃ superlattices, reproduced with permission.^[145] Copyright 2021, AIP publishing. b) Magnetic hysteresis loop showing dependence in field direction and difference between field-cooled and zero-field-cooled hysteresis of SrRuO₃/SrMnO₃ superlattices, reproduced with permission.^[151] Copyright 2005, Springer Nature. c) Temperature dependence of exchange bias effect in SrRuO₃/LaNiO₃ superlattices, reproduced with permission.^[157] Copyright 2020, Taylor & Francis. d) Exchange bias effect in SrRuO₃/BiFeO₃ superlattices, reproduced with permission.^[159] Copyright 2019, Elsevier. e) Left panel, temperature dependence of out-of-plane (circles) and in-plane (squares) magnetic moment measured by field cooled method. Right panel, SrRuO₃ thickness-dependent magnetic moment in SrRuO₃/La_{0.7}Sr_{0.3}MnO₃ superlattice, reproduced with permission.^[136] Copyright 2010, American Physical Society. f) In-plane, out-of-plane, and field-cooled in-plane magnetic hysteresis loop of SrRuO₃/PrMnO₃ superlattice as a function of PrMnO₃ thickness, reproduced with permission.^[147] Copyright 2018, Wiley-VCH.

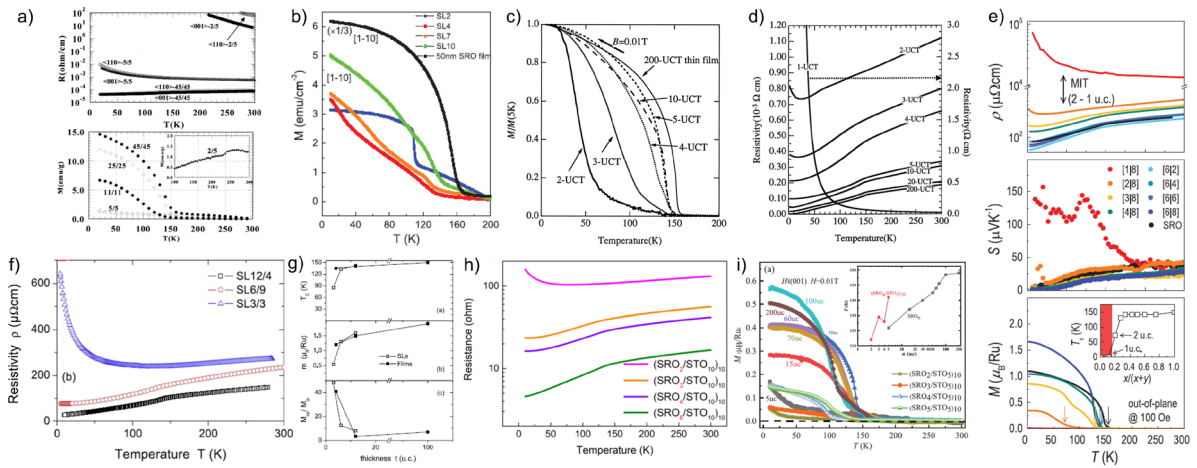


Figure 9. a) Temperature dependent transport and magnetization with respect to stacking periodicity in of SrRuO₃/BaTiO₃ superlattice grown on SrTiO₃ (110) substrates, reproduced with permission.^[111] Copyright 2000, Elsevier. b) Temperature dependent magnetization of SrRuO₃/LaAlO₃ superlattices with varying SrRuO₃ layer thickness, reproduced with permission.^[116] Copyright 2012, AIP publishing. c) Temperature dependent magnetization of SrRuO₃/SrTiO₃ superlattices with varying SrRuO₃ thickness, reproduced with permission.^[86, 87] Copyright 1998, Elsevier. d) Temperature dependent transport of SrRuO₃/SrTiO₃ superlattices with different SrRuO₃ thickness, reproduced with permission.^[86, 87] Copyright 1998, The Physical Society of Japan e) Dimensional crossover effect of SrRuO₃/SrTiO₃ superlattice as a function of SrRuO₃ thickness, reproduced with permission^[92] Copyright 2020, American Physical Society. f) Temperature dependent resistivity and g) summarized magnetic properties of three different SrRuO₃/SrTiO₃ superlattices, reproduced with permission.^[100] Copyright 2013, IOP publishing. h) Temperature dependent resistance of SrRuO₃/SrTiO₃ superlattices with varying SrRuO₃ layer thickness, reproduced with permission.^[98] Copyright 2020, American Physical Society. i) Temperature dependent magnetization SrRuO₃/SrTiO₃ superlattices as a function of SrRuO₃ thickness, reproduced with permission.^[54] Copyright 2022, Wiley-VCH.

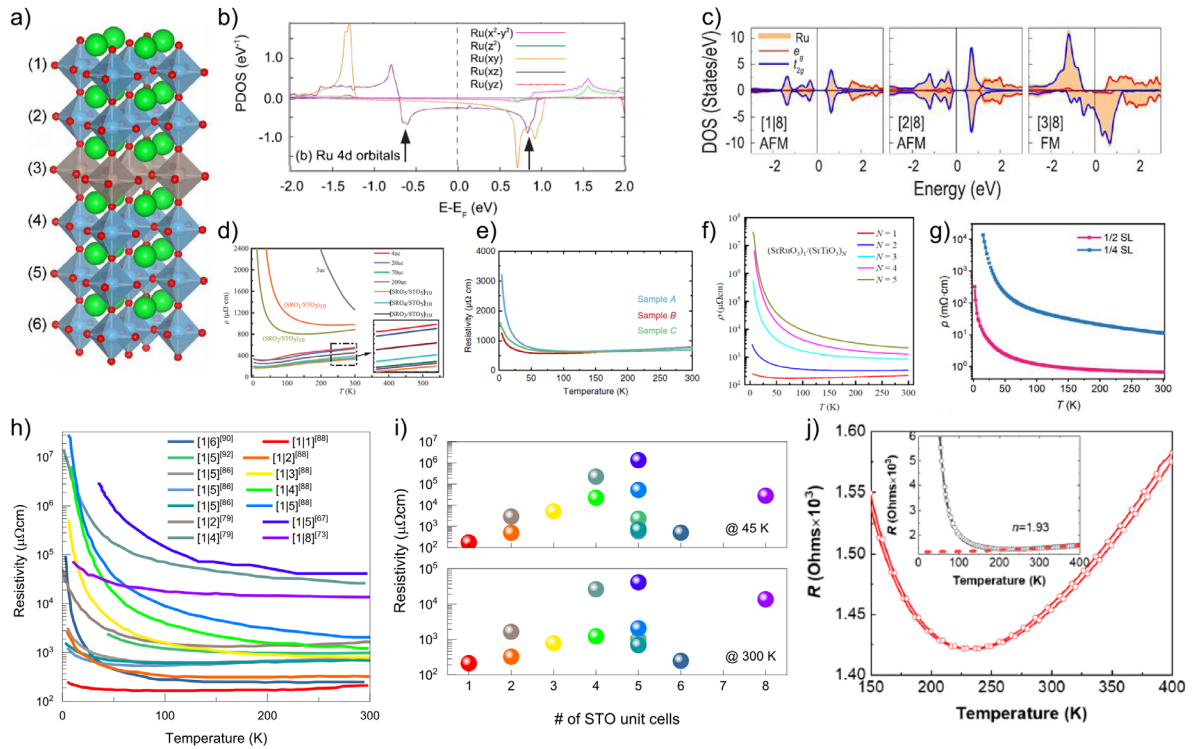


Figure 10. a) Schematic and b) projected density of states of Ru orbitals of oxide superlattice composed monolayer SrRuO₃ layer and 5 unit cell layers of SrTiO₃, reproduced with permission.^[102] Copyright 2012, American Physical Society. c) Dimensionality-induced phase transition of SrRuO₃/SrTiO₃ superlattice as a function of the thickness of the SrRuO₃ layer, reproduced with permission.^[92] Copyright 2020, American Physical Society. d) Temperature dependent transport with varying SrRuO₃ layer thickness in SrRuO₃/SrTiO₃ superlattice, reproduced with permission.^[178] Copyright 2020, Wiley-VCH. e) Temperature dependent transport of three different monolayer SrRuO₃ superlattices with the same periodicity, reproduced with permission.^[105] Copyright 2019, American Physical Society. f) Temperature dependent resistivity of SrRuO₃/SrTiO₃ superlattice with varying SrTiO₃ thickness, reproduced with permission.^[107] Copyright 2020, American Association for the Advancement of Science. g) Temperature dependent transport of SrRuO₃/SrTiO₃ superlattice with two different SrTiO₃ thickness, reproduced with permission.^[99] Copyright 2022, Springer Nature. h) Summary of the temperature dependent resistivity of SrRuO₃ monolayer within SrRuO₃/SrTiO₃ superlattices.^[54, 86, 92, 99, 105, 107, 109] i) SrTiO₃ thickness dependent resistivity of monolayer SrRuO₃ superlattice at 45 K and 300 K. j) Temperature dependent transport of monolayer SrRuO₃ superlattice with 10 unit cell layers of BaTiO₃, reproduced with permission.^[112] Copyright 2021, American Chemical Society.

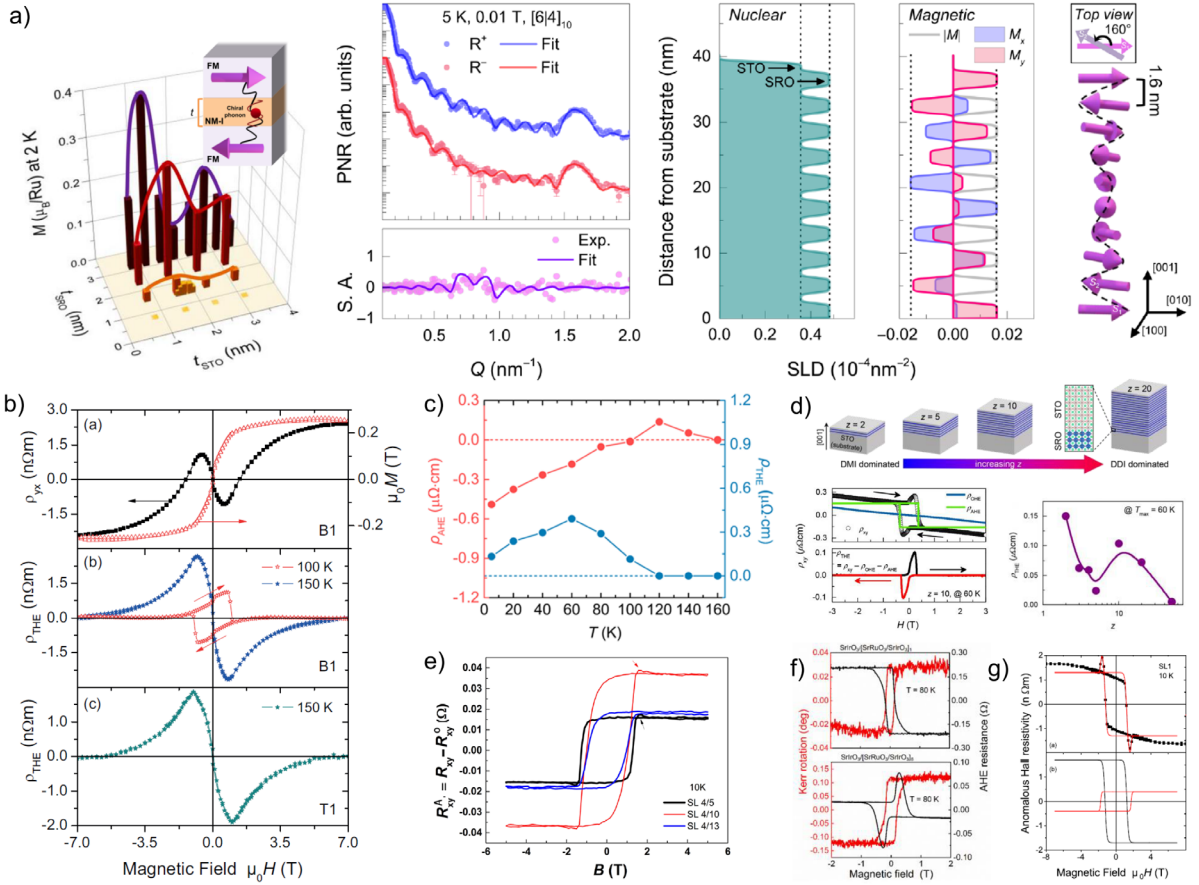


Figure 11. a) In-plane magnetization in SrRuO₃/SrTiO₃ superlattices at 2 K as a function of SrRuO₃ and SrTiO₃ layer thickness. The middle and right panels are polarized neutron reflectivity result with fitting analysis and corresponding spin structure of SrRuO₃/SrTiO₃ superlattices, respectively, reproduced with permission.^[55] Copyright 2022, American Association for the Advancement of Science. b) Interlayer coupling induced topological Hall effect in SrRuO₃/La_{0.7}Sr_{0.3}MnO₃ superlattice, reproduced with permission.^[122] Copyright 2017, Wiley-VCH. c) Temperature dependent anomalous and topological Hall effect in SrRuO₃/BiFeO₃ multilayer, reproduced with permission.^[158] Copyright 2022, American Chemical Society. d) Repetition number dependence of topological Hall effect in SrRuO₃/SrTiO₃ superlattice, reproduced with permission.^[90] Copyright 2021, Elsevier. e) Topological Hall signal of SrRuO₃/SrIrO₃ superlattice, reproduced with permission.^[163] Copyright 2021, American Chemical Society. f) Kerr rotation and anomalous Hall effect with hump structure formed as SrIrO₃/SrRuO₃/SrIrO₃ trilayers changed to SrRuO₃/SrIrO₃ superlattice, reproduced with permission.^[162] Copyright 2021, American Physical Society. g) Anomalous Hall resistivity with hump signal in SrRuO₃/Pr_{0.7}Ca_{0.3}MnO₃ superlattice, reproduced with permission.^[138] Copyright 2019, IOP publishing.

Table 3. Summary of reported *5d* SrIrO₃ based superlattices.^[75, 199-218]

5d SrIrO₃ based superlattices	Functionality of partner compounds	Reference
SrIrO ₃ /SrTiO ₃	Quantum paraelectric	[75, 199-205]
SrIrO ₃ /CaTiO ₃	Incipient ferroelectric	[206]
SrIrO ₃ /La _{1-x} Sr _x MnO ₃		[207-211]
SrIrO ₃ /SrMnO ₃		[212]
SrIrO ₃ /LaCoO ₃		[213, 214]
SrIrO ₃ /LaFeO ₃	(Anti-)Ferromagnetic	[215]
SrIrO ₃ /LaMnO ₃		[216]
SrIrO ₃ /LaNiO ₃		[217]
SrIrO ₃ /CaMnO ₃		[218]

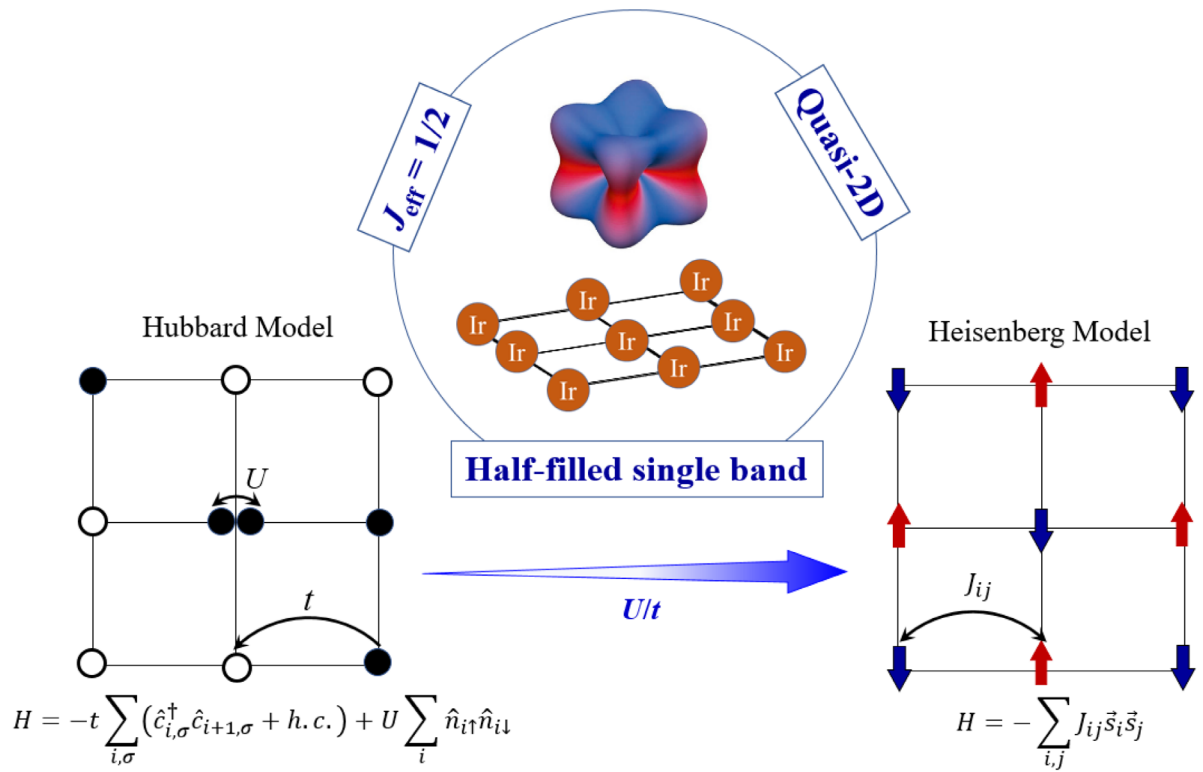


Figure 12. Physics relevant to the 2D square-lattice iridate, ranging from the charge Hubbard model to the spin Heisenberg model.

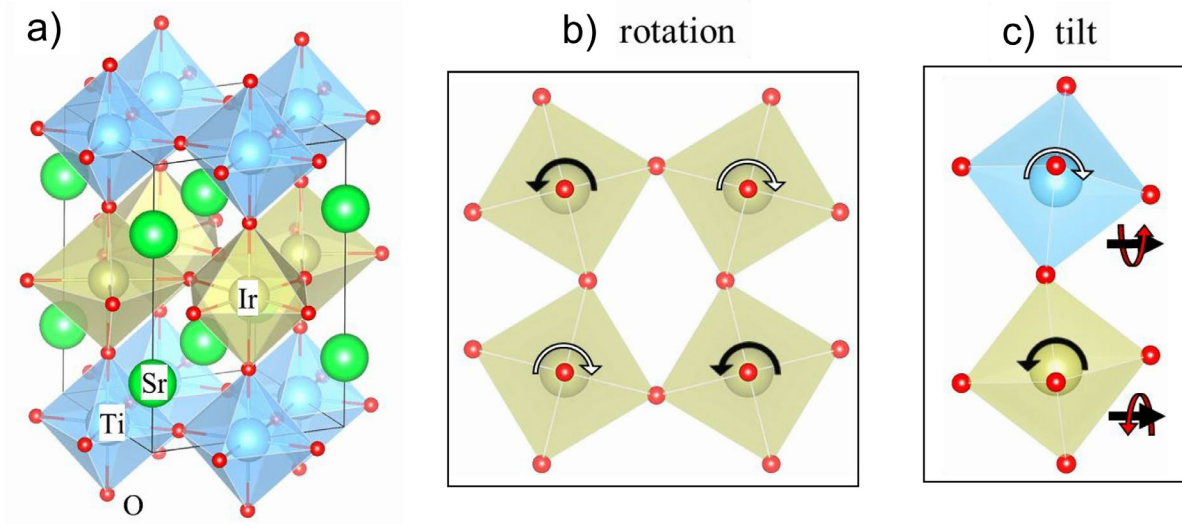


Figure 13. a) Lattice structure of (SrIrO₃)₁/(SrTiO₃)₁. Schematics of b) octahedral rotation and c) tilt.

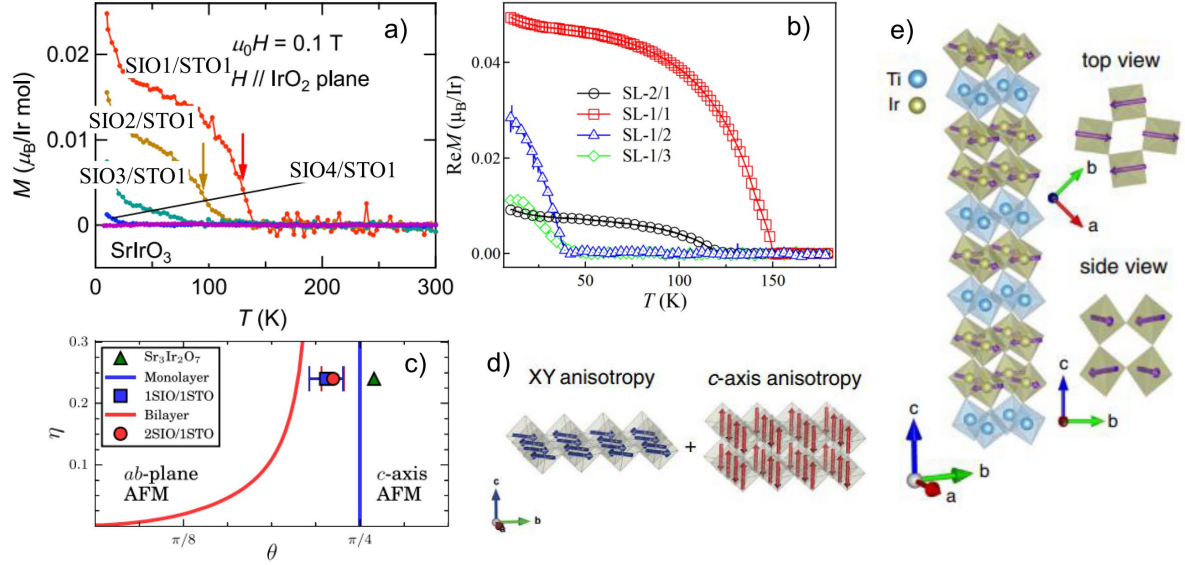


Figure 14. a) Temperature dependent magnetization of $(\text{SrIrO}_3)_m/(\text{SrTiO}_3)_1$, reproduced with permission.^[75] Copyright 2015, American Physical Society. b) Temperature dependent magnetization of $(\text{SrIrO}_3)_1/(\text{SrTiO}_3)_m$, reproduced with permission.^[199] Copyright 2017, American Physical Society. c) Classic magnetic phase diagram of monolayer- and bilayer-iridates. (here, η is the ratio of Hund's coupling on Coulomb repulsion and θ denotes tetragonal distortion of IrO_6 octahedron), reproduced with permission.^[203] Copyright 2019, Springer Nature. d) Schematic of the addition of an easy-plane monolayer iridate and easy-axis bilayer iridate. e) Magnetic structure of a hybrid $(\text{SrIrO}_3)_1/(\text{SrTiO}_3)_1/(\text{SrIrO}_3)_2/(\text{SrTiO}_3)_1$ superlattice, reproduced with permission.^[204] Copyright 2022, American Physical Society.

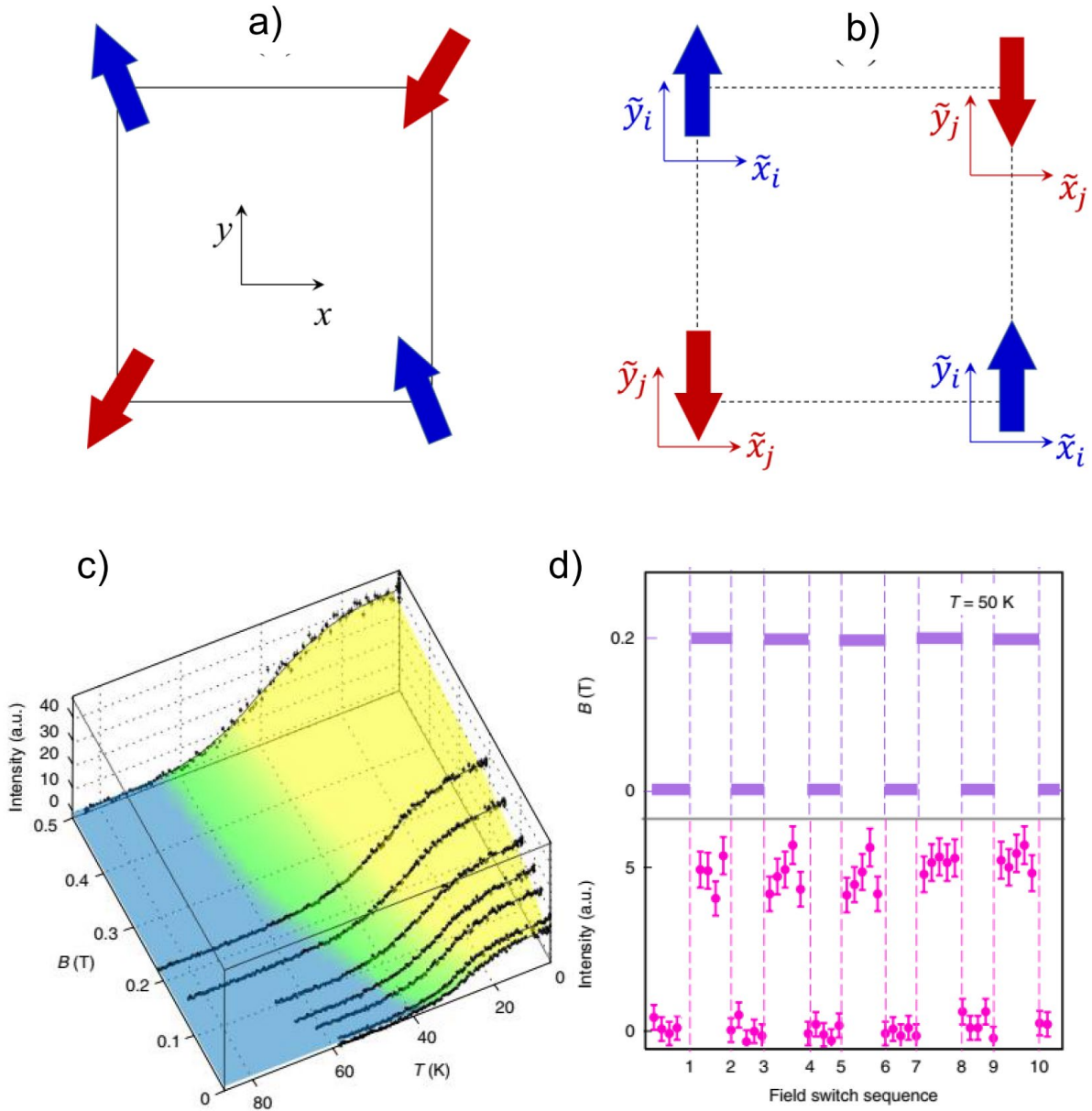


Figure 15. Schematics of canted antiferromagnetic structure in a) the global frame and b) a staggered local frame. c) Temperature dependent magnetic peak intensity of $(\text{SrIrO}_3)_1/(\text{SrTiO}_3)_2$ under various magnetic fields, reproduced with permission. Copyright 2018, Springer Nature. d) Switching sequence of a 0.2 T magnetic field and the associated change in the magnetic peak intensity of $(\text{SrIrO}_3)_1/(\text{SrTiO}_3)_2$, reproduced with permission.^[205] Copyright 2018, Springer Nature.

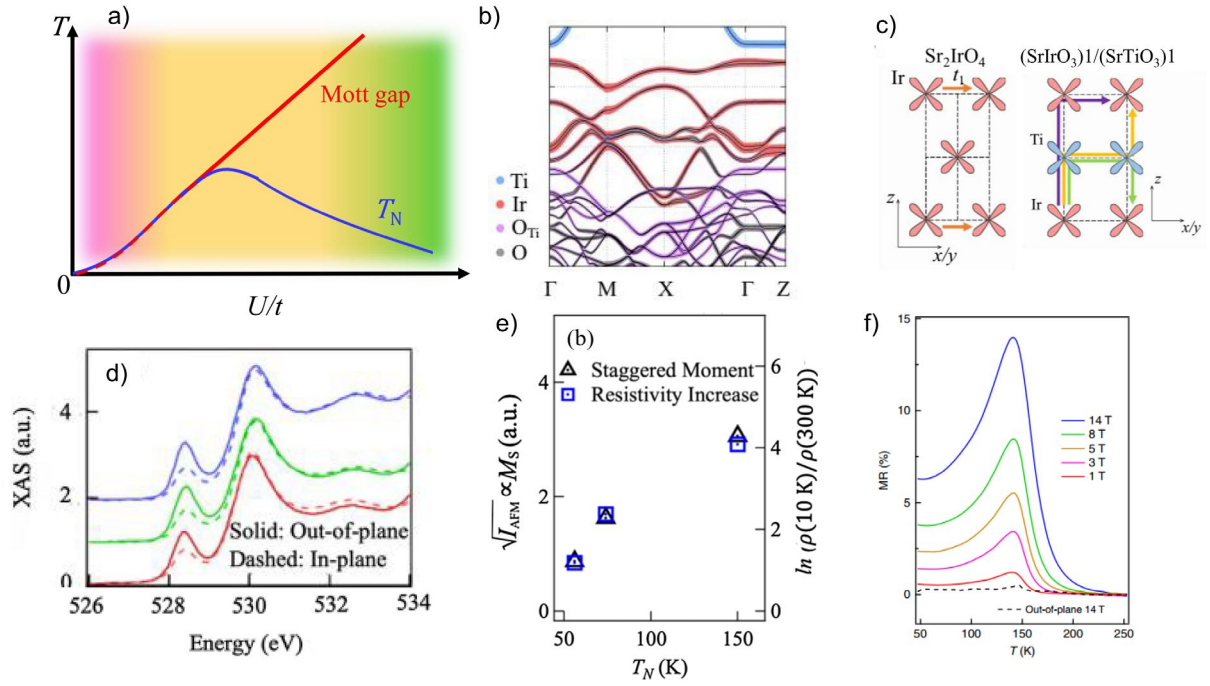


Figure 16. a) A generic phase diagram of the half-filled single-band Hubbard system as a function of U/t . b) Representative band structure of $(\text{SrIrO}_3)_1/(\text{SrTiO}_3)_1$, reproduced with permission.^[202] Copyright 2016, American Physical Society. c) Orbital arrangements of Ir and Ti orbitals for Sr_2IrO_4 and $(\text{SrIrO}_3)_1/(\text{SrTiO}_3)_1$, reproduced with permission.^[202] Copyright 2016, American Physical Society. d) Polarization-dependent X-ray absorption spectra of $(\text{SrIrO}_3)_1/(\text{SrTiO}_3)_1$ grown on SrTiO_3 (red), LSAT (green), and NdGaO_3 (blue) substrates, reproduced with permission.^[248] Copyright 2020, American Physical Society. e) Staggered moment and resistivity increase of $(\text{SrIrO}_3)_1/(\text{SrTiO}_3)_1$ as a function of Neel temperature, reproduced with permission.^[248] Copyright 2020, American Physical Society. f) Magnetoresistance dependence on temperature under various magnetic fields, reproduced with permission.^[253] Copyright 2019, Springer Nature.

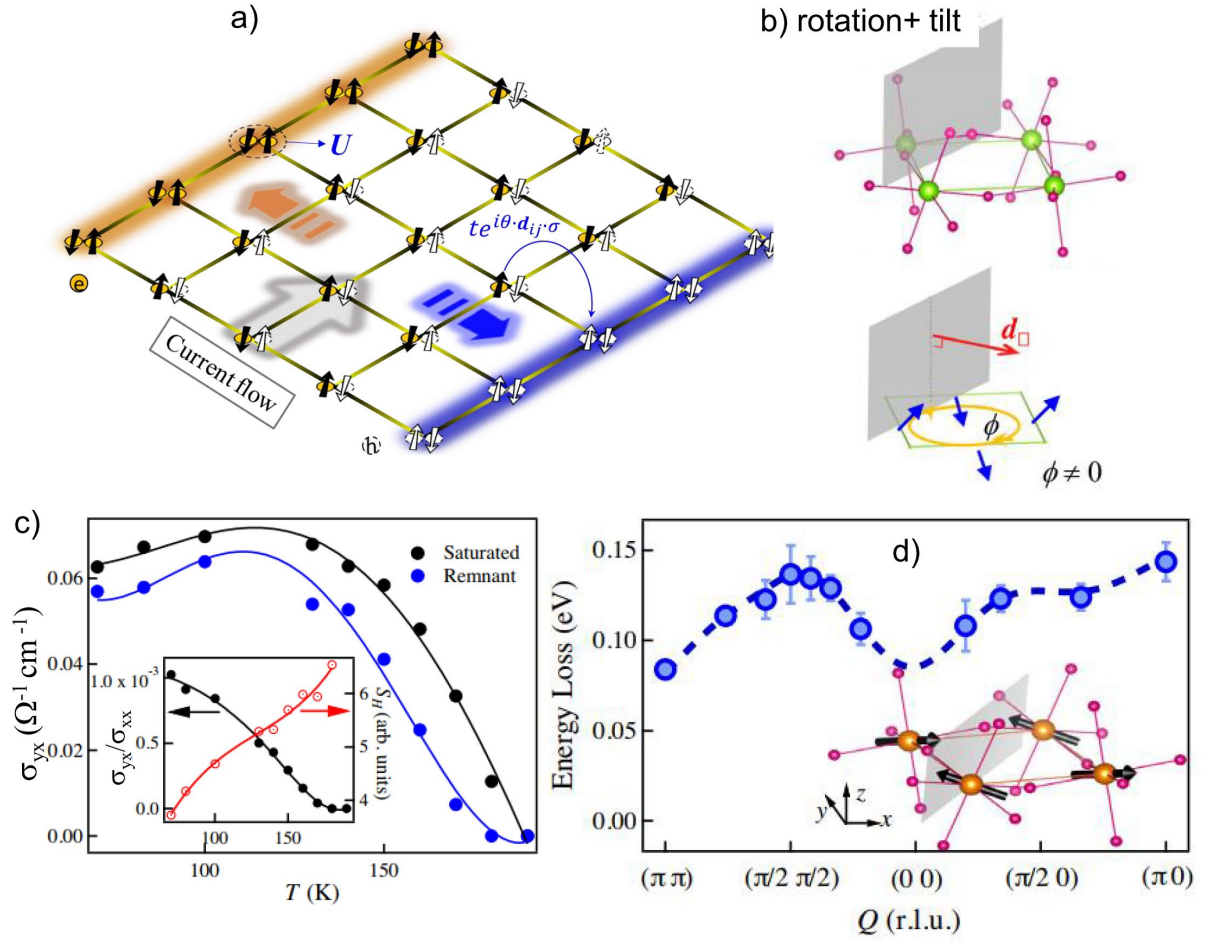


Figure 17. a) Schematic of a distorted 2D Hubbard system with a SU(2) gauge field modulating the electron hopping process. b) Square lattice with a finite octahedral rotation and tilt. The bottom panel displays the orientation of the Dzyaloshinskii–Moriya vectors. c) Temperature dependent anomalous Hall conductivity of $(\text{SrIrO}_3)_1/(\text{CaTiO}_3)_1$. The inset displays the temperature dependencies of the anomalous Hall angle (left) and anomalous Hall coefficient (right). d) Magnon dispersion of $(\text{SrIrO}_3)_1/(\text{CaTiO}_3)_1$ at base temperature. The inset displays the ground-state magnetic structure of the superlattice, reproduced with permission.^[206] Copyright 2022, American Physical Society.

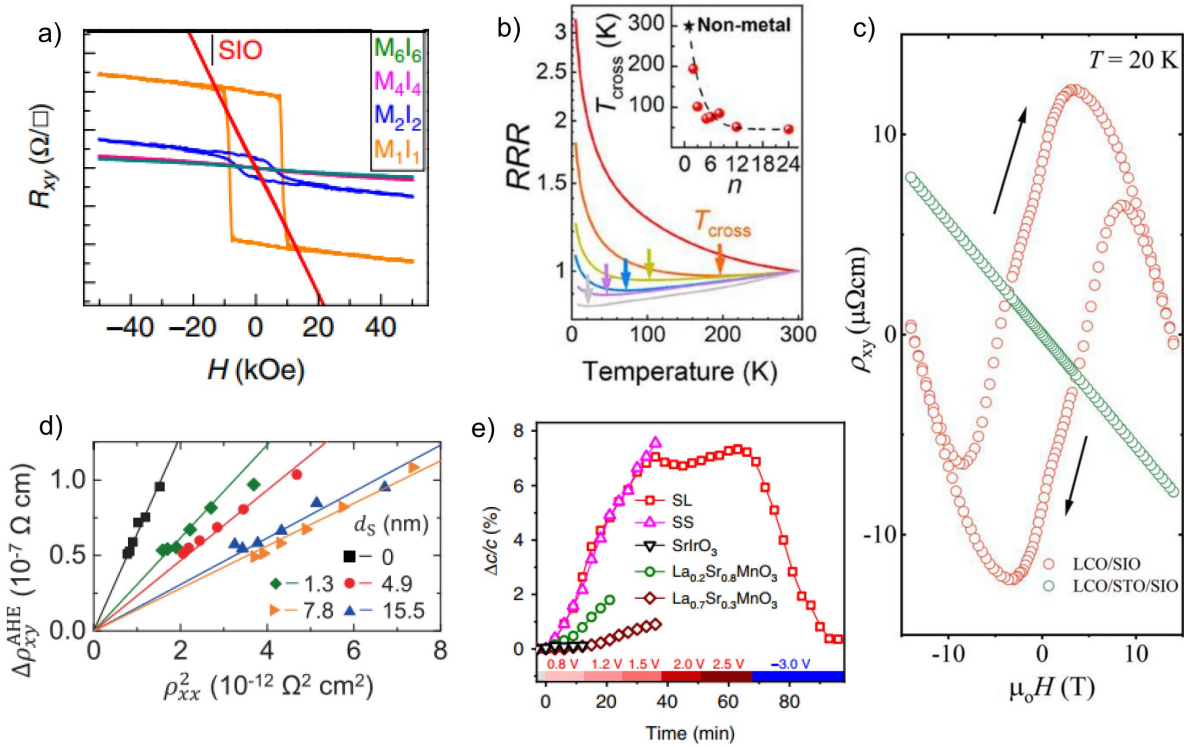


Figure 18. a) Anomalous Hall resistivity as a function of c -axis magnetic field of a series of $(\text{SrIrO}_3)_y/(\text{SrMnO}_3)_x$ (M_xI_y in the notation) superlattices, reproduced with permission.^[212] Copyright 2016, Springer Nature. b) Temperature dependent resistivity of $\text{SrIrO}_3/\text{CaMnO}_3$, reproduced with permission.^[218] Copyright 2022, American Chemical Society. c) Field dependent anomalous Hall resistivity of $\text{SrIrO}_3/\text{LaCoO}_3$ and $\text{SrIrO}_3/\text{SrTiO}_3/\text{LaCoO}_3$ heterostructures, reproduced with permission.^[213] Copyright 2022, Wiley-VCH. d) Relation between anomalous Hall resistivity and the square of longitudinal resistivity of $\text{SrIrO}_3/\text{La}_{0.7}\text{Sr}_{0.3}\text{MnO}_3$ heterostructures, reproduced with permission.^[207] Copyright 2021, Springer Nature. e) Time evolution of the lattice structure of $\text{SrIrO}_3/\text{La}_{0.8}\text{Sr}_{0.2}\text{MnO}_3$ superlattice under ionic liquid gating, reproduced with permission.^[211] Copyright 2022, Springer Nature.

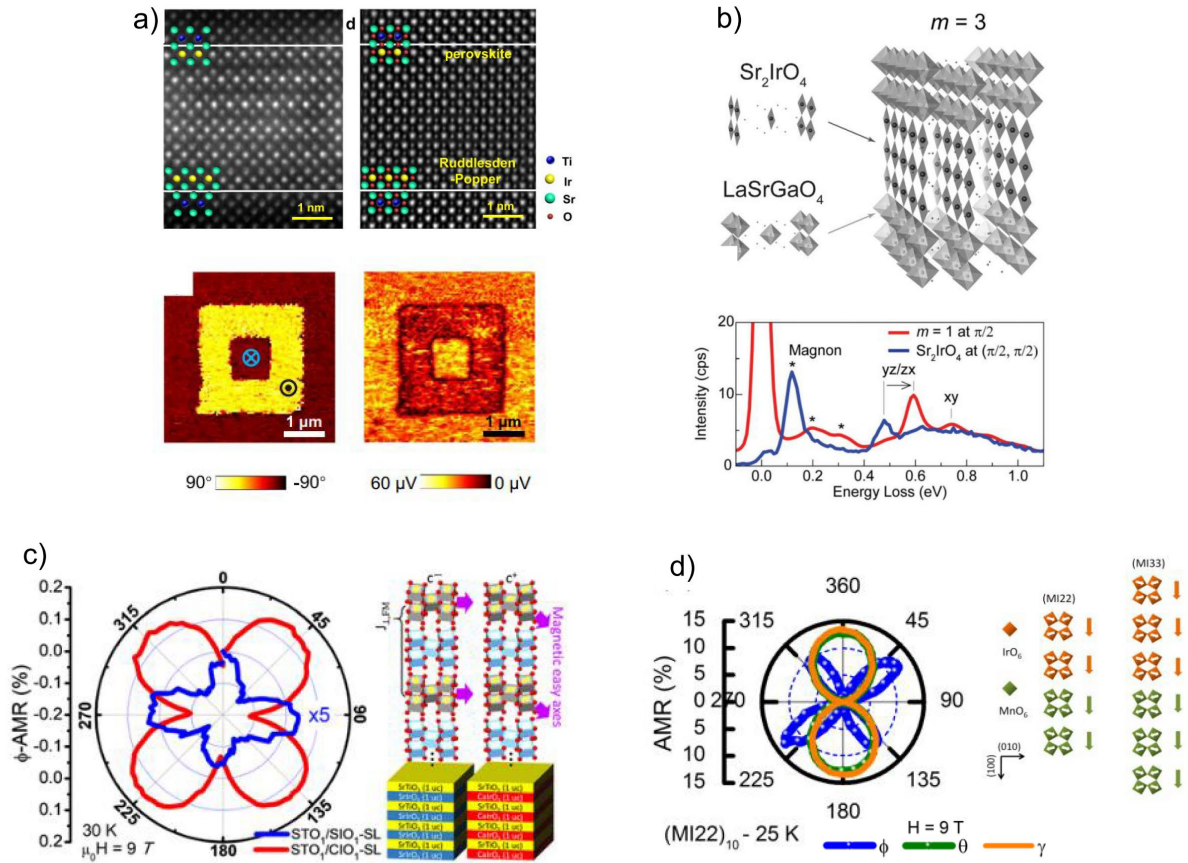


Figure 19. a) Atomically resolved High angle annular dark-field and integrated differential phase contrast images of $(\text{Sr}_2\text{IrO}_4)_3/(\text{SrTiO}_3)_6$ superlattice. The bottom panel shows the out-of-plane PFM images of the superlattice at 3.7 K, reproduced with permission.^[268] Copyright 2021, Springer Nature. b) Schematic diagram of the a -axis-oriented $(\text{Sr}_2\text{IrO}_4)_3/(\text{LaSrGaO}_4)_5$ superlattice. The bottom panel displays resonant inelastic X-ray scattering spectra of the superlattice and Sr_2IrO_4 , reproduced with permission.^[269] Copyright 2016, Wiley-VCH. c) Anisotropic magnetoresistance effect and schematic of $(\text{CaIrO}_3)_1/(\text{SrTiO}_3)_1$, reproduced with permission.^[272] Copyright 2020, American Chemical Society. d) Anisotropic magnetoresistance effect and magnetic structure of $\text{CaIrO}_3/\text{CaMnO}_3$, reproduced with permission.^[273] Copyright 2022, American Physical Society.

Acknowledgements

This work was supported by the Basic Science Research Programs through the National Research Foundation of Korea (NRF-2021R1A2C2011340 and 2022R1C1C2006723). Lin Hao acknowledges financial support from the Collaborative Innovation Program of Hefei Science Center, CAS (2022HSC-CIP005), and the HFIPS Director's Fund (2023YZGH01).

References

- [1] C. H. Ahn, K. M. Rabe, J. M. Triscone, *Science* **2004**, 303, 488.
- [2] J. Chakhalian, J. W. Freeland, A. J. Millis, C. Panagopoulos, J. M. Rondinelli, *Rev. Mod. Phys.* **2014**, 86, 1189.
- [3] H. Y. Hwang, Y. Iwasa, M. Kawasaki, B. Keimer, N. Nagaosa, Y. Tokura, *Nat. Mater.* **2012**, 11, 103.
- [4] R. Ramesh, D. G. Schlom, *Nat. Rev. Mater.* **2019**, 4, 257.
- [5] Y. Tokura, N. Nagaosa, *Science* **2000**, 288, 462.
- [6] P. Yu, Y.-H. Chu, R. Ramesh, *Materials Today* **2012**, 15, 320.
- [7] P. Zubko, S. Gariglio, M. Gabay, P. Ghosez, J.-M. Triscone, *Annu. Rev. Condens. Matter Phys.* **2011**, 2, 141.
- [8] Y. Tokura, M. Kawasaki, N. Nagaosa, *Nat. Phys.* **2017**, 13, 1056.
- [9] J. Heber, *Nature* **2009**, 459, 28.
- [10] H. N. Lee, H. M. Christen, M. F. Chisholm, C. M. Rouleau, D. H. Lowndes, *Nature* **2005**, 433, 395.
- [11] A. K. Geim, I. V. Grigorieva, *Nature* **2013**, 499, 419.
- [12] K. T. Kang, J. Park, D. Suh, W. S. Choi, *Adv. Mater.* **2019**, 31, 1803732.
- [13] Z. Huang, Ariando, X. Renshaw Wang, A. Rusydi, J. Chen, H. Yang, T. Venkatesan, *Adv. Mater.* **2018**, 30, 1802439.
- [14] T. Takayama, J. Chaloupka, A. Smerald, G. Khaliullin, H. Takagi, *J. Phys. Soc. Jpn.* **2021**, 90, 062001.
- [15] A. Ohtomo, H. Y. Hwang, *Nature* **2004**, 427, 423.
- [16] A. Ohtomo, D. A. Muller, J. L. Grazul, H. Y. Hwang, *Nature* **2002**, 419, 378.
- [17] S. S. A. Seo, W. S. Choi, H. N. Lee, L. Yu, K. W. Kim, C. Bernhard, T. W. Noh, *Phys. Rev. Lett.* **2007**, 99, 266801.
- [18] V. R. Cooper, S. S. A. Seo, S. Lee, J. S. Kim, W. S. Choi, S. Okamoto, H. N. Lee, *Sci. Rep.* **2014**, 4, 6021.
- [19] W. S. Choi, S. Lee, V. R. Cooper, H. N. Lee, *Nano Letters* **2012**, 12, 4590.
- [20] W. S. Choi, H. Ohta, H. N. Lee, *Adv. Mater.* **2014**, 26, 6701.
- [21] W. S. Choi, S. A. Lee, J. H. You, S. Lee, H. N. Lee, *Nat. Commun.* **2015**, 6, 7424.
- [22] S. S. A. Seo, M. J. Han, G. W. J. Hassink, W. S. Choi, S. J. Moon, J. S. Kim, T. Susaki, Y. S. Lee, J. Yu, C. Bernhard, H. Y. Hwang, G. Rijnders, D. H. A. Blank, B. Keimer, T. W. Noh, *Phys. Rev. Lett.* **2010**, 104, 036401.
- [23] W. S. Choi, H. Ohta, S. J. Moon, Y. S. Lee, T. W. Noh, *Phys. Rev. B* **2010**, 82, 024301.
- [24] H. Ohta, S. Kim, Y. Mune, T. Mizoguchi, K. Nomura, S. Ohta, T. Nomura, Y. Nakanishi, Y. Ikuhara, M. Hirano, H. Hosono, K. Koumoto, *Nat. Mater.* **2007**, 6, 129.
- [25] S. S. A. Seo, J. H. Lee, H. N. Lee, M. F. Chisholm, W. S. Choi, D. J. Kim, J. Y. Jo, H. Kim, J. Yu, T. W. Noh, *Adv. Mater.* **2007**, 19, 2460.
- [26] Y. L. Tang, Y. L. Zhu, X. L. Ma, A. Y. Borisevich, A. N. Morozovska, E. A. Eliseev, W. Y. Wang, Y. J. Wang, Y. B. Xu, Z. D. Zhang, S. J. Pennycook, *Science* **2015**, 348, 547.
- [27] A. K. Yadav, C. T. Nelson, S. L. Hsu, Z. Hong, J. D. Clarkson, C. M. Schlepütz, A. R. Damodaran, P. Shafer, E. Arenholz, L. R. Dedon, D. Chen, A. Vishwanath, A. M. Minor,

- L. Q. Chen, J. F. Scott, L. W. Martin, R. Ramesh, *Nature* **2016**, 530, 198.
- [28] E. R. Hoglund, D.-L. Bao, A. O'Hara, S. Makarem, Z. T. Piontkowski, J. R. Matson, A. K. Yadav, R. C. Haislmaier, R. Engel-Herbert, J. F. Ihlefeld, J. Ravichandran, R. Ramesh, J. D. Caldwell, T. E. Beechem, J. A. Tomko, J. A. Hachtel, S. T. Pantelides, P. E. Hopkins, J. M. Howe, *Nature* **2022**, 601, 556.
- [29] J. Ravichandran, A. K. Yadav, R. Cheaito, P. B. Rossen, A. Soukiassian, S. J. Suresha, J. C. Duda, B. M. Foley, C.-H. Lee, Y. Zhu, A. W. Lichtenberger, J. E. Moore, D. A. Muller, D. G. Schlom, P. E. Hopkins, A. Majumdar, R. Ramesh, M. A. Zurbuchen, *Nat. Mater.* **2014**, 13, 168.
- [30] D. W. Jeong, W. S. Choi, T. D. Kang, C. H. Sohn, A. David, H. Rotella, A. A. Sirenko, C. H. Lee, J. H. Kim, U. Lüders, W. Prellier, Y. J. Kim, Y. S. Lee, T. W. Noh, *Phys. Rev. B* **2011**, 84, 115132.
- [31] W. S. Choi, D. W. Jeong, S. S. A. Seo, Y. S. Lee, T. H. Kim, S. Y. Jang, H. N. Lee, K. Myung-Whun, *Phys. Rev. B* **2011**, 83, 195113.
- [32] S. H. Chang, S. K. Kim, Y.-M. Kim, Y. Dong, C. M. Folkman, D. W. Jeong, W. S. Choi, A. Y. Borisevich, J. A. Eastman, A. Bhattacharya, D. D. Fong, *APL Mater.* **2019**, 7, 071117.
- [33] D. W. Jeong, W. S. Choi, S. Okamoto, J. Y. Kim, K. W. Kim, S. J. Moon, D. Y. Cho, H. N. Lee, T. W. Noh, *Sci. Rep.* **2014**, 4, 6124.
- [34] A. V. Boris, Y. Matiks, E. Benckiser, A. Frano, P. Popovich, V. Hinkov, P. Wochner, M. Castro-Colin, E. Detemple, V. K. Malik, C. Bernhard, T. Prokscha, A. Suter, Z. Salman, E. Morenzoni, G. Cristiani, H. U. Habermeier, B. Keimer, *Science* **2011**, 332, 937.
- [35] J. A. Mundy, C. M. Brooks, M. E. Holtz, J. A. Moyer, H. Das, A. F. Rébola, J. T. Heron, J. D. Clarkson, S. M. Disseler, Z. Liu, A. Farhan, R. Held, R. Hovden, E. Padgett, Q. Mao, H. Paik, R. Misra, L. F. Kourkoutis, E. Arenholz, A. Scholl, J. A. Borchers, W. D. Ratcliff, R. Ramesh, C. J. Fennie, P. Schiffer, D. A. Muller, D. G. Schlom, *Nature* **2016**, 537, 523.
- [36] W. R. Grove, *Philos. Trans. R. Soc. Lond.* **1852**, 142, 87.
- [37] J. E. Greene, *Journal of Vacuum Science & Technology A* **2017**, 35, 05C204.
- [38] M. Dawber, in *Epitaxial Growth of Complex Metal Oxides (Second Edition)*, DOI: <https://doi.org/10.1016/B978-0-08-102945-9.00016-2> (Eds: G. Koster, M. Huijben, G. Rijnders), Woodhead Publishing **2015**, p. 37.
- [39] J. M. Triscone, O. Fischer, O. Brunner, L. Antognazza, A. D. Kent, M. G. Karkut, *Phys. Rev. Lett.* **1990**, 64, 804.
- [40] M. Dawber, N. Stucki, C. Lichtensteiger, S. Gariglio, P. Ghosez, J.-M. Triscone, *Adv. Mater.* **2007**, 19, 4153.
- [41] S. J. Callori, J. Gabel, D. Su, J. Sinsheimer, M. V. Fernandez-Serra, M. Dawber, *Phys. Rev. Lett.* **2012**, 109, 067601.
- [42] C. Domínguez, A. B. Georgescu, B. Mundet, Y. Zhang, J. Fowlie, A. Mercy, A. Waelchli, S. Catalano, D. T. L. Alexander, P. Ghosez, A. Georges, A. J. Millis, M. Gibert, J.-M. Triscone, *Nat. Mater.* **2020**, 19, 1182.
- [43] B. Mundet, C. Domínguez, J. Fowlie, M. Gibert, J.-M. Triscone, D. T. L. Alexander, *Nano Letters* **2021**, 21, 2436.
- [44] M. Gibert, P. Zubko, R. Scherwitzl, J. Íñiguez, J.-M. Triscone, *Nat. Mater.* **2012**, 11, 195.
- [45] H. M. Smith, A. F. Turner, *Appl. Opt.* **1965**, 4, 147.
- [46] J. R. A. Jr., *J. Appl. Phys.* **1968**, 39, 4032.
- [47] H. M. Christen, G. Eres, *J. Phys. Condens. Matter* **2008**, 20, 264005.
- [48] A. Ojeda-G-P, M. Döbeli, T. Lippert, *Adv. Mater. Interfaces* **2018**, 5, 1701062.
- [49] S. A. Lee, S. Oh, J. Lee, J.-Y. Hwang, J. Kim, S. Park, J.-S. Bae, T. E. Hong, S. Lee, S. W. Kim, W. N. Kang, W. S. Choi, *Sci. Rep.* **2017**, 7, 11583.

- [50] S. Woo, H. Choi, S. Kang, J. Lee, A. David, W. Prellier, Y. Kim, H. Y. Kim, W. S. Choi, *Applied Surface Science* **2020**, 499, 143924.
- [51] B. Kim, S. A. Lee, D. Seol, W. S. Choi, Y. Kim, *Curr. Appl. Phys.* **2017**, 17, 1721.
- [52] E. K. Ko, J. Mun, H. G. Lee, J. Kim, J. Song, S. H. Chang, T. H. Kim, S. B. Chung, M. Kim, L. Wang, T. W. Noh, *Adv. Funct. Mater.* **2020**, 30, 2001486.
- [53] J. Thompson, J. Nichols, S. Lee, S. Ryee, J. H. Gruenewald, J. G. Connell, M. Souiri, J. Johnson, J. Hwang, M. J. Han, *Appl. Phys. Lett.* **2016**, 109, 161902.
- [54] Z. Deng, J. Liu, Y. Hong, L. Wei, S. Hu, W. Xiao, L. Li, L. Wang, K. Chen, Z. Liao, *Adv. Mater. Interfaces* **2022**, 9, 2201371.
- [55] S. G. Jeong, J. Kim, A. Seo, S. Park, H. Y. Jeong, Y.-M. Kim, V. Lauter, T. Egami, J. H. Han, W. S. Choi, *Sci. Adv.* **2022**, 8, eabm4005.
- [56] W. Nunn, T. K. Truttman, B. Jalan, *J. Mater. Res.* **2021**, 36, 4846.
- [57] W. Nunn, A. K. Manjeshwar, J. Yue, A. Rajapitamahuni, T. K. Truttman, B. Jalan, *Proc. Natl. Acad. Sci. U. S. A.* **2021**, 118, e2105713118.
- [58] G. Koster, L. Klein, W. Siemons, G. Rijnders, J. S. Dodge, C.-B. Eom, D. H. A. Blank, M. R. Beasley, *Rev. Mod. Phys.* **2012**, 84, 253.
- [59] I. I. Mazin, D. J. Singh, *Phys. Rev. B* **1997**, 56, 2556.
- [60] M. Cuoco, A. Di Bernardo, *APL Mater.* **2022**, 10, 090902.
- [61] C. W. Jones, P. D. Battle, P. Lightfoot, W. T. A. Harrison, *Acta Crystallogr. C* **1989**, 45, 365.
- [62] P. A. Cox, R. G. Egdell, J. B. Goodenough, A. Hamnett, C. C. Naish, *J. Solid State Phys.* **1983**, 16, 6221.
- [63] P. B. Allen, H. Berger, O. Chauvet, L. Forro, T. Jarlborg, A. Junod, B. Revaz, G. Santi, *Phys. Rev. B* **1996**, 53, 4393.
- [64] S. A. Lee, S. Oh, J.-Y. Hwang, M. Choi, C. Youn, J. W. Kim, S. H. Chang, S. Woo, J.-S. Bae, S. Park, Y.-M. Kim, S. Lee, T. Choi, S. W. Kim, W. S. Choi, *Energy Environ. Sci.* **2017**, 10, 924.
- [65] C. B. Eom, R. J. Cava, R. M. Fleming, J. M. Phillips, R. B. vanDover, J. H. Marshall, J. W. P. Hsu, J. J. Krajewski, W. F. Peck, *Science* **1992**, 258, 1766.
- [66] A. Rastogi, M. Brahlek, J. M. Ok, Z. Liao, C. Sohn, S. Feldman, H. N. Lee, *APL Mater.* **2019**, 7, 091106.
- [67] H. Jeong, S. G. Jeong, A. Y. Mohamed, M. Lee, W.-s. Noh, Y. Kim, J.-S. Bae, W. S. Choi, D.-Y. Cho, *Appl. Phys. Lett.* **2019**, 115, 092906.
- [68] S. H. Chang, Y. J. Chang, S. Y. Jang, D. W. Jeong, C. U. Jung, Y. J. Kim, J. S. Chung, T. W. Noh, *Phys. Rev. B* **2011**, 84, 104101.
- [69] D. Kan, Y. Shimakawa, *Cryst. Growth Des.* **2011**, 11, 5483.
- [70] S. G. Jeong, S. Y. Lim, J. Kim, S. Park, H. Cheong, W. S. Choi, *Nanoscale* **2020**, 12, 13926.
- [71] D. W. Jeong, H. C. Choi, C. H. Kim, S. H. Chang, C. H. Sohn, H. J. Park, T. D. Kang, D.-Y. Cho, S. H. Baek, C. B. Eom, J. H. Shim, J. Yu, K. W. Kim, S. J. Moon, T. W. Noh, *Phys. Rev. Lett.* **2013**, 110, 247202.
- [72] S. Hahn, B. Sohn, M. Kim, J. R. Kim, S. Huh, Y. Kim, W. Kyung, M. Kim, D. Kim, Y. Kim, T. W. Noh, J. H. Shim, C. Kim, *Phys. Rev. Lett.* **2021**, 127, 256401.
- [73] D. Kan, R. Aso, R. Sato, M. Haruta, H. Kurata, Y. Shimakawa, *Nat. Mater.* **2016**, 15, 432.
- [74] J. Matsuno, N. Ogawa, K. Yasuda, F. Kagawa, W. Koshibae, N. Nagaosa, Y. Tokura, M. Kawasaki, *Sci. Adv.* **2016**, 2, e1600304.
- [75] J. Matsuno, K. Ihara, S. Yamamura, H. Wadati, K. Ishii, V. V. Shankar, H. Y. Kee, H. Takagi, *Phys. Rev. Lett.* **2015**, 114, 247209.
- [76] L. Wang, Q. Feng, Y. Kim, R. Kim, K. H. Lee, S. D. Pollard, Y. J. Shin, H. Zhou, W. Peng, D. Lee, W. Meng, H. Yang, J. H. Han, M. Kim, Q. Lu, T. W. Noh, *Nat. Mater.*

- 2018**, 17, 1087.
- [77] B. Sohn, B. Kim, S. Y. Park, H. Y. Choi, J. Y. Moon, T. Choi, Y. J. Choi, H. Zhou, J. W. Choi, A. Bombardi, D. G. Porter, S. H. Chang, J. H. Han, C. Kim, *Phys. Rev. Res.* **2021**, 3, 023232.
- [78] B. Sohn, E. Lee, S. Y. Park, W. Kyung, J. Hwang, J. D. Denlinger, M. Kim, D. Kim, B. Kim, H. Ryu, S. Huh, J. S. Oh, J. K. Jung, D. Oh, Y. Kim, M. Han, T. W. Noh, B.-J. Yang, C. Kim, *Nat. Mater.* **2021**, 20, 1643.
- [79] W. Lin, L. Liu, Q. Liu, L. Li, X. Shu, C. Li, Q. Xie, P. Jiang, X. Zheng, R. Guo, Z. Lim, S. Zeng, G. Zhou, H. Wang, J. Zhou, P. Yang, Ariando, S. J. Pennycook, X. Xu, Z. Zhong, Z. Wang, J. Chen, *Adv. Mater.* **2021**, 33, 2101316.
- [80] Z. Fang, N. Nagaosa, K. S. Takahashi, A. Asamitsu, R. Mathieu, T. Ogasawara, H. Yamada, M. Kawasaki, Y. Tokura, K. Terakura, *Science* **2003**, 302, 92.
- [81] S. Itoh, Y. Endoh, T. Yokoo, S. Ibuka, J.-G. Park, Y. Kaneko, K. S. Takahashi, Y. Tokura, N. Nagaosa, *Nat. Commun.* **2016**, 7, 11788.
- [82] K. Jenni, S. Kunkemöller, D. Brüning, T. Lorenz, Y. Sidis, A. Schneidewind, A. A. Nugroho, A. Rosch, D. I. Khomskii, M. Braden, *Phys. Rev. Lett.* **2019**, 123, 017202.
- [83] Z. Wang, H. P. Nair, G. C. Correa, J. Jeong, K. Lee, E. S. Kim, A. S. H., C. S. Lee, H. J. Lim, D. A. Muller, D. G. Schlom, *APL Mater.* **2018**, 6, 086101.
- [84] D. Popescu, B. Popescu, G. Jegert, S. Schmelzer, U. Boettger, P. Lugli, *IEEE Transactions on Electron Devices* **2014**, 61, 2130.
- [85] H. M. Kim, J. H. Lee, A. Yom, H. S. Lee, D. G. Kim, D. W. Ko, H. S. Kim, J.-H. Ahn, *J. Alloys Compd.* **2021**, 857, 157627.
- [86] M. Izumi, K. Nakazawa, Y. Bando, *J. Phys. Soc. Jpn.* **1998**, 67, 651.
- [87] M. Izumi, K. Nakazawa, Y. Bando, Y. Yoneda, H. Terauchi, *Solid State Ion.* **1998**, 108, 227.
- [88] S. G. Jeong, A. Seo, W. S. Choi, *Adv. Sci.* **2022**, 9, 2103403.
- [89] S. G. Jeong, H. Kim, S. J. Hong, D. Suh, W. S. Choi, *ACS Appl. Nano Mater.* **2021**, 4, 2160.
- [90] S. W. Cho, S. G. Jeong, H. Y. Kwon, S. Song, S. Han, J. H. Han, S. Park, W. S. Choi, S. Lee, J. W. Choi, *Acta Mater.* **2021**, 216, 117153.
- [91] S. G. Jeong, G. Han, S. Song, T. Min, A. Y. Mohamed, S. Park, J. Lee, H. Y. Jeong, Y.-M. Kim, D.-Y. Cho, W. S. Choi, *Adv. Sci.* **2020**, 7, 2001643.
- [92] S. G. Jeong, T. Min, S. Woo, J. Kim, Y.-Q. Zhang, S. W. Cho, J. Son, Y.-M. Kim, J. H. Han, S. Park, H. Y. Jeong, H. Ohta, S. Lee, T. W. Noh, J. Lee, W. S. Choi, *Phys. Rev. Lett.* **2020**, 124, 026401.
- [93] S. G. Jeong, S. Song, S. Park, V. Lauter, W. S. Choi, *Small Methods* n/a, 2201386.
- [94] S. G. Jeong, W. S. Choi, A. Y. Mohamed, D.-Y. Cho, *J. Korean Phys. Soc.* **2023**, DOI: 10.1007/s40042-022-00695-5.
- [95] C. v. Korff Schmising, A. Harpoeth, N. Zhavoronkov, Z. Ansari, C. Aku-Leh, M. Woerner, T. Elsaesser, M. Bargheer, M. Schmidbauer, I. Vrejoiu, D. Hesse, M. Alexe, *Phys. Rev. B* **2008**, 78, 060404.
- [96] M. Kim, C.-J. Kang, J.-H. Han, K. Kim, B. Kim, *Phys. Rev. B* **2022**, 106, L201103.
- [97] B. Kim, S. Khmelevskiy, C. Franchini, I. I. Mazin, K. Kim, *Phys. Rev. B* **2020**, 101, 220502.
- [98] P.-C. Wu, H. Song, Y. Yuan, B. Feng, Y. Ikuhara, R. Huang, P. Yu, C.-G. Duan, Y.-H. Chu, *Phys. Rev. Mater.* **2020**, 4, 014401.
- [99] J. Zhang, L. Cheng, H. Cao, M. Bao, J. Zhao, X. Liu, A. Zhao, Y. Choi, H. Zhou, P. Shafer, X. Zhai, *Nano Research* **2022**, 15, 7584.
- [100] F. Bern, M. Ziese, A. Setzer, E. Pippel, D. Hesse, I. Vrejoiu, *J. Phys. Condens. Matter* **2013**, 25, 496003.
- [101] M. Gu, Q. Xie, X. Shen, R. Xie, J. Wang, G. Tang, D. Wu, G. P. Zhang, X. S. Wu, *Phys.*

- Rev. Lett.* **2012**, 109, 157003.
- [102] M. Verissimo-Alves, P. García-Fernández, D. I. Bilc, P. Ghosez, J. Junquera, *Phys. Rev. Lett.* **2012**, 108, 107003.
- [103] C.-Y. Yang, P.-C. Wu, Y.-H. Chu, K.-H. Lin, *New J. Phys.* **2021**, 23, 053009.
- [104] P. García-Fernández, M. Verissimo-Alves, D. I. Bilc, P. Ghosez, J. Junquera, *Phys. Rev. B* **2012**, 86, 085305.
- [105] H. Boschker, T. Harada, T. Asaba, R. Ashoori, A. V. Boris, H. Hilgenkamp, C. R. Hughes, M. E. Holtz, L. Li, D. A. Muller, H. Nair, P. Reith, X. Renshaw Wang, D. G. Schlom, A. Soukiassian, J. Mannhart, *Phys. Rev. X* **2019**, 9, 011027.
- [106] M. Gu, K. Wang, Y. Wang, Q. Xie, H. Cai, G.-P. Zhang, X. Wu, *npj Quantum Mater.* **2016**, 1, 16011.
- [107] Z. Cui, A. J. Grutter, H. Zhou, H. Cao, Y. Dong, D. A. Gilbert, J. Wang, Y.-S. Liu, J. Ma, Z. Hu, J. Guo, J. Xia, B. J. Kirby, P. Shafer, E. Arenholz, H. Chen, X. Zhai, Y. Lu, *Sci. Adv.* **2020**, 6, eaay0114.
- [108] A. Bojahr, D. Schick, L. Maerten, M. Herzog, I. Vrejoiu, C. von Korff Schmising, C. Milne, S. L. Johnson, M. Bargheer, *Phys. Rev. B* **2012**, 85, 224302.
- [109] H.-J. Liu, M. Ye, C.-Y. Yang, Y.-W. Fang, Y.-Y. Chin, C.-Y. Chen, R. T. Hung, Y. Zhu, L.-C. He, M.-Y. Huang, L. Chen, M. Gu, S. Ke, Y.-F. Liao, K.-D. Tsuei, H.-J. Lin, C.-T. Chen, S. Agrestini, J. Herrero-Martin, C.-H. Lai, *Appl. Mater. Today* **2021**, 24, 101101.
- [110] J. L. Lin, Y. Sun, R. He, Y. Li, Z. Zhong, P. Gao, X. Zhao, Z. Zhang, Z. J. Wang, *Nano Letters* **2022**, 22, 7104.
- [111] K. Ueda, H. Saeki, H. Tabata, T. Kawai, *Solid State Commun.* **2000**, 116, 221.
- [112] M. Ye, S. Hu, Y. Zhu, Y. Zhang, S. Ke, L. Xie, Y. Zhang, S. Hu, D. Zhang, Z. Luo, M. Gu, J. He, P. Zhang, W. Zhang, L. Chen, *Nano Letters* **2021**, 21, 144.
- [113] C. v. Korff Schmising, M. Bargheer, M. Kiel, N. Zhavoronkov, M. Woerner, T. Elsaesser, I. Vrejoiu, D. Hesse, M. Alexe, *Phys. Rev. Lett.* **2007**, 98, 257601.
- [114] M. Hadjimichael, Y. Li, L. Yedra, B. Dkhil, P. Zubko, *Phys. Rev. Mater.* **2020**, 4, 094415.
- [115] J. L. Lin, Z. J. Wang, X. Zhao, Z. D. Zhang, *Ceram. Int.* **2020**, 46, 9328.
- [116] Z. Q. Liu, Y. Ming, W. M. Lü, Z. Huang, X. Wang, B. M. Zhang, C. J. Li, K. Gopinadhan, S. W. Zeng, A. Annadi, Y. P. Feng, T. Venkatesan, Ariando, *Appl. Phys. Lett.* **2012**, 101, 223105.
- [117] S. Lin, Q. Zhang, X. Sang, J. Zhao, S. Cheng, A. Huon, Q. Jin, S. Chen, S. Chen, W. Cui, H. Guo, M. He, C. Ge, C. Wang, J. Wang, M. R. Fitzsimmons, L. Gu, T. Zhu, K. Jin, E.-J. Guo, *Nano Letters* **2021**, 21, 3146.
- [118] M. Ziese, I. Vrejoiu, D. Hesse, *Appl. Phys. Lett.* **2010**, 97, 052504.
- [119] S. Thota, Q. Zhang, F. Guillou, U. Lüders, N. Barrier, W. Prellier, A. Wahl, P. Padhan, *Appl. Phys. Lett.* **2010**, 97, 112506.
- [120] Y. Shiomi, Y. Handa, T. Kikkawa, E. Saitoh, *Phys. Rev. B* **2015**, 92, 024418.
- [121] K. Lv, H. P. Zhu, W. Q. Zou, F. M. Zhang, X. S. Wu, *J. Appl. Phys.* **2015**, 117, 185305.
- [122] I. Lindfors-Vrejoiu, M. Ziese, *Phys. Status Solidi B* **2017**, 254, 1600556.
- [123] R. S. Helen, W. Prellier, P. Padhan, *J. Appl. Phys.* **2020**, 128, 033906.
- [124] M. Ziese, E. Pippel, E. Nikulina, M. Arredondo, I. Vrejoiu, *Nanotechnology* **2011**, 22, 254025.
- [125] M. Ziese, I. Lindfors-Vrejoiu, *J. Appl. Phys.* **2018**, 124, 163905.
- [126] B. C. Behera, P. Padhan, W. Prellier, *J. Magn. Magn. Mater.* **2015**, 388, 22.
- [127] M. Ziese, *Phys. Status Solidi - Rapid Res. Lett.* **2011**, 5, 444.
- [128] I. Razdolski, R. R. Subkhangulov, D. G. Gheorghe, F. Bern, I. Vrejoiu, A. V. Kimel, A. Kirilyuk, M. Ziese, T. Rasing, *Phys. Status Solidi - Rapid Res. Lett.* **2015**, 9, 583.
- [129] B. C. Behera, A. V. Ravindra, P. Padhan, W. Prellier, *Appl. Phys. Lett.* **2014**, 104, 092406.
- [130] R. Hillebrand, E. Pippel, D. Hesse, I. Vrejoiu, *Phys. Status Solidi A* **2011**, 208, 2144.
- [131] S. N. Jammalamadaka, J. Vanacken, V. V. Moshchalkov, *Appl. Phys. Lett.* **2014**, 105,

- 033505.
- [132] P. Padhan, W. Prellier, *Appl. Phys. Lett.* **2011**, 99, 263108.
- [133] M. Ziese, F. Bern, E. Pippel, D. Hesse, I. Vrejoiu, *Nano Letters* **2012**, 12, 4276.
- [134] S. Das, A. Herklotz, E. Pippel, E. J. Guo, D. Rata, K. Dörr, *Phys. Rev. B* **2015**, 91, 134405.
- [135] R. S. H, W. Prellier, P. Padhan, *Nanoscale* **2020**, 12, 5151.
- [136] M. Ziese, I. Vrejoiu, E. Pippel, P. Esquinazi, D. Hesse, C. Etz, J. Henk, A. Ernst, I. V. Maznichenko, W. Hergert, I. Mertig, *Phys. Rev. Lett.* **2010**, 104, 167203.
- [137] Y. Shiomi, Y. Handa, T. Kikkawa, E. Saitoh, *Appl. Phys. Lett.* **2015**, 106, 232403.
- [138] M. Ziese, L. Jin, I. Lindfors-Vrejoiu, *J. Phys. Condens. Materials* **2019**, 2, 034008.
- [139] M. Ziese, I. Vrejoiu, *Phys. Rev. B* **2011**, 84, 104413.
- [140] M. Ziese, F. Bern, I. Vrejoiu, *J. Appl. Phys.* **2013**, 113, 063911.
- [141] M. Ziese, I. Vrejoiu, E. Pippel, A. Hähnel, E. Nikulina, D. Hesse, *J. Phys. D: Appl. Phys* **2011**, 44, 345001.
- [142] R. Hillebrand, E. Pippel, I. Vrejoiu, D. Hesse, *Phys. Status Solidi A* **2014**, 211, 536.
- [143] M. Ziese, I. Vrejoiu, *Phys. Status Solidi - Rapid Res. Lett.* **2013**, 7, 243.
- [144] L. Qu, D. Lan, L. Si, C. Ma, S. Wang, L. Xu, K. Zhang, F. Jin, Z. Zhang, E. Hua, B. Chen, G. Gao, F. Chen, H. Du, K. Held, L. Wang, W. Wu, *Nano Research* **2021**, 14, 3621.
- [145] L. Qu, D. Lan, K. Zhang, E. Hua, B. Ge, L. Xu, F. Jin, G. Gao, L. Wang, W. Wu, *AIP Advances* **2021**, 11, 075001.
- [146] G. Q. Gong, A. Gupta, G. Xiao, P. Lecoeur, T. R. McGuire, *Phys. Rev. B* **1996**, 54, R3742.
- [147] A. Sahoo, W. Prellier, P. Padhan, *Adv. Mater. Interfaces* **2018**, 5, 1800913.
- [148] A. Sahoo, P. Padhan, W. Prellier, *ACS Appl. Mater. Interfaces* **2017**, 9, 36423.
- [149] A. Sahoo, W. Prellier, P. Padhan, *ACS Appl. Mater. Interfaces* **2018**, 10, 44190.
- [150] S. Dong, Q. Zhang, S. Yunoki, J. M. Liu, E. Dagotto, *Phys. Rev. B* **2011**, 84, 224437.
- [151] P. Padhan, W. Prellier, *Eur. Phys. J. B* **2005**, 45, 169.
- [152] P. Padhan, W. Prellier, *Appl. Phys. Lett.* **2006**, 88, 263114.
- [153] Y. Choi, Y. C. Tseng, D. Haskel, D. E. Brown, D. Danaher, O. Chmaissem, *Appl. Phys. Lett.* **2008**, 93, 192509.
- [154] P. Padhan, W. Prellier, B. Mercey, *Phys. Rev. B* **2004**, 70, 184419.
- [155] Y.-Z. Yoo, O. Chmaissem, J.-H. Song, *Curr. Appl. Phys.* **2014**, 14, 378.
- [156] W. Wang, H. Zhang, X. Shen, X. Guan, Y. Yao, Y. Wang, J. Sun, R. Yu, *J. Cryst. Growth* **2018**, 490, 110.
- [157] P. Liu, X. Ning, *Materials Research Letters* **2020**, 8, 173.
- [158] X. Yao, C. Wang, E.-J. Guo, X. Wang, X. Li, L. Liao, Y. Zhou, S. Lin, Q. Jin, C. Ge, M. He, X. Bai, P. Gao, G. Yang, K.-j. Jin, *ACS Appl. Mater. Interfaces* **2022**, 14, 6194.
- [159] A. Singh, J. Chen, *Ceram. Int.* **2019**, 45, 20465.
- [160] S. Yousfi, M. El Marssi, H. Bouyanfif, *Superlattices Microstruct.* **2021**, 156, 106983.
- [161] Z. Zeng, J. Feng, X. Zheng, C. Wang, J. Liu, Z. Lu, F.-X. Jiang, X.-H. Xu, Z. Wang, R.-W. Li, *Appl. Phys. Lett.* **2020**, 116, 142401.
- [162] L. Yang, L. Wysocki, J. Schöpf, L. Jin, A. Kovács, F. Gunkel, R. Dittmann, P. H. M. van Loosdrecht, I. Lindfors-Vrejoiu, *Phys. Rev. Mater.* **2021**, 5, 014403.
- [163] B. Pang, L. Zhang, Y. B. Chen, J. Zhou, S. Yao, S. Zhang, Y. Chen, *ACS Appl. Mater. Interfaces* **2017**, 9, 3201.
- [164] L. Wysocki, J. Schöpf, M. Ziese, L. Yang, A. Kovács, L. Jin, R. B. Versteeg, A. Bliesener, F. Gunkel, L. Kornblum, R. Dittmann, P. H. M. van Loosdrecht, I. Lindfors-Vrejoiu, *ACS Omega* **2020**, 5, 5824.
- [165] A. Herklotz, K. Dörr, *The European Physical Journal B* **2015**, 88, 60.
- [166] S. J. May, J. W. Kim, J. M. Rondinelli, E. Karapetrova, N. A. Spaldin, A. Bhattacharya,

- P. J. Ryan, *Phys. Rev. B* **2010**, 82, 014110.
- [167] A. A. Balandin, E. P. Pokatilov, D. L. Nika, *J. Nanoelectron. Optoelectron.* **2007**, 2, 140.
- [168] A. Bartels, T. Dekorsy, H. Kurz, K. Köhler, *Phys. Rev. Lett.* **1999**, 82, 1044.
- [169] T. A. Palomaki, J. W. Harlow, J. D. Teufel, R. W. Simmonds, K. W. Lehnert, *Nature* **2013**, 495, 210.
- [170] R. W. Andrews, R. W. Peterson, T. P. Purdy, K. Cicak, R. W. Simmonds, C. A. Regal, K. W. Lehnert, *Nat. Phys.* **2014**, 10, 321.
- [171] F. Massel, T. T. Heikkilä, J. M. Pirkkalainen, S. U. Cho, H. Saloniemi, P. J. Hakonen, M. A. Sillanpää, *Nature* **2011**, 480, 351.
- [172] R. Manenti, A. F. Kockum, A. Patterson, T. Behrle, J. Rahamim, G. Tancredi, F. Nori, P. J. Leek, *Nat. Commun.* **2017**, 8, 975.
- [173] D. Kirillov, Y. Suzuki, L. Antognazza, K. Char, I. Bozovic, T. H. Geballe, *Phys. Rev. B* **1995**, 51, 12825.
- [174] M. N. Iliev, A. P. Litvinchuk, H. G. Lee, C. L. Chen, M. L. Dezaneti, C. W. Chu, V. G. Ivanov, M. V. Abrashev, V. N. Popov, *Phys. Rev. B* **1999**, 59, 364.
- [175] L. Liu, Q. Qin, W. Lin, C. Li, Q. Xie, S. He, X. Shu, C. Zhou, Z. Lim, J. Yu, W. Lu, M. Li, X. Yan, S. J. Pennycook, J. Chen, *Nature Nanotechnology* **2019**, 14, 939.
- [176] M. Yamanouchi, Y. Araki, T. Sakai, T. Uemura, H. Ohta, J. i. Ieda, *Sci. Adv.* **2022**, 8, eabl6192.
- [177] Y. Chen, D. L. Bergman, A. A. Burkov, *Phys. Rev. B* **2013**, 88, 125110.
- [178] H. G. Lee, L. Wang, L. Si, X. He, D. G. Porter, J. R. Kim, E. K. Ko, J. Kim, S. M. Park, B. Kim, A. T. S. Wee, A. Bombardi, Z. Zhong, T. W. Noh, *Adv. Mater.* **2020**, 32, 1905815.
- [179] Z. Zhong, P. Hansmann, *Phys. Rev. X* **2017**, 7, 011023.
- [180] L. Sheng, D. N. Sheng, C. S. Ting, *Phys. Rev. Lett.* **2006**, 96, 155901.
- [181] D. M. Juraschek, N. A. Spaldin, *Phys. Rev. Mater.* **2019**, 3, 064405.
- [182] V. L. Korenev, M. Salewski, I. A. Akimov, V. F. Sapega, L. Langer, I. V. Kalitukha, J. Debus, R. I. Dzhioev, D. R. Yakovlev, D. Müller, C. Schröder, H. Hövel, G. Karczewski, M. Wiater, T. Wojtowicz, Y. G. Kusrayev, M. Bayer, *Nat. Phys.* **2016**, 12, 85.
- [183] D. Liu, J. Shi, *Phys. Rev. Lett.* **2017**, 119, 075301.
- [184] G. Grissonnanche, S. Thériault, A. Gourgout, M. E. Boulanger, E. Lefrançois, A. Ataei, F. Laliberté, M. Dion, J. S. Zhou, S. Pyon, T. Takayama, H. Takagi, N. Doiron-Leyraud, L. Taillefer, *Nat. Phys.* **2020**, 16, 1108.
- [185] D. Kan, T. Moriyama, K. Kobayashi, Y. Shimakawa, *Phys. Rev. B* **2018**, 98, 180408.
- [186] H. Huang, S.-J. Lee, B. Kim, B. Sohn, C. Kim, C.-C. Kao, J.-S. Lee, *ACS Appl. Mater. Interfaces* **2020**, 12, 37757.
- [187] W. Witczak-Krempa, G. Chen, Y. B. Kim, L. Balents, *Annu. Rev. Condens. Matter Phys.* **2014**, 5, 57.
- [188] J. G. Rau, E. K.-H. Lee, H.-Y. Kee, *Annu. Rev. Condens. Matter Phys.* **2016**, 7, 195.
- [189] R. Schaffer, E. K. H. Lee, B. J. Yang, Y. B. Kim, *Rep. Prog. Phys.* **2016**, 79, 094504.
- [190] G. Cao, P. Schlottmann, *Rep. Prog. Phys.* **2018**, 81, 042502.
- [191] J. Bertinshaw, Y. K. Kim, G. Khaliullin, B. J. Kim, *Annu. Rev. Condens. Matter Phys.* **2019**, 10, 315.
- [192] A. Biswas, Y. H. Jeong, *Curr. Appl. Phys.* **2017**, 17, 605.
- [193] L. Hao, D. Yi, M. Wang, J. Liu, P. Yu, *Fundam. res.* **2022**, DOI: <https://doi.org/10.1016/j.fmre.2022.09.030>.
- [194] B. J. Kim, H. Jin, S. J. Moon, J. Y. Kim, B. G. Park, C. S. Leem, J. Yu, T. W. Noh, C. Kim, S. J. Oh, J. H. Park, V. Durairaj, G. Cao, E. Rotenberg, *Phys. Rev. Lett.* **2008**, 101, 076402.
- [195] S. J. Moon, H. Jin, K. W. Kim, W. S. Choi, Y. S. Lee, J. Yu, G. Cao, A. Sumi, H. Funakubo, C. Bernhard, T. W. Noh, *Phys. Rev. Lett.* **2008**, 101, 226402.
- [196] F. Wang, T. Senthil, *Phys. Rev. Lett.* **2011**, 106, 136402.

- [197] H. Watanabe, T. Shirakawa, S. Yunoki, *Phys. Rev. Lett.* **2013**, 110, 027002.
- [198] G. Jackeli, G. Khaliullin, *Phys. Rev. Lett.* **2009**, 102, 017205.
- [199] L. Hao, D. Meyers, C. Frederick, G. Fabbris, J. Yang, N. Traynor, L. Horak, D. Kriegner, Y. Choi, J.-W. Kim, D. Haskel, P. J. Ryan, M. P. M. Dean, J. Liu, *Phys. Rev. Lett.* **2017**, 119, 027204.
- [200] B. Kim, P. Liu, C. Franchini, *Phys. Rev. B* **2017**, 95, 115111.
- [201] J. Hubbard, *Proc. R. Soc. A Math. Phys. Eng. Sci.* **1963**, 276, 238.
- [202] S. Y. Kim, C. H. Kim, L. J. Sandilands, C. H. Sohn, J. Matsuno, H. Takagi, K. W. Kim, Y. S. Lee, S. J. Moon, T. W. Noh, *Phys. Rev. B* **2016**, 94, 245113.
- [203] D. Meyers, Y. Cao, G. Fabbris, N. J. Robinson, L. Hao, C. Frederick, N. Traynor, J. Yang, J. Lin, M. H. Upton, D. Casa, J.-W. Kim, T. Gog, E. Karapetrova, Y. Choi, D. Haskel, P. J. Ryan, L. Horak, X. Liu, J. Liu, M. P. M. Dean, *Sci. Rep.* **2019**, 9, 4263.
- [204] D. Gong, J. Yang, L. Hao, L. Horak, Y. Xin, E. Karapetrova, J. Stremper, Y. Choi, J.-W. Kim, P. J. Ryan, J. Liu, *Phys. Rev. Lett.* **2022**, 129, 187201.
- [205] L. Hao, D. Meyers, H. Suwa, J. Yang, C. Frederick, T. R. Dasa, G. Fabbris, L. Horak, D. Kriegner, Y. Choi, J.-W. Kim, D. Haskel, P. J. Ryan, H. Xu, C. D. Batista, M. P. M. Dean, J. Liu, *Nat. Phys.* **2018**, 14, 806.
- [206] J. Yang, H. Suwa, D. Meyers, H. Zhang, L. Horak, Z. Wang, G. Fabbris, Y. Choi, J. Karapetrova, J.-W. Kim, D. Haskel, P. J. Ryan, M. P. M. Dean, L. Hao, J. Liu, *Phys. Rev. X* **2022**, 12, 031015.
- [207] M.-W. Yoo, J. Tornos, A. Sander, L.-F. Lin, N. Mohanta, A. Peralta, D. Sanchez-Manzano, F. Gallego, D. Haskel, J. W. Freeland, D. J. Keavney, Y. Choi, J. Stremper, X. Wang, M. Cabero, H. B. Vasili, M. Valvidares, G. Sanchez-Santolino, J. M. Gonzalez-Calbet, A. Rivera, C. Leon, S. Rosenkranz, M. Bibes, A. Barthelemy, A. Anane, E. Dagotto, S. Okamoto, S. G. E. te Velthuis, J. Santamaria, J. E. Villegas, *Nat. Commun.* **2021**, 12, 3283.
- [208] D. Yi, J. Liu, S. L. Hsu, L. P. Zhang, Y. Choi, J. W. Kim, Z. H. Chen, J. D. Clarkson, C. R. Serrao, E. Arenholz, P. J. Ryan, H. X. Xu, R. J. Birgeneau, R. Ramesh, *Proc. Natl. Acad. Sci. U. S. A.* **2016**, 113, 6397.
- [209] J. W. Kim, Y. Choi, S. H. Chun, D. Haskel, D. Yi, R. Ramesh, J. Liu, P. J. Ryan, *Phys. Rev. B* **2018**, 97, 094426.
- [210] D. Yi, C. L. Flint, P. P. Balakrishnan, K. Mahalingam, B. Urwin, A. Vailionis, A. T. N'Diaye, P. Shafer, E. Arenholz, Y. Choi, K. H. Stone, J.-H. Chu, B. M. Howe, J. Liu, I. R. Fisher, Y. Suzuki, *Phys. Rev. Lett.* **2017**, 119, 077201.
- [211] D. Yi, Y. Wang, O. M. J. van 't Erve, L. Xu, H. Yuan, M. J. Veit, P. P. Balakrishnan, Y. Choi, A. T. N'Diaye, P. Shafer, E. Arenholz, A. Grutter, H. Xu, P. Yu, B. T. Jonker, Y. Suzuki, *Nat. Commun.* **2020**, 11, 902.
- [212] J. Nichols, X. Gao, S. Lee, T. L. Meyer, J. W. Freeland, V. Lauter, D. Yi, J. Liu, D. Haskel, J. R. Petrie, E.-J. Guo, A. Herklotz, D. Lee, T. Z. Ward, G. Eres, M. R. Fitzsimmons, H. N. Lee, *Nat. Commun.* **2016**, 7, 12721.
- [213] A. K. Jaiswal, D. Wang, V. Wollersen, R. Schneider, M. L. Tacon, D. Fuchs, *Adv. Mater.* **2022**, 34, 2109163.
- [214] J. Liu, X. Zhang, Y. Ji, X. Gao, J. Wu, M. Zhang, L. Li, X. Liu, W. Yan, T. Yao, Y. Yin, L. Wang, H. Guo, G. Cheng, Z. Wang, P. Gao, Y. Wang, K. Chen, Z. Liao, *J. Phys. Chem. Lett.* **2022**, 13, 11946.
- [215] A. K. Jaiswal, R. Schneider, M. L. Tacon, D. Fuchs, *AIP Advances* **2022**, 12, 035120.
- [216] E. Skoropata, J. Nichols, J. M. Ok, R. V. Chopdekar, E. S. Choi, A. Rastogi, C. Sohn, X. Gao, S. Yoon, T. Farmer, R. D. Desautels, Y. Choi, D. Haskel, J. W. Freeland, S. Okamoto, M. Brahlek, H. N. Lee, *Sci. Adv.* **2020**, 6, eaaz3902.
- [217] X. Liu, M. Kotiuga, H.-S. Kim, A. T. N'Diaye, Y. Choi, Q. Zhang, Y. Cao, M. Kareev, F. Wen, B. Pal, J. W. Freeland, L. Gu, D. Haskel, P. Shafer, E. Arenholz, K. Haule, D.

- Vanderbilt, K. M. Rabe, J. Chakhalian, *Proc. Natl. Acad. Sci. U. S. A.* **2019**, 116, 19863.
- [218] M. Gu, R. Zhu, X. Zhang, Z. Wang, Q. An, F. Yang, X. Liu, P. Gao, M. Meng, J. Guo, *ACS Appl. Electron. Mater.* **2022**, 4, 3707.
- [219] K. H. Kim, H. S. Kim, M. J. Han, *J. Phys.: Condens. Matter* **2014**, 26, 185501.
- [220] D. J. Groenendijk, N. Manca, G. Mattoni, L. Kootstra, S. Gariglio, Y. Huang, E. van Heumen, A. D. Caviglia, *Appl. Phys. Lett.* **2016**, 109, 041906.
- [221] D. Hirai, J. Matsuno, H. Takagi, *APL Mater.* **2015**, 3, 041508.
- [222] T. J. Anderson, S. Ryu, H. Zhou, L. Xie, J. P. Podkaminer, Y. Ma, J. Irwin, X. Q. Pan, M. S. Rzechowski, C. B. Eom, *Appl. Phys. Lett.* **2016**, 108, 151604.
- [223] C. C. Fan, Z. T. Liu, S. H. Cai, Z. Wang, P. Xiang, K. L. Zhang, W. L. Liu, J. S. Liu, P. Wang, Y. Zheng, D. W. Shen, L. X. You, *AIP Adv.* **2017**, 7, 085307.
- [224] A. M. Glazer, *Acta Cryst.* **1972**, B28, 3384.
- [225] A. M. Glazer, *Acta Cryst.* **1975**, A31, 756.
- [226] L. Shekhtman, O. Entin-Wohlman, A. Aharony, *Phys. Rev. Lett.* **1992**, 69, 836.
- [227] M. P. M. Dean, R. S. Springell, C. Monney, K. J. Zhou, J. Pereiro, I. Božović, B. Dalla Piazza, H. M. Rønnow, E. Morenzoni, J. van den Brink, T. Schmitt, J. P. Hill, *Nat. Mater.* **2012**, 11, 850.
- [228] S. Boseggia, R. Springell, H. C. Walker, H. M. Ronnow, C. Ruegg, H. Okabe, M. Isobe, R. S. Perry, S. P. Collins, D. F. McMorrow, *Phys. Rev. Lett.* **2013**, 110, 117207.
- [229] L. Paolasini, *École thématique de la Société Française de la Neutronique* **2014**, 13, 03002.
- [230] J. Stöhr, H. C. Siegmann, *Interactions of Polarized Photons with Matter*, Springer, **2006**.
- [231] J. W. Kim, Y. Choi, J. Kim, J. F. Mitchell, G. Jackeli, M. Daghofer, J. van den Brink, G. Khaliullin, B. J. Kim, *Phys. Rev. Lett.* **2012**, 109, 037204.
- [232] K. Ohgushi, J.-i. Yamaura, H. Ohsumi, K. Sugimoto, S. Takeshita, A. Tokuda, H. Takagi, M. Takata, T.-h. Arima, *Phys. Rev. Lett.* **2013**, 110, 217212.
- [233] H. Kim, J. Bertinshaw, J. Porras, B. Keimer, J. Kim, J. W. Kim, J. Kim, J. Kim, G. Noh, G.-Y. Kim, S.-Y. Choi, B. J. Kim, *Phys. Rev. Res.* **2022**, 4, 013229.
- [234] J. Kim, A. H. Said, D. Casa, M. H. Upton, T. Gog, M. Daghofer, G. Jackeli, J. van den Brink, G. Khaliullin, B. J. Kim, *Phys. Rev. Lett.* **2012**, 109, 157402.
- [235] D. G. Mazzone, Y. Shen, H. Suwa, G. Fabbris, J. Yang, S. S. Zhang, H. Miao, J. Sears, K. Jia, Y. G. Shi, M. H. Upton, D. M. Casa, X. Liu, J. Liu, C. D. Batista, M. P. M. Dean, *Nat. Commun.* **2022**, 13, 913.
- [236] A. Vasiliev, O. Volkova, E. Zvereva, M. Markina, *npj Quantum Mater.* **2018**, 3, 18.
- [237] M. Gibertini, M. Koperski, A. F. Morpurgo, K. S. Novoselov, *Nat. Nanotechnol.* **2019**, 14, 408.
- [238] N. D. Mermin, H. Wagner, *Phys. Rev. Lett.* **1966**, 17, 1133.
- [239] E. Manousakis, *Rev. Mod. Phys.* **1991**, 63, 1.
- [240] E. Dagotto, *Rev. Mod. Phys.* **1994**, 66, 763.
- [241] L. Hao, D. Meyers, M. P. M. Dean, J. Liu, *J. Phys. Chem. Solids* **2019**, 128, 39.
- [242] L. Néel, *Nobel Lectures, Physics* **1970**, 1963.
- [243] V. Baltz, A. Manchon, M. Tsoi, T. Moriyama, T. Ono, Y. Tserkovnyak, *Rev. Mod. Phys.* **2018**, 90, 015005.
- [244] C. Song, Y. You, X. Chen, X. Zhou, Y. Wang, F. Pan, *Nanotechnology* **2018**, 29, 112001.
- [245] T. Jungwirth, X. Marti, P. Wadley, J. Wunderlich, *Nat. Nanotechnol.* **2016**, 11, 231.
- [246] P. Wadley, B. Howells, J. Železný, C. Andrews, V. Hills, R. P. Champion, V. Novák, K. Olejník, F. Maccherozzi, S. S. Dhesi, S. Y. Martin, T. Wagner, J. Wunderlich, F. Freimuth, Y. Mokrousov, J. Kuneš, J. S. Chauhan, M. J. Grzybowski, A. W. Rushforth, K. W. Edmonds, B. L. Gallagher, T. Jungwirth, *Science* **2016**, 351, 587.
- [247] B. H. Brandow, *Adv. Phys.* **1977**, 26, 651.
- [248] J. Yang, L. Hao, D. Meyers, T. Dasa, L. Xu, L. Horak, P. Shafer, E. Arenholz, G. Fabbris,

- Y. Choi, D. Haskel, J. Karapetrova, J.-W. Kim, P. J. Ryan, H. Xu, C. D. Batista, M. P. M. Dean, J. Liu, *Phys. Rev. Lett.* **2020**, 124, 177601.
- [249] H.-J. Noh, S. J. Oh, B. G. Park, J. H. Park, J. Y. Kim, H. D. Kim, T. Mizokawa, L. H. Tjeng, H. J. Lin, C. T. Chen, S. Schuppler, S. Nakatsuji, H. Fukazawa, Y. Maeno, *Phys. Rev. B* **2005**, 72, 052411.
- [250] S. J. Moon, M. W. Kim, K. W. Kim, Y. S. Lee, J. Y. Kim, J. H. Park, B. J. Kim, S. J. Oh, S. Nakatsuji, Y. Maeno, I. Nagai, S. I. Ikeda, G. Cao, T. W. Noh, *Phys. Rev. B* **2006**, 74, 113104.
- [251] T. Moriya, *Phys. Rev.* **1960**, 120, 91.
- [252] J. P. F. LeBlanc, A. E. Antipov, F. Becca, I. W. Bulik, G. K.-L. Chan, C.-M. Chung, Y. Deng, M. Ferrero, T. M. Henderson, C. A. Jiménez-Hoyos, E. Kozik, X.-W. Liu, A. J. Millis, N. V. Prokof'ev, M. Qin, G. E. Scuseria, H. Shi, B. V. Svistunov, L. F. Tocchio, I. S. Tupitsyn, S. R. White, S. Zhang, B.-X. Zheng, Z. Zhu, E. Gull, *Phys. Rev. X* **2015**, 5, 041041.
- [253] L. Hao, Z. Wang, J. Yang, D. Meyers, J. Sanchez, G. Fabbris, Y. Choi, J.-W. Kim, D. Haskel, P. J. Ryan, K. Barros, J.-H. Chu, M. P. M. Dean, C. D. Batista, J. Liu, *Nat. Commun.* **2019**, 10, 5301.
- [254] C. Haas, *Phys. Rev.* **1968**, 168, 531.
- [255] S. Alexander, J. S. Helman, I. Balberg, *Phys. Rev. B* **1976**, 13, 304.
- [256] A. R. Bishop, H. Roder, *Curr. Opin. Solid State Mater. Sci.* **1997**, 2, 244.
- [257] A. P. Ramirez, *J. Phys.: Condens. Matter* **1997**, 9, 8171.
- [258] J. Z. Sun, A. Gupta, *Annu. Rev. Mater. Sci.* **1998**, 28, 45.
- [259] E. Dagotto, T. Hotta, A. Moreo, *Phys. Rep.* **2001**, 344, 1.
- [260] M. B. Salamon, M. Jaime, *Rev. Mod. Phys.* **2001**, 73, 583.
- [261] M. Ziese, *Rep. Prog. Phys.* **2002**, 65, 143.
- [262] Y. Ando, *J. Phys. Soc. Jpn.* **2013**, 82, 102001.
- [263] M. Z. Hasan, C. L. Kane, *Rev. Mod. Phys.* **2010**, 82, 3045.
- [264] Y. Tokura, *Nat. Mater.* **2022**, 21, 971.
- [265] N. Nagaosa, J. Sinova, S. Onoda, A. H. MacDonald, N. P. Ong, *Rev. Mod. Phys.* **2010**, 82, 1539.
- [266] D. Xiao, M.-C. Chang, Q. Niu, *Rev. Mod. Phys.* **2010**, 82, 1959.
- [267] Y. Chen, Y.-M. Lu, H.-Y. Kee, *Nat. Commun.* **2015**, 6, 6593.
- [268] X. Liu, W. Song, M. Wu, Y. Yang, Y. Yang, P. Lu, Y. Tian, Y. Sun, J. Lu, J. Wang, D. Yan, Y. Shi, N. X. Sun, Y. Sun, P. Gao, K. Shen, G. Chai, S. Kou, C.-W. Nan, J. Zhang, *Nat. Commun.* **2021**, 12, 5453.
- [269] J. H. Gruenewald, J. Kim, H. S. Kim, J. M. Johnson, J. Hwang, M. Souri, J. Terzic, S. H. Chang, A. Said, J. W. Brill, G. Cao, H.-Y. Kee, S. S. A. Seo, *Adv. Mater.* **2017**, 29, 1603798.
- [270] H. Xu, H. Huang, Q. Wu, Z. Wang, Z. Cui, X. Zhai, J. Wang, Z. Fu, Y. Lu, *J. Mater. Sci.* **2020**, 55, 8211.
- [271] S. Y. Jang, H. Kim, S. J. Moon, W. S. Choi, B. C. Jeon, J. Yu, T. W. Noh, *J. Phys. Condens. Matter* **2010**, 22, 485602.
- [272] Z. S. Lim, C. Li, X. Chi, G. J. Omar, H. H. Ma, Z. Huang, S. Zeng, P. Yang, T. Venkatesan, A. Rusydi, S. J. Pennycook, A. Ariando, *Nano Lett.* **2020**, 20, 1890.
- [273] M. Vagadia, S. Sardar, T. Tank, S. Das, B. Gunn, P. Pandey, R. Hübner, F. Rodolakis, G. Fabbris, Y. Choi, D. Haskel, A. Frano, D. S. Rana, *Phys. Rev. B* **2022**, 105, L020402.